A FUNDAMENTAL STUDY OF SPINEL Co_3O_4 ELECTRO-CATALYST DURINF ELECTROCHEMICAL OXYGEN EVOLUTION REACTION

WANG HSIN-YI

SCHOOL OF CHEMICAL AND BIOMEDICAL ENGINEERING

2016

A FUNDAMENTAL STUDY OF SPINEL Co_3O_4 ELECTRO-CATALYST DURINF ELECTROCHEMICAL OXYGEN EVOLUTION REACTION

WANG HSIN-YI

School of Chemical and Biomedical Engineering

A thesis submitted to the Nanyang Technological University
in partial fulfilment of the requirement for the degree of
Doctor of Philosophy

2016

Acknowledgement

Four years have gone so fast. In this research journey filled with hardness and joy in NTU, I would like to express my deepest appreciation to my supervisor Asst. Prof. Liu Bin, for his guidance, encouragement, support, and enlightenment. He always tried his best to answer any of my questions, and also was happy to share all his personal experiences. What I learned from him was not only principles and theories but also his innovative idea and optimistic attitude as a wisdom scholar. His ambition has motivated me throughout my projects and encouraged me to achieve my goal in my research.

I sincerely thank my family for their encouragement when I decided to pursue my Ph.D degree, and grateful appreciation is specially given to Miss Wei-Chen Hung for her patience and support. The trust, happiness, and confidence delivered through the phone from her always become my greatest spiritual foundation, which supports me in every day at Singapore.

I am grateful to thank Dr. Hongbin Yang, Dr. Jiazeng Chen, Dr. Fangxing Xiao, and Mr. Jianwei Miao who are enthusiastic and skillful researchers in our lab. It is very lucky to work with them during thesis days. With their guidance and kindness suggestions, I have learned quite lots of techniques and experimental skills which enrich my knowledge and facilitate my research.

Appreciation is also given to Prof. Chen Hao-Ming and his research group at National Taiwan University for their friendly supports, advice, and assistances. Special thanks go to Mr. Ying-Ya Hsu, Mr. Sung-Fu Hung and Mr. Ching-Wei Tung for their technological supports and friendly advice in National Synchrotron Radiation Research Center, Taiwan.

I would like to acknowledge Nanyang Technological University (NTU) and Agency for Science, Technology & Research (A*STAR) for providing me the opportunity and supporting me the Singapore International Graduate Award (SINGA) scholarship to pursue my Ph.D. degree. Finally, my great appreciation is given to all my friends and group members. I will remember all the days we have experienced through together. Thank you!

Table of Contacts

List of Figures

List of Tables

Abstract

The energy crisis and related environmental issue is an important issue at a global level. Water electrolysis has been proposed as a promising technology for the production of H_2 that can be directly used as the clean fuel. However, the efficiency of the electrolyser is greatly limited on the anode side, where the oxygen evolution reaction (OER) is a thermodynamic up-hill reaction and which usually requires a high overpotential to drive the reaction. Thus, efficient and earth-abundant electrocatalyst for high-performance OER is essential for the development of sustainable energy conversion technology.

Spinel cobalt oxide (Co_3O_4) is an earth-abundant element which has been extensively studied as effective OER catalyst due to its competitive activity compared to the noble catalyst. To further improve the catalytic activity, substituting Co_3O_4 with Ni has been proposed as a promising approach to enhance the electrochemical activity toward OER. We revealed that by tuning the amount of the coordinating agent of NH^{3+} and/or F^- ions, the Ni dopant was capable of enlarging the surface roughness factor, improving the electrical conductivity of the catalyst, and reducing the activation energy barrier in terms of a relatively earlier onset with a high current density. Meanwhile, we also found the Ni dopants occupied the tetrahedral site of the spinel structure, which could be a critical information because so far, although it has been known the spinel Co_3O_4 was comprised by one Co^{2+} in the tetrahedral site ($Co^{2+}{}_{Td}$) and two Co^{3+} in the octahedral site ($Co^{3+}{}_{Oh}$), the roles of two geometrical cobalt ions toward the OER have remained elusive. To individually understand geometrical-site-dependent OER activity of Co_3O_4 catalyst, we separately examined the properties of $Co^{3+}{}_{Oh}$ and $Co^{2+}{}_{Td}$ by substituting $Co^{2+}{}_{Td}$ and $Co^{3+}{}_{Oh}$ with inactive Zn^{2+} and Al^{3+}, respectively. Following a thorough *in-operando* analysis by electrochemical impedance spectroscopy and X-ray absorption spectroscopy, it was revealed that $Co^{2+}{}_{Td}$ site is responsible for the formation of cobalt oxyhydroxide (CoOOH), which acted as the active site for water oxidation.

Apart from the geometrical-site-dependent activity of spinel Co_3O_4 has been successfully disclosed, we were also surprised that the anodic peak prior to the rise of OER current could be vanished if Zn^{2+} was substituted into the tetrahedral site of Co_3O_4. Thus, the underlying properties of oxidation peak attracted our attentions. Through a combination of well-designed independent in-situ measurements including X-ray absorption and grazing-angle X-ray diffraction under operando conditions, and following a potential-resolved in-situ Raman analysis with their particularly re-designed in-situ cell, we successfully revealed that the anodic peak current could be associated with the formation process of peroxide moieties (e.g., Co-OO-Co or Co-OOH) on the surface of Co_3O_4, and more importantly, Co^{2+}_{Td} ions in Co_3O_4 should be the vital species to bridge the μ-OO bond as the key elementary step for the OER.

In this thesis, we step-by-step revealed the full OER mechanism on spinel Co_3O_4 electrocatalyst carefully and rationally via various *operando* measurements. We wanted to highlight that by doing such detailed study, a rational design for a superior catalyst with highly effective activity is possible.

Organization of this thesis

This Thesis contains **5 chapters** which are organized as listed in the below:

In Chapter 1, a brief background and current issue of water electrolysers were introduced. An overview of the reaction mechanistic insight of oxygen evolution reaction (OER), an introduction to the physical properties of spinel Co_3O_4 as an OER electrocatalyst, the reason why we chose Co_3O_4, research motivations, and objectives of my research were given in this chapter.

In Chapter 2, in order to further improve the catalytic activity of spinel Co_3O_4, a method to simultaneously construct a high electrochemical active surface area (EASA) with an enhanced OER efficiency of Co_3O_4 was then carried out. In which, nickel (Ni) was selected as a crucial dopant to achieve such desired performance.

In Chapter 3, inspired by the experience from the Chapter 2, where a great enhanced catalytic activity of Co_3O_4 was associated with the geometrically substituted Ni ion (the substitute may selectively occupy the tetrahedral or octahedral sites in the normal spinel structure), we proposed that the OER activity of spinel Co_3O_4 may be geometrical-site-dependent. Thus, tow well-designed *operando* techniques, including electrochemical impedance spectroscopy and X-ray absorption spectroscopy, were then carried out to instantaneously the geometrical-site-dependent activity of Co_3O_4 under OER condition.

In Chapter 4, based on the experience learn from chapter 2 & 3, the anodic peak which usually appeared prior to the OER onset attracted our attention because this peak may be associated some importance reactions of the surface intermediates for OER. To uncover a complete scenario of the OER process on Co_3O_4 surface, several advanced *in-situ* measurements were developed for a detailed examination.

In Chapter 5, we summarized all the achievements in each experiment and proffered a mechanism for the overall electrochemical OER process on the Co_3O_4. Then finally, we highlighted our research impact on the electrocatalyst field and proposed some extending works based on the result of this thesis.

Chapter 1. Introduction

1.1 Perspective of water electrolysers and their application

With the growing global population and the increasing demand for the energy, it becomes more and more important to utilize the limited energy resource of our mother plant more efficiently. To date, the energy crisis and environmental issue are the crucial topics at a global level, which greatly motivate scientists' enthusiasm to devote to the development of clean and sustainable green energy resources. In order to reduce the usage of the traditional fossil fuel which usually emits harmful particulate matter and green-house gases, e.g., CO_2 or SO_2, renewable energy such as wind-power, hydro-power, and solar power have been explored and proposed to be the next generation power resource due to their positive impact with no CO_2 emission on the environment and human health. Even though the energy can be almost sustainably generated by the aforementioned methods, the renewable sources produced from the sun or the wind are generally influenced by the intermittent on daily, seasonal changes, and regional scales on different pleases. This characteristic on-peak and off-peak load variations seriously threaten their practicability and reliability. To address the uncertainty as aforementioned, the electricity generated via those methods can be connected to local energy-storages or converted to a different energy form, e.g., H_2O_2[1] or H_2,[2] which could be easy to be stored by an electricity-producing unit.[3] Based on this idea and framework, it is believed water electrolysis technology can be a fundamental solution in the development of a sustainable energy system. Water is the most accessible and cheap material resource on the plant and which occupies up to 70 % of the plant surface. Thus, it has been proposed to be the ideal method to convert the energy by water electrolysers. The water electrolyser is an energy-conversion device which produces hydrogen (H_2) on the cathode electrode and oxygen (O_2) on the anode electrode. Electrolysis is an important technology for the production of H_2 with several advantages including fast dynamic response times, large operational ranges, high efficiencies, and very high gas purities.[3] From which, H_2 with high energy density can be used as an alternative for electricity storage for batteries since it can be converted back to electricity via fuel cells operation,[4] opening up an opportunity for the portable and scalable power and energy devices due to the separation of the hydrogen storage from the electrolysis devices. Thus, Electrolysis is a promising alternative coupled with renewable energy sources.

Since water electrolysis was first reported by Van Trostwijk and Deiman in 1789,[5] this technology has been greatly investigated in depth and applied for real, i.e., providing the oxygen gas for the human daily necessities inside the submarines. However, although this technology possesses the advantages such as flexibility for usage, almost zero emission, and production of high purity gases, substantial efforts are still needed to meet the standards for practical applications and mass-production in terms of efficiency and long-term durability to become economically attractive. In principle, the water electrolysers can be sorted out into two different systems based on the nature of electrolyte: alkaline water electrolysers (AWE) and polymer electrolyte membrane (PEM) electrolysis in acidic media.[6] Typically, the cathodic and anodic reactions occurring at the AWE and PEM electrodes under applying bias can be described by the following equations:

AWE:

$$4e^- + 4H_2O \rightarrow 4OH^- + 2H_2\uparrow \text{ cathode } \text{–(1)}$$

$$4OH^- \rightarrow 2H_2O + 4e^- + O_2\uparrow \text{ anode } \text{–(2)}$$

PEM:

$$4e^- + 4H^+ \rightarrow 2H_2\uparrow \text{ cathode } \text{–(3)}$$

$$2H_2O \rightarrow 4H^+ + 4e^- + O_2\uparrow \text{ anode } \text{–(4)}$$

The hydrogen evolution reaction (HER) on cathode side requires two electrons stepwise transfer to generate one hydrogen molecule. On the contrary, the oxygen evolution reaction (OER) demands relatively more electrons for the reaction: four electrons stepwise transfer to produce one oxygen molecule. Thus, the OER on the anode side is usually considered as the battle-neck reaction, limiting the overall reaction speed of water electrolysis.[7] Common for both AWE and PEM systems, significant overpotential is generally needed to overcome the energy barrier at the anode side where the OER takes place. For this reason, the specific OER has been intensively studied for many decades in order to elucidate the underlying oxidation reaction mechanism, and several OER electrochemical catalysts have been developed and engineered to minimize the energy loss during water electrolysis.[6]

The cell configuration of AWE is shown in **Figure 1-1.** The best reported electro-catalyst on the anode electrode for AWE is iridium (Ir) or ruthenium (Ru) based materials.[8-10] However, since several materials including transition metal oxides also present an adequate stability when in contact with an alkaline solution, which introduces the possibility of using alternative catalysts with cheaper prices compared to noble metals.[11,12] Furthermore, the alkaline media with OH^- rich environment allows a more favorable kinetics for water oxidations at the anode side compared to the situation in acidic solution.[13] However, the low current density restricts the overall performance and practicability. Further improvement and study on designing a more effective electrochemical catalyst for alkaline water oxidation is necessary.

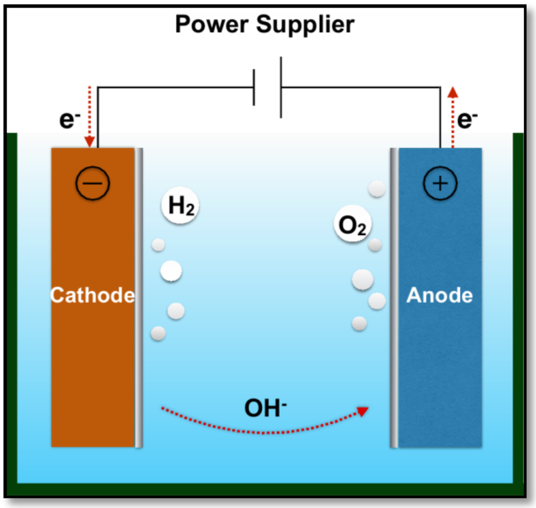

Figure 1-1. Working principle of AWE device.

In a typical PEM cell configuration (**Figure1-2)**, it usually requires a sold polymer electrolyte (SPE) membrane as the electrical insulation to separate the contact between anode and cathode, which is also responsible for the selective conduction of positive ions such as protons from anode to cathode, separation of product gases (H_2 and O_2), and support a local acidic environment. The PEM electroyzer is introduced to address the issues of partial load, low current density, and low pressure operation currently persecuting the performance of alkaline electrolyser AWE.[14] Compared with AWE, the acidic media enable PEM to perform a fast kinetics toward HER and a high-voltage efficiencies at high current densities. Furthermore, it has been demonstrated PEM can produce a ultrapure hydrogen gas at relatively high pressures (over 150 bar), offering the possibilities to store the hydrogen gas directly without further mechanical compression.[15] However, under this acidic environment of the PEM system, only few electrode materials can survive and present an acceptable stability. Therefore, the anodic and cathodic reactions (OER and HER, respectively) of PEM are generally catalyzed by noble metal-based catalysts, such as Pt, Ru and Ir based materials.[6] How to reduce the usage of those precious materials is the main issue for the PEM application.

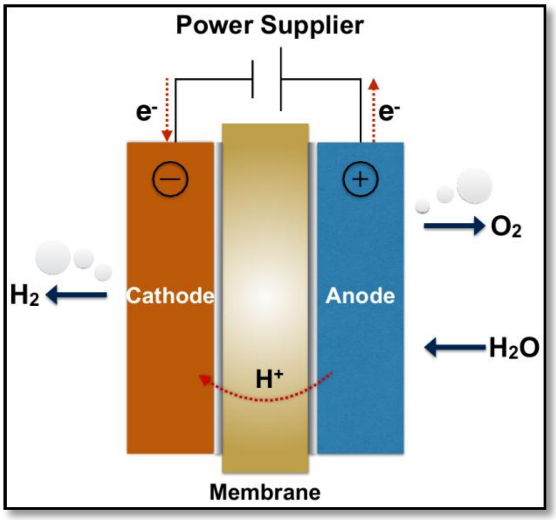

Figure 1-2. Working principle of PEM device.

Based on the above discussion, we can realize that for both alkaline and acidic water electrolysis systems, improving OER kinetics on anode side would be undoubtedly favorable to effectively generate H_2 and O_2 gases to widespread the market penetration and practicality. To date, the most reported OER catalyst which generally exhibits the best performance based on the evaluation between catalytic activity and long-term stability in no matter alkaline and acidic media is the noble metal, IrO_2. However, the scarce quantity and high price make it almost impossible to utilize this material on a large scale. To find a possible alternative catalyst with cheaper price but comparable activity and durability compared to that of IrO_2, researchers have shifted their attention on AWE system, in which the nature abundant materials such as transition metal oxides (cobalt, nickel, or iron)[16] and perovskite oxides[11,17] have been proved to be quite stable and active toward OER in alkaline media. Several strategies and method have also been proposed to tailor the activity of those non-precious catalysts. Based on this present perspective, the reaction mechanism and kinetics, and current issues discussed form fundamental aspects in catalyst materials for the OER is summarized and discussed.

1.2 Reaction mechanistic insight of oxygen evolution reaction

The most obvious indication to quantitatively describe the activity of the catalyst toward oxygen evolution reaction is the current density (i) under a particular applied voltage (V). Several experimental parameters could influence the measured i during electrochemical measurement, such as voltage sweep rate, substrate of electrode, and the surface roughness factor (or named as electrochemical active surface area, EASA), which should be carefully controlled when comparing the OER activity among various catalyst samples.[6] The general scientific concern of an electro-kinetic study is the determination of how i varies as a function of voltage, temperature, pH value, electrolyte strength and viscosity, and other experimental variables. Among these, the most important kinetic parameter is the relationship between V and i.[18] In a conscientious and careful electrochemical experiment, the V value is usually recorded in the scale versus a particular reference electrode designated as the starting voltage point, V=0. Based on this reference system, the applied external V on the system can be directly determined as the driving force to initiate the OER. In practice, the expected relationship between applied V and i for the most simplistic case of an outer-shell single-electron-transfer reaction of the reactant can be constructed. This scenario describes a simplified case that reactant (A) can be oxidized to an oxidation state (A^+) by obtaining a hole with positive charge (h^+) from the electrode in solution. A simplified reaction-coordinate energy diagram for the abovementioned heterogeneous single-electron oxidation reaction is illustrated in **Figure1-3**.[18]

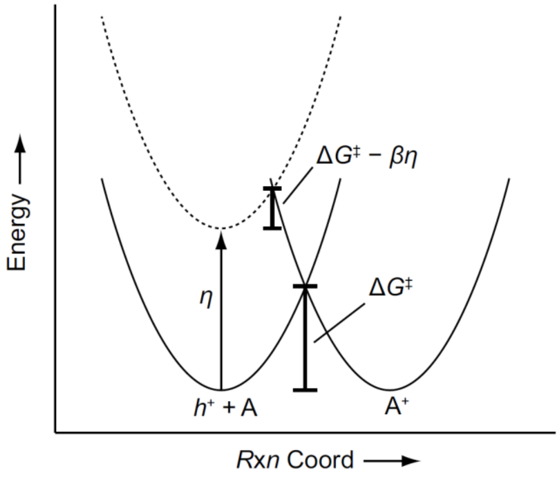

Figure 1-3. Simplified reaction-coordinate diagram for a heterogeneous single-electron oxidation reaction of A to A^+. h^+ represents a hole with a chemical potential equal to the Fermi level of the poised electrode. The activation barrier, ΔG‡, and overpotential, η, are in units of eV. Reproduced with permission from ref.[18] (Copyright © 2012 John Wiley & Sons, Inc.).

The chemical potential of the positive charge carrier h^+ is in line with the position of the Fermi level of the solid phase on the electrode, which can be directly manipulated by varying the applied V on the electrode. If the voltage of the electrode is equipoised to the theoretical thermodynamic potential for the oxidation of A to A^+, the driving force to push reactant to overcome the activation energy barrier (ΔG‡) will be zero, and the two energy curve wells will be isoenergetic. This situation is comparable to that of an electron-transfer self-exchange reaction in which the system also possesses no driving force. With the applied V gradually increasing on the electrode, the chemical potential of h^+ is also promoted. Thus, the energy well of the reactant (A) is risen as compared to the energy well of the product (A^+). The applied additional voltage, or denoted as overpotential (η), determines the driving force for electron transfer form electrode to the reactant and therefore which can be estimated by the difference in energy of the two minima points of the reactant energy which can be graphically realized in **Figure1-3**.[18]

In practice, most electrochemical measurements are always carried out with a practical reference (e.g., saturated Hg/HgO electrode, SCE) and the potentials recorded are subtracted with the thermodynamic value for the reaction to determine the overpotential, η. Meanwhile, in order to report the η value in an universal standard, the voltage is usually to converted in the scale versus the reversible hydrogen electrode, RHE, e.g., V_{SCE}^{o} = 0.241 V vs. SHE. Thus, let's take water oxidation reaction as the example, the recorded potential can be converted to the RHE scale using the following equation: $V_{RHE} = V_{SCE} + V^{o}_{SCE} + 0.059 \times \text{pH}$, and $\eta = V_{RHE} - 1.23$ V, in which 1.23 V is the standard thermodynamic value of potential for water electrolysis.

In a general condition, a portion of the overpontential energy applied on the system will go forward to lower the activation barrier for promoting the reaction, and the faction of the overpotential, usually defined as β, is known as the symmetry factor. On the contrary, the complementary factor, 1- β, represents the fraction of the overpotential which will go toward lowing the energy barrier for the opposite direction reaction. Based on the Erying equation, the activation energy barrier and reaction rate possess an exponential relationship in terms of that activation controlled current density will be exponentially scaled as a function of overpotential. In a single electron transfer reaction, current density, i, can be interpreted by the following equation:

$$i = i_0 \exp(\frac{\beta F \eta}{RT}) \text{ –(5)}$$

where F is the Faraday constant, R is the ideal gas constant, T is temperature in Kelvin scale, and i_0 is the exchange current density which represents the current rate at which the forward and back reactions simultaneously occur when η=0. To practically use this equation in electrochemical kinetics study, it is common to represent this equation is log scale:

$$\log(i) = \log(i_0) + \frac{\beta F \eta}{2.3RT} = \log(i_0) + \frac{\eta}{b} \text{ –(6)}$$

We purposely convert the equation to the relation between overpotential and current density:

$$\eta = b\log(i) - b\log(i_0) = blog(i) + Constant \text{ –(7)}$$

Where b is the Tafel slope, which is equal to:

$$b = \frac{2.3RT}{\beta F} = \frac{59mV}{\beta} \text{–(8)}$$

As mentioned, the symmetry factor (β) can be regarded as a description for the effect in the overpotential which can change the activation barrier. Thus, based on the simplified Marcus equation:

$$\beta = \frac{\partial G}{\partial \eta} = \frac{1}{2} + \frac{\eta}{2\lambda} \text{–(9)}$$

where λ is the reorganization energy. Based on the above equation,[18] we can learn that the Tafel slope is actually also a function of overpotential, which is expected to vary with the driving force increases. However, for most of the electrochemical systems, λ is excess then 1 eV in common. Therefore, the second term of the equation can be negligible, and thus, the β is usually treated as a constant of 0.5 for the normal range over the usual electrokinetic measurement. In such case, we can deduce the a Tafel slope of 120 mV per decade of current density (dec) will be expected at room temperature for a one-electron-transfer reaction. Although the exact value of b depends on a number of external parameters in the electrochemical measurement, extensive studies of the HER in which the reaction rate is limited by single electron transfer do exhibit Tafel slopes very close to the expected value of 120 mV/dec.

Tafel slope is an effective kinetic parameter which has been generally used as the indicator for the catalytic activity toward water electrolysis. For the point of view, it is useful to quantitatively evaluate the performance of the catalyst. For the OER mechanism which involves multi-electrons-stepwise-transfer reaction or even parallel reactions, the Tafel slope is defined as the dependency of the overpotential η

on the current density I in log space:

$$\frac{\partial \log(i)}{\partial \eta} = \frac{2.3RT}{\alpha ZF} \text{–(10)}$$

where Z is the number of transfer electrons in the rate-determining steps, and α is the charge transfer coefficient on the interface between catalyst and electrolyte. By the definition of the equ.10, a lower Tafel slope represents a faster increase of OER current with applied bias in terms of a better activity. Compared to equation (5), charge transfer coefficient (α), and symmetry factor (β) are two similar related parameters used in description of the kinetics of electrochemical reactions, and the only difference is that the β can be applicable only to an ideal one-electron-transfer reaction.

In general, no matter in acidic or in alkaline environments, the mechanistic schemes for the OER are composed by different elementary reactions, which involve several surface adsorbed intermediates. It has been accepted that the general OER mechanism in alkaline solution on the metal site (M) begins with a proton-coupled electron transfer from a surface-bound aquo species followed by an O-O bond formation,[19,20] which can be described as four elementary reaction steps and involve several surface

adsorbed intermediates:

Step 1 $$\text{M-OH}_2 + \text{OH}^- \rightarrow \text{M-OH} + \text{H}_2\text{O} + e^- \qquad \text{–(11)}$$

Step 2 $$\text{M-OH} + \text{OH}^- \rightarrow \text{M-O*} + \text{H}_2\text{O} + e^- \qquad \text{–(12)}$$

Step 3 $$\text{M-O*} + \text{OH}^- \rightarrow \text{M-OOH} + e^- \qquad \text{–(13)}$$

Step 4 $$\text{M-OOH} + \text{OH}^- \rightarrow \text{M-OH}_2 + \text{O}_2 + e^- \qquad \text{–(14)}$$

where M refers to the adsorption metal site on the catalyst.

In order to obtain a reliable Tafel slope, the measurement is usually carried out in the cycling voltammetry at a very slow scan rate, or using a quasi-stationary potentialstate measurement, i.e., hold the potential until the current achieves a steady-state. In such condition, we can then assure the only the RDS is irreversible step controlling the kinetic performacne whereas the other elementary steps exist in a quasi-equilibrium state. The particular elementary reaction step with the highest kinetic activation energy is regarded as the bottleneck for the overall

OER cycle, which is denoted as the rate-determining step (RDS). Therefore, the overall reaction rate, ν, will be identically equal to the rate of the RDS, which is given by:

$$\nu = \theta_M(a_{OH^-})\exp(\frac{\beta F\eta}{RT}) \text{ –(15)}$$

where a_{OH^-} refers to the activity of the hydroxide ion reactant in this step, and θ_M is the surface coverage of the exposed reaction sites. Now let discuss the Tafel slope for the specific RDS situation where the RDS could be step1, 2, or 3.[11,21]

If step 1 is turnover limiting process, then θ_M should approach to unity because the surface is covered with few accumulation of hydroxyl group, the impact of changes in potential on θ_M is negligible and can be treated as a constant. Thus, reaction velocity is directly proportional to the current density, so the Tafel slope can be obtained by taking partial derivative of eqn. 15 according to eqn. 10:

$$b = \frac{\partial\eta}{\partial\log(i)} = \frac{\partial\eta}{\partial\log(\nu)} = \frac{2.3RT}{\beta F} = \sim 120\ mV/dec \text{ –(16)}$$

where β = 0.5 due to the ideal single electron transfer reaction for each step, and temperature is 25 ^{o}C.

If step 2 is considered as the RDS, the reaction rate can be given as following:

$$\nu = \theta_{M-OH}(a_{OH^-})\exp(\frac{\beta F\eta}{RT}) \text{ –(17)}$$

where θ_{M-OH} is the surface coverage ratio of the hydroxyl group on the expose active sites.

Because the step 1 remains a quasi-equilibrium state, based on the Nernst equation, the ratio of the reactants, θ_{M-OH} on the right hand side and θ_M on the left hand side of the step 1 (eqn. 11) can be given by the follows:

$$\frac{\theta_{M-OH}}{\theta_M} = k(a_{OH^-})exp(\frac{F\eta}{RT}) \text{ –(18)}$$

where k is the equilibrium constant.

Combing Eqn. 17 and Eqn.18 gives:

$$\nu = \theta_M (a_{OH^-})^2 \exp[\frac{(\beta+1)F\eta}{RT}] \text{ –(19)}$$

Following this, the Tafel slope can be deduced by equ. 10:

$$b = \frac{\partial\eta}{\partial\log(i)} = \frac{\partial\eta}{\partial\log(\nu)} = \frac{2.3RT}{(\beta+1)F} = \sim 40\ mV/dec \text{ –(20)}$$

Unsing the same principle, if the reaction rate is constricted by step 3, Tafel slope can be calculated as following:

$$b = \frac{2.3RT}{(\beta+2)F} = \sim 24\ mV/dec \text{ –(21)}$$

The value of Tafel slope is an important indicator for determining the RDS of the catalytic reaction. However, sometimes, we cannot get a characteristic value of Tafel slope due to that fact that the reaction could be controlled by the mixed steps which all contribute to the RDS simultaneously. For example, a Tafel slope of 60 mV/dec is usually estimated for Co_3O_4 where the reaction may be controlled by the formation of peroxide intermediate (OOH*) among step 1 to step 3. An in-situ IR or Raman measurement will be useful to detect the intermediates on the catalyst for the determination of the RDS.

1.3 The descriptor of the electrocatalyst toward OER activity: Volcano diagram

The kinetic study focusing on RDS has played a central topic for many years. Recently, a new point of view has attracted massive attention in which the potential-determining step (PDS) has been proposed. Compared to RDS, PDS highlights the role of thermochemical aspects for the overpotential of OER. In the thermodynamic view, PDS represent the elementary step which requires the maximum change of Gibbs free chemisorption energy between two subsequent adsorbed intermediates (ΔG_{max}). Thus, the overpotential related to the PDS can be redefined under a standard condition at pH = 0 and U = 0 V versus RHE as:[13]

$$\eta^{OER} = \left(\frac{\Delta G_{max}}{e}\right) - 1.23\ V \quad –(22)$$

For an ideal catalyst, there will be no overpotential for an ideal catalyst due to the absence of thermodynamic hindrance without the consideration of the kinetic limitation. where the ΔG in each elementary step is all equal to 1.23 V . The energy diagram for an ideal catalyst is shown in **Figure1-4a**.[22]

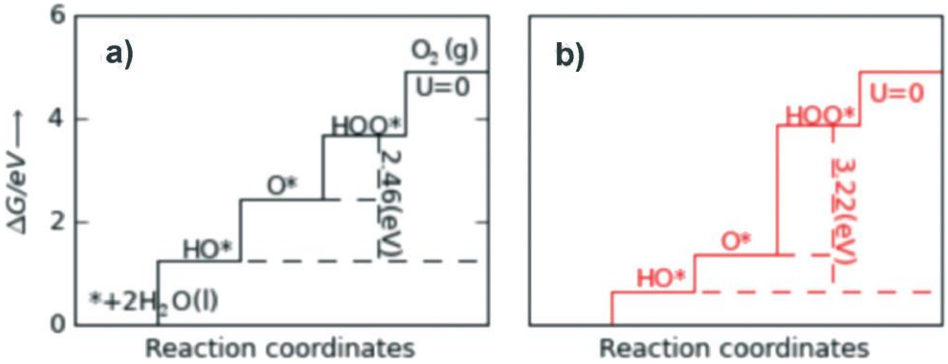

Figure 1-4. Standard free energy diagram for the (a) ideal catalyst and for (b) the real catalyst where PDS happens on the transition between O* and OOH* intermediates. Reproduced with permission from ref.[22] (Copyright © 2011 WILEY-VCH Verlag GmbH & Co. KGaA, Weinheim).

This energy diagram is constructed by density functional theory (DFT) calculations which usually focus on the surface adsorbed intermediates which can be denoted with the mark of *. Therefore, we can rewrite equation (11)-(14) with the standard Gibbs energy change of each elementary reaction and $\Delta G_{1\text{-}4}$(oxygenated species) represents the standard Gibbs energy of formation of each respective species:[22]

$$H_2O_{(l)} + M \leftrightarrow HO^* + H^+ + e^-,\ \Delta G_1 = \Delta G(HO^*) - \Delta G(H_2O) – eU + k_bT\ln(a_{H}+) \quad –(23)$$

$$HO^* \leftrightarrow O^* + H^+ + e^-,\ \Delta G_2 = \Delta G(O^*) - \Delta G(HO^*) – eU + k_bT\ln(a_{H}+) \quad –(24)$$

$O^* + H_2O_{(l)} \leftrightarrow HOO^* + H^+ + e^-, ^-, \Delta G_3 = \Delta G(HOO^*) - \Delta G(O^*) - eU + k_bT\ln(a_{H^+})$ –(25)

$HOO^* \leftrightarrow M + O_{2(g)} + H^+ + e^-, \Delta G_4 = \Delta G(O_2) - \Delta G(HOO^*) - eU + k_bT\ln(a_{H^+})$ –(26)

For a real catalyst which generally possesses a PDS with a relatively largest ΔG, the corresponding energy diagram can he represented in **Figure 1-4b**. where a perovskite OER catalyst, $LaMnO_3$, as the example. We can clearly find that the ΔG between the reaction steps associated with O* and HOO* intermediates is the largest, and thus, which can represent the RDS for $LaMnO_3$. Since the formation of HOO* intermediates is the RDS, An ideal catalyst for the OER would can be optimized to be able to minimize the unfavorable energetic relationship between the crucial intermediates of the RDS, and an common approach to enhance the electrochemical activity can be achieved by reducing the energy barrier for this step. Besides, the ΔG between different elementary steps is highly related in terms of a linear depending relation of the chemi-sorption/desorption existing between these surface intermediates. In other words, if one of the elementary ΔG is changed, all the others will be affected, too. Based on this truth, we will be able to describe the OER activity by plotting a function of only one adsorption energy of intermediate species, e.g., the O* species, or an energy difference between two interested species, e.g., ΔG0(O*) − $\Delta G_0(HO^*)$. Thus, a volcano relation between the activity (turning off frequency (TOF), overpotential (η), current density (I) at a assigned voltage, etc.) and the chemisorption energy of O* intermediate species or a particular energy variation of $\Delta G_0(O^*) - \Delta G_0(HO^*)$ can be plotted as shown in the **Figure 1-5**[13] and **Figure 1-6**.[22]

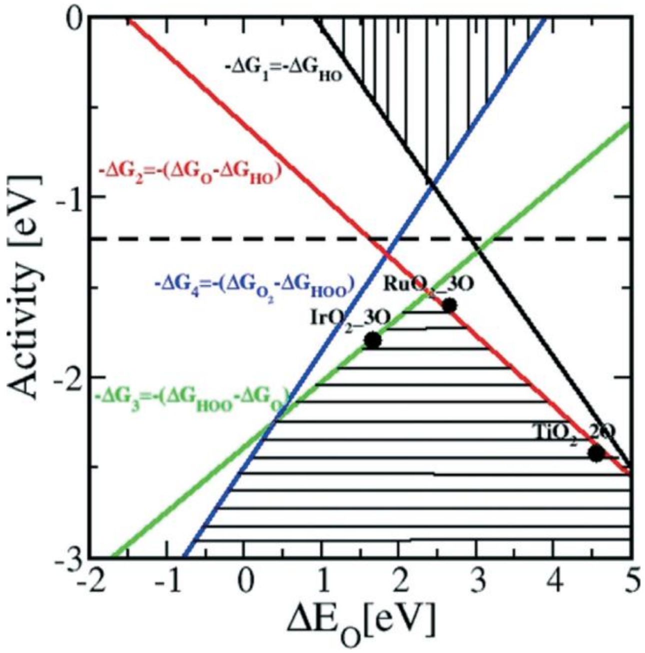

Figure 1-5. Theoretical OER activity, defined as the negative change of the Gibbs free energy (−ΔG), of the four reaction steps described in eqn. 23 to 26 as a function of the oxygen binding energy. Reproduced with permission from ref.[13] (Copyright © 2006 Elsevier B.V. All rights reserved).

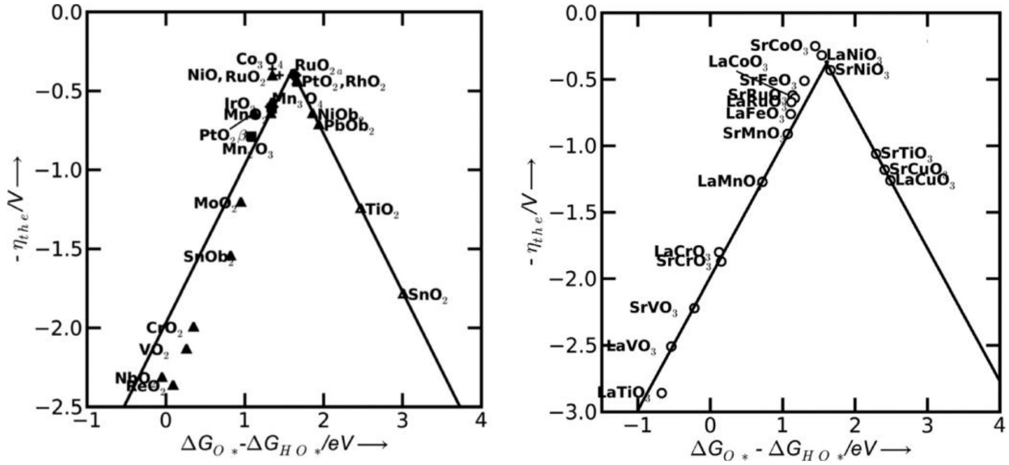

Figure 1-6. Theoretical overpotential(η) for oxygen evolution vs. the difference between the standard free energy of two subsequent intermediates (ΔG$_0$(O*) − ΔG$_0$(HO)) for various binary oxides (left) and perovskite oxide (right). Reproduced with permission from ref.[22] (Copyright © 2011 WILEY-VCH Verlag GmbH & Co. KGaA, Weinheim).

This volcano plot, which shows the OER activity based on the standard four reaction steps described by the eqn. 23-26 as a function of the chemisorption energy, is an useful tool to rank the activity among different catalyst. For example, in **Figure 1-5**, it indicates f a catalyst with a too weak or too strong O* surface binding energies, the corresponding OER activity would be limited by the O* (red line) or the HOO* (green line) formation steps, respectively. i.e., RuO_2 binds O* a little too weakly, while TiO_2 binds O* too strongly. The optimum catalyst should sit on the summit of the volcano which the intensity of O* binding energy is perfect right with a maximum catalytic performance. It is worth to mention that a similar concept has been proposed for the pervoskite based material (e.g., $LiBO_3$) where the -OH bonding strength on the edge atom, B, could be adjustable in terms of the catalytic activity by changing the number of electrons occupying the anti-bonding orbitals.[23,24]

As indicated in the Chapter 1.1, nature abundant catalyst with cheaper price but comparable activity and durability compared to that of noble metal, such as transition metal oxides (and perovskite oxides have attracted an great attention as a possible alternative toward OER in alkaline media. In this thesis, spinel cobalt oxide, Co_3O_4, is particularly chosen as the studying subject due to the following reasons:

(1) Cobalt based material is cost-effective and environmentally friendly. It is one of the most common seen transition metal, which usually can be found together with iron, nickel and copper mineral.

(2) The crystal structure of spinel is interesting, which is composed by one tetrahedral M^{2+} ion and two octahedral M^{3+} ions. Both geometrical metal ions can be easily substituted, enabling a possibility to modulate the activity by changing different substitutes.

(3) According to the volcano plot in **Figure1-6**, Co_3O_4 sits on the top of the volcano, indicating its potential to be an optimum catalyst toward OER.

(4) It is convenient to do the synthesis of spinel Co_3O_4 through hydrothermal, sol-gel, or electro-deposition methods, and the shape of Co_3O_4 is alterable ranging for 1 dimensional (1-D) rod or tube to 3-D cubic structure. Besides, it has been reported this material can be easily to be grown on any conductive substrate, which greatly facilitates its practical utility.

The material properties and currently encountered issues of spinel Co_3O_4 as the electrocatalyst will be discussed in the next section.

1.4 Spinel metal oxide and their OER activity

The general formulation of spinel is $A^{2+}B^{3+}{}_2O^{2-}{}_4$ in which the crystalline structure is in the cubic (or isometric) crystal system. The oxide anion, (O^{2-}), arrange in a close-packed cubic lattice, and the metal cations, A and B, occupy the octahedral and tetrahedral sites in the lattice. The detail of spinel structure is illustrated in **Figure 1-7**.[25] Although the oxidation state of A and B in the spinel structure are (II) and (III), respectively, other combinations incorporating divalent, trivalent, or even tetravalentcations are possible. The metal cations could be any of the first raw of the transition metals.[26] The common seen elements are magnesium (Mg), zinc (Zn), iron (Fe), manganese (Mn), Cobalt (Co), chromium (Cr), titanium (Ti), and other metal such as silicon (Si) and aluminum (Al) are also possible.[25] The anion is normally oxygen. However, when other chalcogenides constitute the anion role, the as-formed spinel structure is usually referred to as a thiospinel.[27]

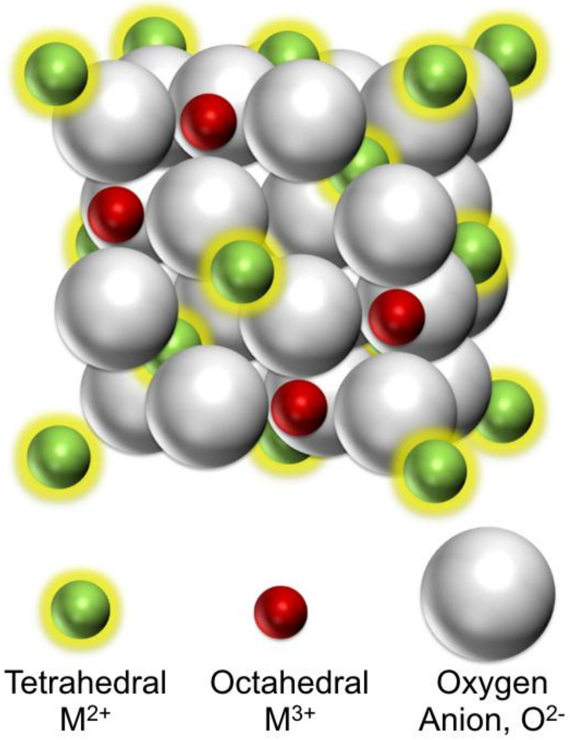

Figure 1-7. The illustration of normal spinel structure.

Co_3O_4 has been demonstrated as a promising transition metal catalyst with good efficiency and corrosion stability for the OER. The electronic spin state of the d-orbital configuration in the transition metal oxide is an interesting knowledge which can theoretically affect the bonding energy with oxygen (ΔG_{O*}), i.e., the OER performance can be adjusted by changing the spin state. The strategy to enhance the OER performance has been intensively discussed for perovskite based materials.[11] Generally, the crystal field stabilization energy (CFSE) theory[28] can be used to predict the spin state of the d-orbital due to the intensity of energy fiend of the bonding ligand, and oxygen anion is usually regarded as the weak ligand with low fiend intensity. Thus, the bonded transition metal center should process an electronic state with high spin state, and vice versa. However, Co_3O_4 is one of the exceptional cases, where the d-orbital electronic state in Co^{3+} with octahedral geometry is usually low spin, yet the electronic state tetrahedral Co^{2+} is still high spin.[28] Thus, such different could affect the ranking of electron binding energy for Co^{3+} and Co^{2+}. One of the famous examples is X-ray photoelectron spectroscopy for Co_3O_4. Usually, it is expected that the ion with higher oxidation state should possess a higher electronic binding energy. However, for Co_3O_4, the biding energy of Co^{2+} is just slightly higher than that of Co^{3+}. The higher binding energy of Co^{2+} state might be ascribed to the effect of the interaction between the cobalt p-orbital and d-orbital. The splitting pattern and electron configuration for d-orbital octahedral ligand (Co^{3+}, d^6) and d-orbital tetrahedral ligand (Co^{2+}, d^7) are illustrated as follows (**Figure 1-8**):[28]

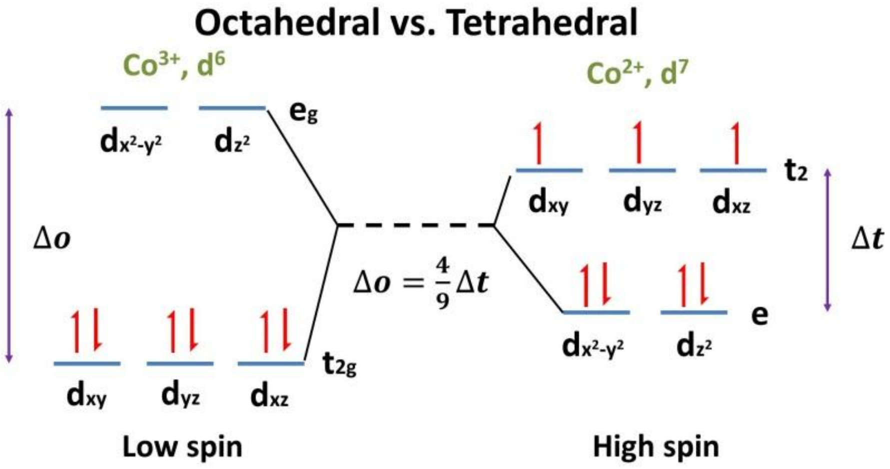

Figure 1-8. The electronic configuration of octahedral Co^{3+} (d^6) and tetrahedral Co^{2+} (d^7).

It can be seen that for Co^{3+}, the d_{xy}, d_{yz}, and d_{xz} orbitals all possess a pair of electrons, constructing a low spin electronic configuration. However, for Co^{2+}, the d_{xy}, d_{yz}, and d_{xz} orbitals only have one electron for each (high spin electronic configuration), which means that the remaining electron spin momentum can symmetrically affect the inner p_x, p_y, and p_z orbitals, thus raising the p-orbital electron binding force. Therefore, it requires more X-ray energy to kick out the electron from the p-orbital. D. Briggs et al.[29] have studied the binding energy of various cobalt complexes and demonstrated that the Co $2p_{1/2}$–Co $2p_{3/2}$ spin–orbit splitting increased with the number of unpaired electrons. The $2p_{1/2}$–$2p_{3/2}$ separation was found to be 15.0 eV for diamagnetic Co^{3+}, 15.4 eV for low-spin Co^{2+}, and 16.0 eV for high-spin Co^{2+}. Moreover, C. Altavilla[30] also revealed that it was invalid to infer the change of oxidation state through using the change of binging energy of Co_{2p} peaks if there was a change in spin state. Consequently, the analysis of Co 2p X-ray photoelectron spectra in all studies was made difficult by the fact that cobalt can exist in different coordination geometries and different spin states for the same oxidation state. The de-convoluted Co $2p_{3/2}$ peaks were assigned to Co^0, Co^{3+}, and Co^{2+} from low to high binding energy. This assignment has been revealed in some literatures [P. Vialat et al. *Adv. Funct. Mater.* **2014,** *24,* 4831[31]; T. Choudhury et al. *J. Phys. D: Appl. Phys.* **1989,** *22,* 1185[32]], where the binding energy of the Co^{3+} with octahedral structure (low spin) was assigned to lower than that of Co^{2+} with tetrahedral geometry (high spin).

With applying a positive bias on Co_3O_4 in an alkaline solution, a phase transformation from spinel to layer structured cobalt oxyhydroxide (CoOOH) is generally expected according to the Co-H_2O Pourbaix diagram (**Figure 1-9**).[33]

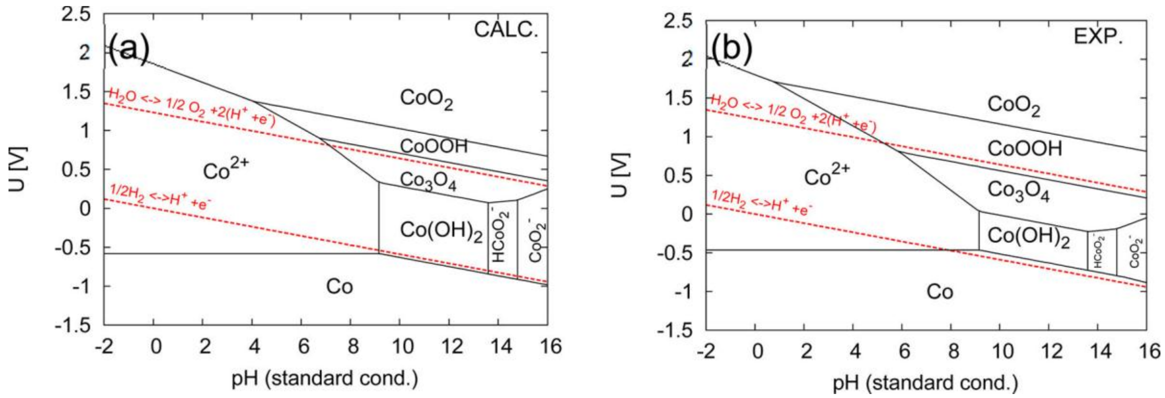

Figure 1-9. Pourbaix diagrams of bulk phases based on (a) the calculated formation free energies of solid compounds and corrected experimental free energies of aqueous ions of Chivot et al.[34] and (b) based only on experimental formation free energies of Chivot et al. Reproduced with permission from ref.[33] (Copyright © 2013, American Chemical Society).

The anodic peak prior to the onset of OER in a typical cycling voltammetry curve (**Figure 1-10**) is usually ascribed as the evidence for the bulk readox reaction with a phase evolution based on the

Purbaix diagram (Co^{2+}/Co^{3+} with $Co(OH)_2/CoOOH$ transformation, or Co^{3+}/Co^{4+} with $CoOOH/CoO_2$ transformation).[26,35-39,34]

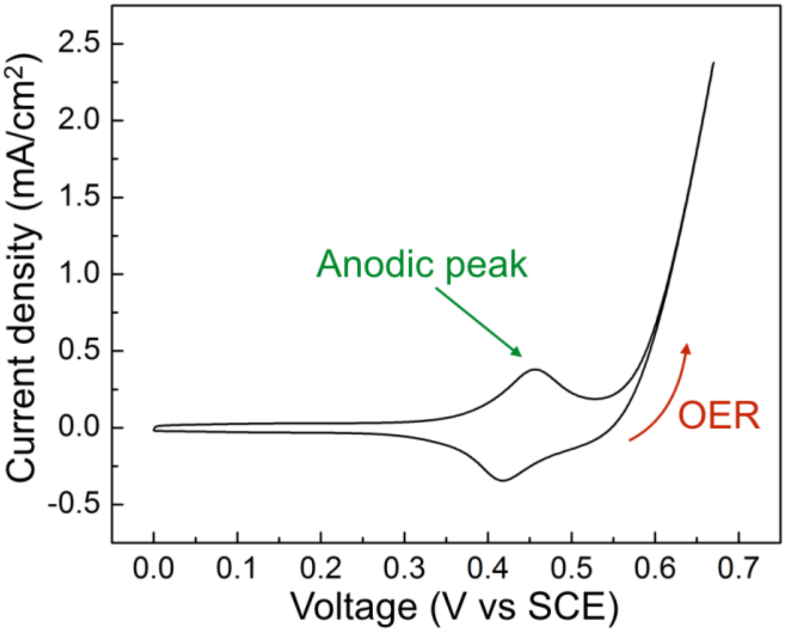

Figure1-10. A typical cycling voltammetry curve of Co_3O_4 in 1 M KOH, where saturated calomel electrode (SCE) was used as reference. From which, an obvious anodic peak prior to the OER onset can been easily identified.

Thus, people generally believe this the newly formed hydrated cobalt oxide layer acts as the main active species rather than pure spinel Co_3O_4 surface. Thus, several simulation works toward the OER activity of Co_3O_4 were calculated based on the cobalt oxyhydroxide structures. For example, the OER activity of two different crystallographic surface of The Co(0112) and Co(1014) has been calculated by DFT method as shown in **Figure 1-11**.[33] In addition, it was also found the most promising dopant appear to be V for Co(0112) surface and Ni for Co(1014) surface for a long-term application with an enhanced stability.

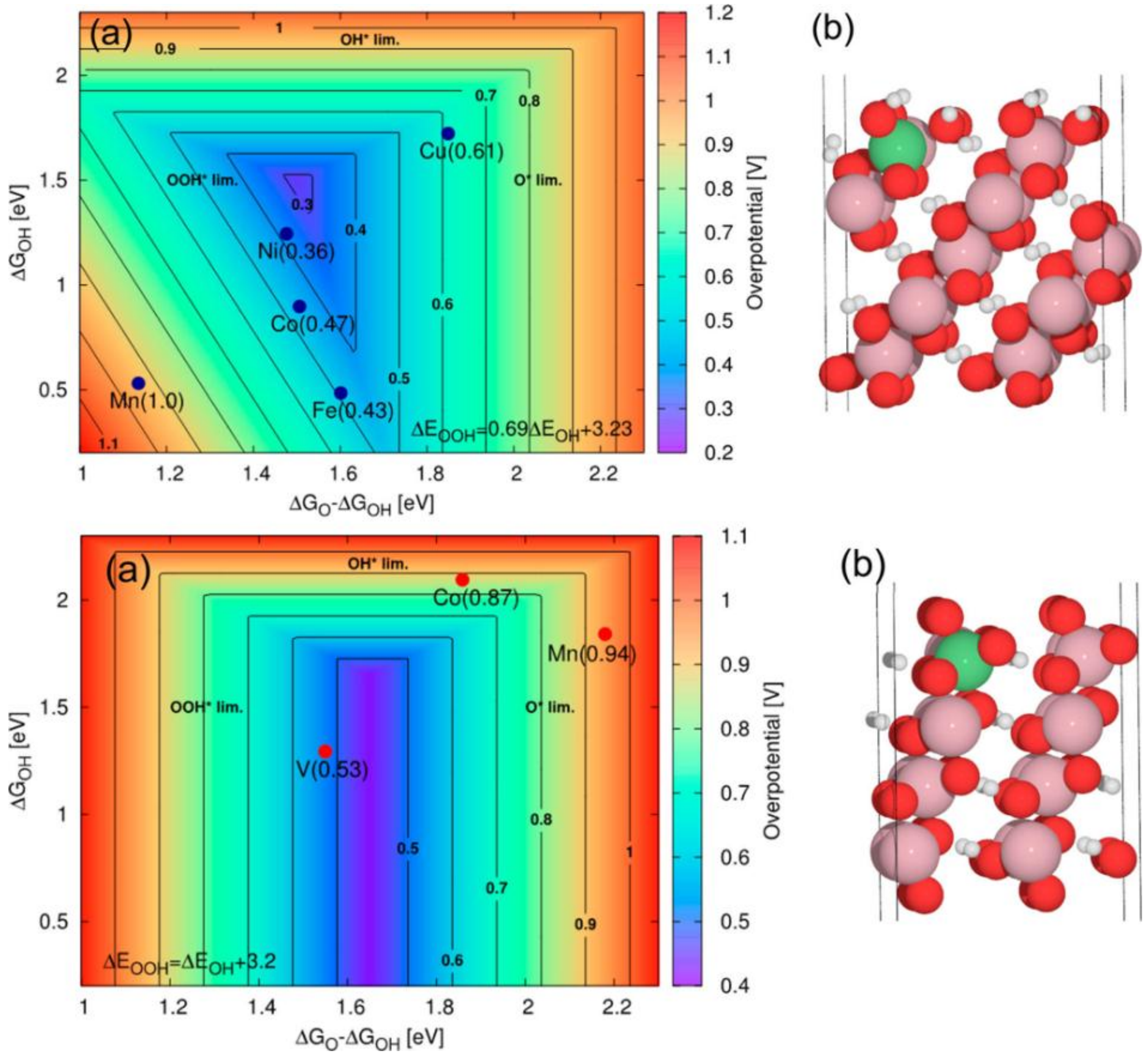

Figure 1-11. (a) 2D map of theoretical overpotentials (η) for the doped $(10\bar{1}4)$ surface (upper panel) and for the $(01\bar{1}2)$ surface (lower panel) of β-CoOOH as function of $\Delta G_O - \Delta G_{OH}$ and ΔG_{OH}. The individual values of η are indicated in brackets. The contour map is constructed assuming $\Delta E_{OOH} = E_{OH} + 3.2$ eV. For the $(10\bar{1}4)$ surface (upper panel), improvement in activity relative to the undoped surface is obtained for Ni with η = 0.36 V and for Fe with η = 0.43 V. For the $(01\bar{1}2)$ surface (lower panel), the improvement relative to the undoped surface is obtained for vanadium with η = 0.53 V. Only the dopants with η < 1 V are shown. (b) The corresponding atomic system with a green sphere indicating the position of the dopant. Reproduced with permission from ref.[33] (Copyright © 2013, American Chemical Society).

Substituting the Co ions with other material ions is an attracting strategy to intrinsically modulate the catalytic activity because this approach can be easily done by simply changing the precursor during the synthesis. Nickel doped Co_3O_4 (denoted as $Ni_xCo_{3-x}O_4$, $0 \le X \le 1$) nano-wires free-standing on the Ti foils has performed an enhanced electrochemical catalytic activity with an obviously decreased Tafel slope and promoted current density.[40] Cu doped Co_3O_4 (denoted as $Cu_xCo_{3-x}O_4$, $0 \le X \le 1$) also showed a good performance and long-term durability due to the interatomic Cu-Co interaction.[41,42] Besides, Fe,[43,44] Mn,[45] Ni,[46,47] or Zn[48] substituted Co_3O_4, or even tri- ternary elements spinel, e.g., Co-Ni-Cu,[49] Co-Cu-Zn,[50] Co-Nu-Cr,[50] Co-Ni-Mn,[51] etc. in which a synergistic effect combining all the benefits from different components is expected have been demonstrated which can exhibits an improved activity. A triangle plot of the OER activity versus the compositions of a ternary catalyst based on a massive experimental data is usually presented as the active descriptor for the ternary catalyst. In order to answer the underlying reason for the enhanced OER activity in these substituted Co_3O_4 spinel compounds, some physical factors such as increased corrosion stability, enlarged the surface activity area, and decreased electrical resistance are usually mentioned. Density functional theory (DFT) calculation is common employed to build up the relation between the ratio of the components and the chemisorption energy of the intermediates in terms of the activity. An example of Ni-Fe-Al, Ni-Al-Co, and Al-Co-Fe spinel is shown in **Figure1-12**.[52]

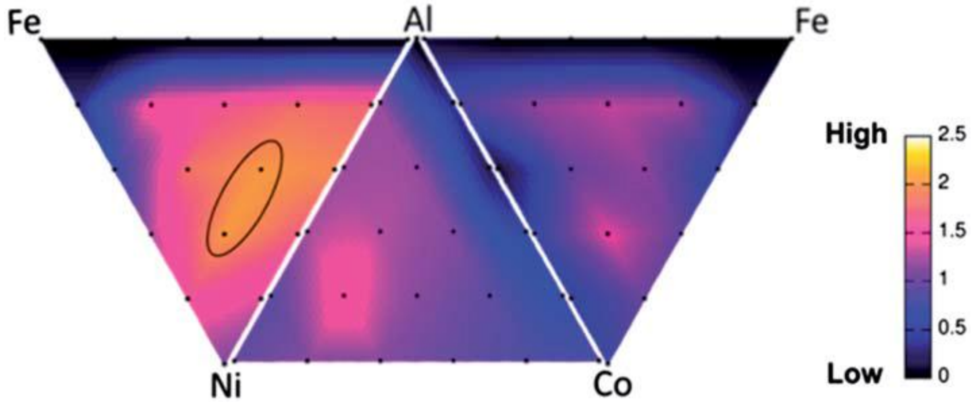

Figure 1-12. Ternary diagrams showing relative electrocatalytic water oxidation activity of thin-film mixed metal oxides at pH 13, 670 mV vs. Ag/AgCl (overpotential = 406 mV). Reproduced with permission from ref.[52] (Copyright © 2014, Royal Society of Chemistry).

Apart from the composition, the annealing process and the choice of the substrate/support also may influence to catalytic activity. It has been generally accepted that a higher temperature treated catalyst with a higher degree of crystallinity could be less active yet more stable compared to what prepared under a lower temperature. It is suggested the defect on the surface of catalyst may act as the active site for OER.

It has also been indicate a high temperature treatment (> 350 °C in the literature) could lead to a diffusion of the substrate material ion to the top of the cobalt oxide layer, affecting its intrinsic catalytic performance. A further possible influence from the substrate/support on the catalyst has been investigated recently. A consequently decreased TOF of the galvanostatically deposited cobalt based catalyst as a function of the substrate in the order of Au > Pt > Pd > Cu > Co.[53] It was suggested the oxidation state of cobalt easily tended to be higher on the more electronegative substrate, such as Au in this case, which acted as an electron sink.[54] Thus, a higher oxidation state of the active metal center may lead to a nucleophilic attraction for the incoming OH^-, facilitating the OER process. However, such significant influence form the substrate toward OER activity could be observed for only few monolayers of the loading catalyst.

To rule out the possibility of the influence caused by the substrate/support toward the OER activity on the catalyst, it is worth to mention that the utilization of some Ni based substrate (i.e, Ni foam) or carbon based material as support which has been mixed with the catalyst to enhance the conductivity should be avoided. It has been warned that the Fe impurities in the KOH electrolyte could strongly affect the activity of Ni toward OER, which make it hard to differentiate the origin of the OER current from the studying catalyst or the Ni substrates. Besides, In addition to Ni, carbon could be thermodynamically oxidized at a positive voltage as low as 0.207 V vs. RHE. Therefore, under a typical operating condition for the OER (> 1.23 V vs. RHE), carbon will suffer a serious anodic corrosion. As a consequence, a combining high anodic current generated from both catalytic water oxidation and carbon corrosion would be observed during the experimental measurements.

1.5 Research Motivation

Substituted Co_3O_4 has been extensively studied as a promising approach to enhance the catalytic activity toward OER. Among various substitutes, Ni dopant has been demonstrated as an effective element to enlarge the surface roughness factor (or electrochemical active surface area, EASA), improve the electrical conductivity of the catalyst, and reduce the activation energy barrier of the RDS in terms of an earlier onset and a higher current density. Typically, a Ni Substituted Co_3O_4 with a constant ratio of Ni/Co = 1/2 (denoted as $NiCo_2O_4$) is generally studied in the Ni-Co catalyst system because this structure is the most common seen and stable Ni-Co oxide spinel. It gives rise to our interest to further optimize the OER performance of Ni substituted Co_3O_4. Meanwhile, an enlarged electrochemical active surface area can benefit the current density. Thus, a method to simultaneously dope Ni into Co_3O_4 and increase the roughness factor (R_f) on the catalyst should be worthy developed.

Even though Co_3O_4 is a well-known spinel material with one Co^{2+} sitting at the tetrahedral site, and two Co^{3+} ions occupying at the octahedral sites, to date, none of the study particularly focuses on the discussion the possibility of that the electrochemical OER activity could be geometrical dependent. For instance, the structure of $NiCo_2O_4$ is an inverse spinel (space group: $Fd\overline{3}m$) where Ni^{2+} ion occupies the octahedral sites and two Co^{3+} ions occupy the remaining tetrahedral and octahedral sites.[55] Such kind of geometry should intrinsically influence the OER activity compared to that of the normal spinel structure, i.e., the catalytic features of both normal and inverse spinel structures should be different from each other. However, such geometrical factor has been usually ignored. To study the possibility of the geometrical-site-dependent activity in the Co_3O_4 toward OER, the advanced in-situ techniques, synchrotron radiation X-ray light absorption and diffraction (denoted as XAS and XRD, respectively) are employed to real-time study the detail of the crystalline information during water oxidation. To understand the geometrical-site-dependent activity in Co_3O_4, we selectively replace the tetrahedral Co^{2+} and octahedral Co^{3+} with non-active species, and thus, the activity of individual geometrical Co ion in Co_3O_4 spinel could be revealed. As a result, we should be able to discover the connection between the activity and the position where the substituted metal ions/Co ions occupy.

Apart from the OER activity, as discussed in the chapter 1.4, a phase evolution is usually expected on Co_3O_4 surface with the increase of bias as indicated by the electrochemical feature of CV curve where an obvious anodic peak appears prior to the rise of OER current during. This newly formed phase is generally assigned to the layered CoOOH structure, and it should be the true active species responsible to the OER activity rather than the Co_3O_4 spinel itself. Recently, the work by Prof. Strasser discussed the surface change on Co_3O_4 via using *in-situ* technique including XAS and XRD during OER. They found that an only sub-nanometer amorphous hydrated cobalt oxide, $Co_x(OH)_y$, could be formed after OER onset. However, no layered CoOOH could be found before the onset as indicated by the rise of the anodic peak. This discrepancy, again, gives rise to our attention to the reaction mechanism on the surface of Co_3O_4. Is there really a phase evolution taking please on Co_3O_4? The Pourbaix diagram is purely constructed by thermodynamic calculation, and this approach totally rules out the possibility of serious kinetic influence in terms of a slow phase transformation. It should be a very crucial issue because this expected CoOOH layer is believed to dominate the OER activity. Besides, if there is almost no layered CoOOH structure which could be formed on Co_3O_4 during OER, then what is the underlying reaction represented by the anodic peak before OER onset?

In this thesis, we will try to dig out the whole underlying scenario of Co_3O_4 toward OER, including the influence of the geometrical substituted metal ions, geometrical-dependent activity of individually tetrahedral Co^{2+} and octahedral Co^{3+} in normal Co_3O_4 spinel, and the authentic surface reaction on Co_3O_4 which is associated to the OER activity. It should be mentioned that to avoid the influence generated from the substrate, we carefully choose the fluoride doped tin oxide ($F:/ZnO_2$, FTO) as the conductive substrate for all the experiments due to its high stability and inert surface property under an acid/alkaline environment. Also, the OER performance, or OER current, is normalized by the geometrical area of the working electrode for a fair comparison. We believe such kind of systematic study based on the deeply understanding of Co_3O_4 could provide a fundamental and crucial knowledge for the reasonable design of superior catalyst.

1.6 Overall objective

The overall objectives of this thesis are listed as follows:

(1) Optimization of the performance of Ni substituted Co_3O_4 with a simultaneously induced shape evolution for a high roughness factor.

(2) Investigation of the connection between substituted geometrical Ni ions and OER activity in Co_3O_4 spinel structure.

(3) Deep understanding of the geometrical-site-dependent activity of pure Co_3O_4 with normal spinel structure by an advanced *in-situ* technique using synchrotron X-ray light source.

(4) Development of various facile *in-situ* cells and revealing the underlying reaction on the Co_3O_4 surface before the rise of the OER current via multiple *operando* examinations.

(5) Concluding the most possible mechanism of OER on Co_3O_4 under the electrochemical condition with the increase of the bias.

Chapter 2. Shape-evolution with enhanced OER activity: surface Ni^{3+} induced formation of active nickel oxyhydroxide (NiOOH) on Spinel Ni-Co Oxide for efficient water oxidation.

2.1 Purpose and motivation to synthesis Ni doped Co_3O_4 spinel as OER catalyst with enhanced activity.

It has been known that over the past few years, great efforts have been devoted to the electrochemical study of OER in pursuit of sustainable and efficient energy conversion and storage. The inherent sluggish kinetics of the four-electron transfer process[7,56,57] makes OER a key step for energy conversion and energy storage devices including water electrolysor devices, photoelectrochemical water splitting cells, and rechargeable metal-air batteries.[58-62] To overcome this rate-limiting step, extensive research efforts have been dedicated to develop efficient OER electrocatalysts with high activity and low overpotential.[63] Among which, noble metal-based oxides, such as RuO_2 and IrO_2, are regarded as the best OER electrocatalysts,[8,9] but the scarcity of ruthenium and iridium limits their widespread applications. Accordingly, materials based on first-row transition metal oxides that are naturally abundant and catalytically active have received considerable attention, since these metal oxide materials show great promises as alternative electrocatalysts for OER.[12,64,65] For example, cobalt-based materials such as $Co(PO_3)_2$,[66] Co_3O_4,[67] $NiCo_2O_4$,[46,47] $Zn_XCo_{3-X}O_4$,[48] Mn-Co oxide,[45] and $Ni_XCo_{3-X}O_4$[40,68] have been extensively studied as competent electrocatalysts for water oxidation reaction because of their good catalytic activity and excellent stability under oxidizing conditions in alkaline medium. Catalytic reaction commonly takes place on the surface of a catalyst, which indicates that activities and current density of electrocatalysts can be influenced by the surface area and geometric structure. Furthermore, cobalt-based oxides for OER are usually employed in the form of thin films or agglomerates bound together by polymer binders,[69,70] which leads to the low surface area and ineffective electron-mass transfer and significantly restricts the electrocatalytic activity due to poor contact between active material/electrolyte and boundaries among particles. As a result, it is highly desirable to design three dimensional (3D) electrocatalysts with large surface area, good electroconductivity, and high porosity for OER.[48,71,72]

Since Ni has been intensively studied as the promising dopant to promoting the catalytic activity on Co_3O_4 as mentioned in Chapter 1.4, thus, we tried to optimize the performance of Co_3O_4 via Ni doping and simultaneously construct a highly rough surface on Ni-Co oxide. A solution chemical method to construct a Ni-Co oxide (NCO) OER electrocatalyst with unique hierarchical 3D nanosheets (HNSs) structure was then reported here. The as formed NCO-HNSs showed high surface area with a Ni^{3+}-rich surface, delivering a stable current density of 10 mA/cm^2 for OER at an overpotential of ~0.34 V with a Tafel slope of 51 mV/decade, which was kinetically better than traditional $NiCo_2O_4$ catalyst where the majority of nickel ion is Ni(II).[73]

2.2 The detail of synthesis of Co_3O_4 nanorods (Co_3O_4-NRs), Ni-Co oxide nanorods (NCO-NRs) and Ni-Co oxide hierarchical nanosheets (NCO-HNSs) on FTO substrates, characterization of the physical properties, and the electrochemical Measurements.

All chemicals were of analytical grade, purchased from Sigma-Aldrich and used without any further purification. In a typical synthesis, calculated amounts of $Co(NO_3)_2\cdot 6H_2O$ and $Ni(NO_3)_2\cdot 6H_2O$ with an appropriate molar ratio x of Ni/Co (x = 0/1 for Co_3O_4-NRs, x = 1/1 for NCO-HNSs) were mixed in 30 mL of deionized water at room temperature with the total metal ion concentration fixed at 0.02 M. Afterwards, 10 mmol of urea were introduced into the mixture under vigorous stirring. The as-prepared homogeneous solution was transferred into a Teflon-lined stainless steel autoclave. One piece of FTO substrate (F:SnO_2, Tec 15, 10 Ω/□, Hartford Glass Company), ultrasonically cleaned for 30 min in a mixed solution of deionized water, acetone, and 2-propanol with volume ratios of 1 : 1 : 1, were placed at an angle against the wall of the Teflon-liner with the conducting side facing down. The hydrothermal reaction was conducted at 120 °C for 3 hours in a temperature-controlled oven. After synthesis, the autoclave was cooled to room temperature under flowing air. The FTO substrate was rinsed with deionized water and dried in ambient air, followed by calcined at 300 °C for 2 h in atmosphere. The growth of NCO-NRs on FTO substrate is similar to that described for NCO-HNSs but with additional 6 mmol of NH_4F.

The crystallographic information of Co_3O_4-NRs, NCO-NRs and NCO-HNSs were examined using X-ray diffraction with Cu Kα irradiation (λ = 1.5406 Å). The morphology was studied with field emission scanning electron microscopy (FESEM, JSM-6700F) and transmission electron microscopy (TEM, JEM-2100). The compositional information was probed via X-ray photoelectron spectroscopy (XPS, ESCALAB 250) with Al Kα mono chromatid flood and Mg Kα radiation (1253.6 eV) with a double pass cylindrical mirror analyzer. X-ray absorption spectroscopy (XAS) measurements of the Ni-Co LDH and oxide samples were collected by employing synchrotron radiation light source at 01C1 beam line of the National Synchrotron Radiation Research Center (NSRRC), Taiwan. Measurements were made at the Ni K-edge (8333 eV) and the Co K-edge (7709 eV) with the sample held at room temperature, in which the home-made *in-situ* cell was designed for this experiment and electrochemical analysis was operated in identical conditions as all electrochemical measurements.

s Before collecting electrochemical data, the working electrodes were cycled at least 20 times between 0 and 0.6 V versus SCE at a scan rate of 5 mV/s to achieve stable current densities. The roughness factor (R_f) was estimated from double-layer capacitance charging curve using cyclic voltammetry in a small potential range (0.18 to 0.24 V vs. SCE), in which the double layer capacitance was determined from the slope of the capacitive current (I_{cap}) at the midpoint of the scan range (0.21V) versus the scan rate through $C_{dl} = I_{cap}/(dE/dt)$, where C_{dl} is the double layer capacitance and dE/dt is the scan rate.[74] R_f was calculated through dividing the slope by 60 μF/cm^2 (capacitance of a smooth surface).[75] Electrochemical impedance spectroscopy (EIS) measurements were performed by applying an AC voltage with 10 mV amplitude in the frequency range of 1 MHz to 1 kHz. OER polarization curves were collected at a scan rate of 1.0 mV/s and the long-term stability was examined via applying an overpotential of 0.37 V on working electrode for 18 hours.

2.3 Material characterization on Ni doped Co_3O_4 spinel

All the Ni doped Co_3O_4 spinel, Co_3O_4-NRs, NCO-NRs, and NCO-HNSs were grown on fluorine-doped tin oxide (FTO) substrate via urea hydrolysis of mixed metal nitrates followed by calcination in air. **Figure 2-1a&b** shows the X-ray diffraction (XRD) patterns of calcined Co_3O_4-NRs and NCO-NRs, indicating their pure spinel structure (JCPDS file nos. 20–0781, *a* = 8.110 Å). **Figure 2-1c** reveals the as-prepared NCO-HNSs films grown on FTO substrate before the thermal treatment. Two substantial diffraction peaks at 33.7° and 59.3° were observed in addition to the diffraction peaks from FTO, which could be attributed to the formation of rhombohedral Ni-Co layered double hydroxide.[76] In present study, a chemical bath co-deposition strategy of Ni and Co was employed to prepare Ni-Co oxide hierarchical nanosheets while in the reaction system, urea was decomposed into CO_2 and NH_3 in early stage and further reacted with metal ions to produce hierarchically rhombohedral Ni-Co layered double hydroxide on FTO. After calcination, as shown in **Figure 2-1d**, all diffraction peaks can be well indexed as the spinel phase of Ni-Co oxide in addition to the typical peaks derived from FTO and the morphology of the film were kept nearly unchanged. This phenomenon means that a remarkable topotactical transformation took place from Ni-Co layered double hydroxide (LDH) to spinel Ni-Co oxide when the as-prepared Ni-Co LDH was calcined at 300 °C for 2 h in atmosphere. Because of removing water and hydroxyl groups during thermal treatment, this formation of metal oxide could be regarded as a topotactical process which was also revealed in other layered hydroxide systems[77-79] including the Co_3O_4-NRs and NCO-NRs. The morphologies of all Ni-Co oxide samples showed no significant change during calcination, since topotactical process offers a minimal re-organization of the Ni/Co atoms in the crystal.[77]

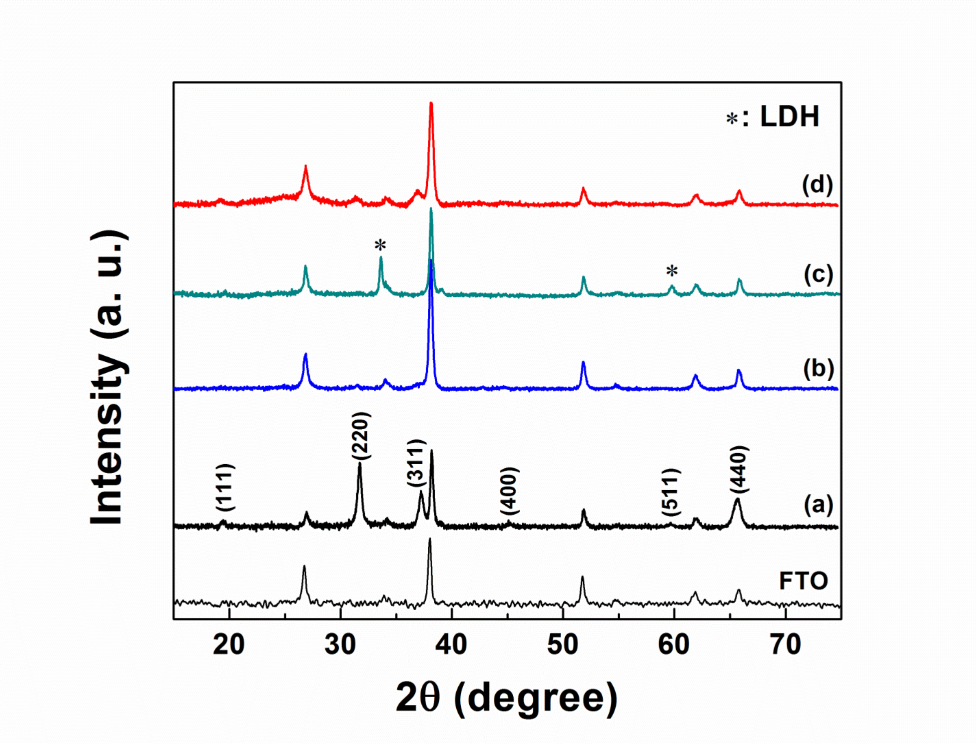

Figure 2-1. XRD patterns of (a) Co_3O_4-NRs, (b) NCO-NRs, (c) NCO-HNSs before calcination and (d) NCO-HNSs after calcination. Reproduced with permission from ref.[80] (© 2015 WILEYVCH Verlag GmbH & Co. KGaA, Weinheim).

To conduct the growth mechanism of NCO-HNSs, the reaction-time-dependent morphology evolution was studied in detail. The top-view and side-view FESEM images of NCO-HNSs obtained with various durations of hydrothermal reaction are shown in **Figure 2-2** and **Figure 2-3**, respectively. When the reaction time was shorter than 90 min, no film was formed on FTO substrate and the FTO remained transparent. The nanosheet film started to grow after 90 min of hydrothermal reaction, in which each nanosheet was composed of numerous thin nanosheets stacking together on their basal planes, standing perpendicular to the FTO substrate (**Figure 2-2a**) with the film thickness of ~500 nm (**Figure 2-3a**). Once the time of hydrothermal reaction was further increased to 120 min, the nanosheet film reached an average thickness of approximately 1 μm (**Figure 2-3b**) and the individual nanosheet reached a thickness of 200 nm (**Figure 2-2b**). It is worth mentioning that the thickness of nanosheet film (**Figure 2-3c and 2-3d**) and the thickness of individual nanosheet (**Figure 2-2c and 2-2d**) were unable to be further increased through increasing the reaction time, but further increase in reaction time caused the nanosheets to partially dissolve on the basal plane of nanosheets accompany with the formation of tiny secondary nanosheets upon the surface of primary nanosheets to form a hierarchical nanostructure, while the secondary nanosheets were grown on primary nanosheet arrays by a dissolution-recrystallization process.

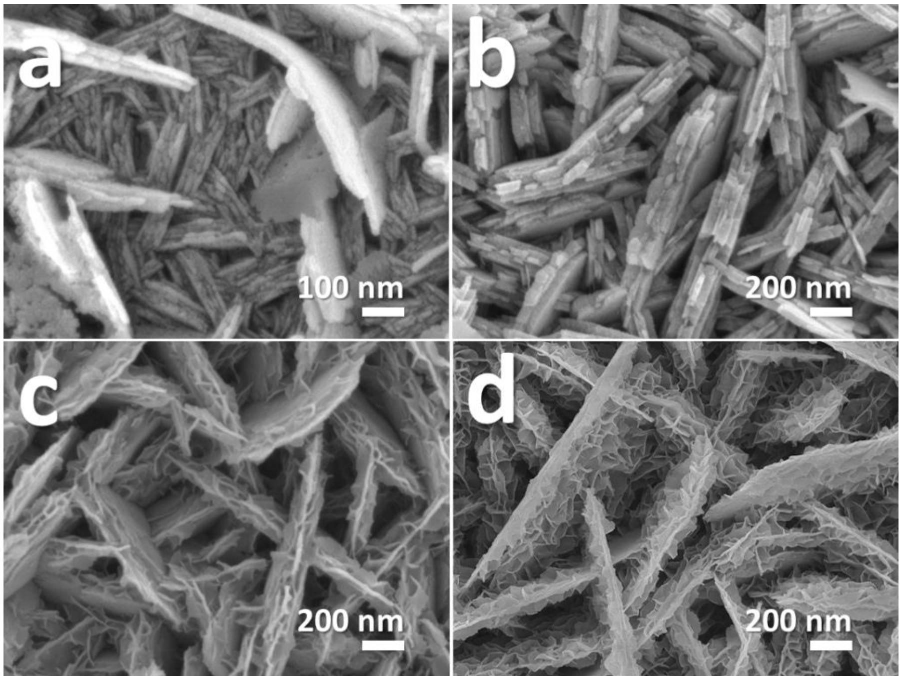

Figure 2-2. FESEM images of NCO-HNSs synthesized after different durations of hydrothermal reaction: (a) 90 min, (b) 120 min, (c) 150 min, and (d) 180 min. Reproduced with permission from ref.[80] (© 2015 WILEYVCH Verlag GmbH & Co. KGaA, Weinheim).

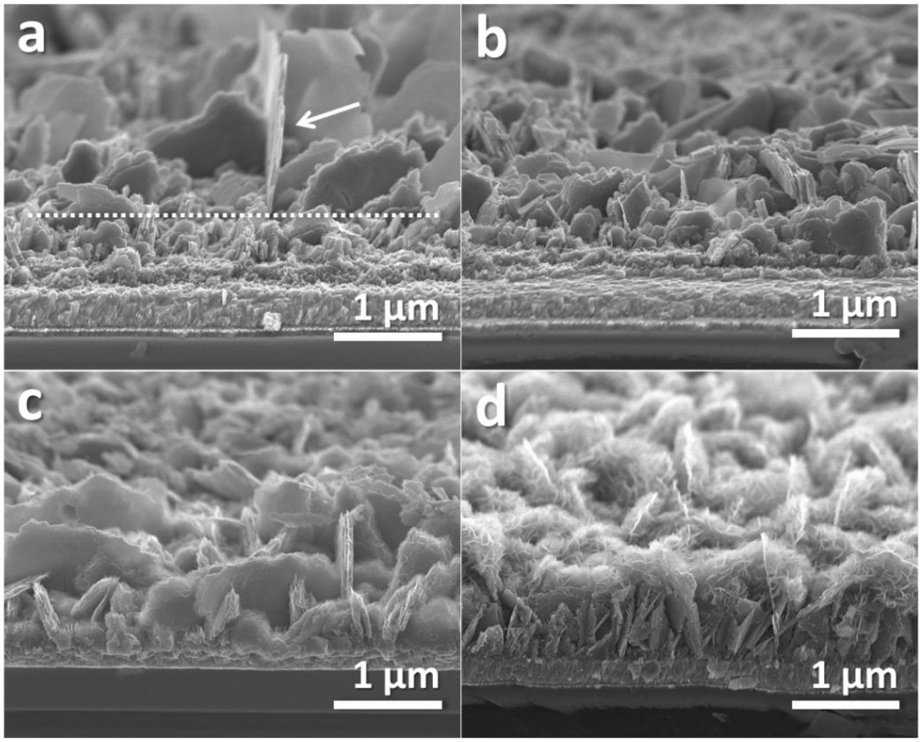

Figure 2-3. Cross-sectional FESEM images of NCO-HNSs synthesized after different durations of hydrothermal reaction: (a) 90 min, (b) 120 min, (c) 150 min, and (d) 180 min. Note: The growth of NCO-HNSs was hard to be precisely terminated at different durations, which caused the formation of some huge sheet-like structures during the cooling process as indicated in Figure 2-3a. Reproduced with permission from ref.[80] (© 2015 WILEYVCH Verlag GmbH & Co. KGaA, Weinheim).

Hierarchical Ni-Co LDH nanosheets acted as starting template for the topotactic atomic re-organization. In the case of absence of NH_4F, the resulting products became 1D nanorod arrays instead of hierarchical nanostructures in both Co-based and Ni/Co-based synthesis (**Figure 2-4a-d**). In this one-step self-template growth method, the super-saturation of Ni and/or Co ions can be remarkably suppressed through effectively coordinating with NH_3 and/or F^- ions, which leads to a considerable decrease in concentrations of metal ions in the reaction system and alters the growth of Ni-Co LDH. Consequently, NH_4F not only acted as a coordinating ligand to slow down the growth rate of Ni-Co nanostructures, but also mediated the dissolution and re-crystallization process to induce the growth of secondary nanosheets on primary nanosheet arrays (**Figure 2-4e&f**). Accordingly, the as-prepared NCO-HNSs film was composed of interconnected nanosheets standing nearly perpendicular to the FTO substrate, where the small secondary nanosheets grown on primary nanosheet arrays to form a hierarchical nanostructure. The growth of secondary nanosheets also significantly increased the surface area, which was represented as R_f factor estimated by double layer capacitance method (**Figure 2-5**), and the result was summarized in **Table 1-1**.

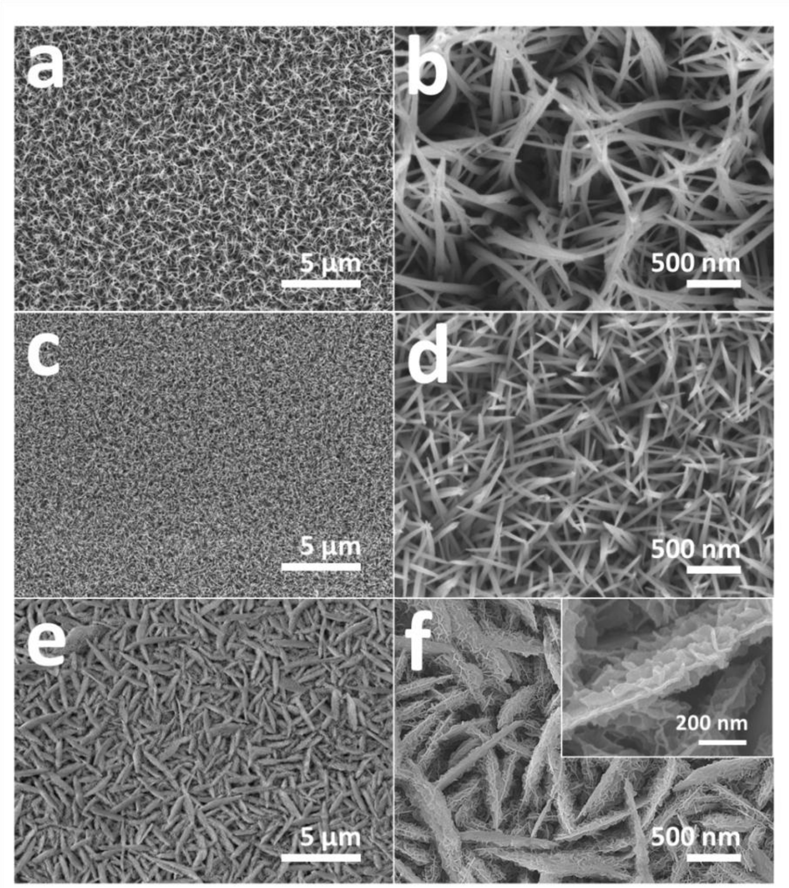

Figure 2-4. FESEM images of Co_3O_4-NRs arrays(a & b), NCO-NRs arrays(c & d), NCO-HNSs arrays. Reproduced with permission from ref.[80] (© 2015 WILEYVCH Verlag GmbH & Co. KGaA, Weinheim).

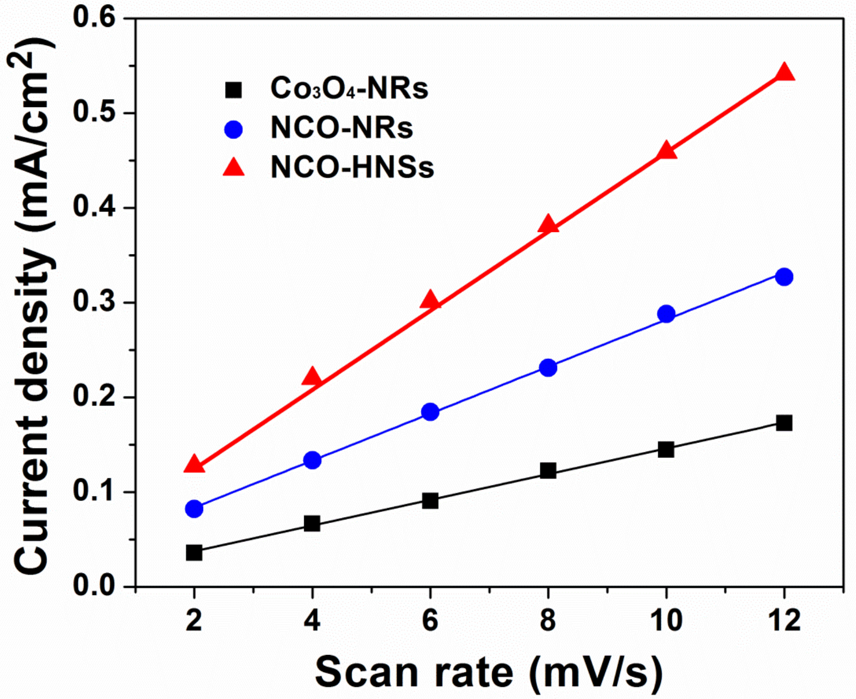

Figure 2-5. Dependence of the capacitive current vs. scan rate for Co_3O_4-NRs, NCO-NRs, and NCO-HNSs. Reproduced with permission from ref.[80] (© 2015 WILEYVCH Verlag GmbH & Co. KGaA, Weinheim).

Figure 2-6 shows the TEM images of the NCO-HNSs film detached from FTO substrate. As displayed in **Figure 2-6a&b**, the bottom part of the NCO-HNSs connecting to FTO was substantially rough and porous, and was composed of lots of small particles that were derived from thermal decomposition of carbonate intercalated Ni-Co LDH. This phenomenon can be attributed to the topotactic atomic re-organization from Ni-Co LDH to spinel Ni-Co oxide, which can also been seen on the Co_3O_4-NRs and NCO-NRs samples (**Figure 2-7**). **Figure 2-6c&d** show the TEM images of the body of NCO-HNSs. It could be clearly observed that tiny ultrathin nanosheets were uniformly distributed on the entire surface. The ultrathin secondary nanosheets had smooth surfaces (**Figure 2-6e**), resulted from their ultrathin nature which facilitated the release of tensile stress during calcination.[81] High-resolution TEM (HRTEM) image as shown in

Figure 2-6f reveals clear lattice fringes with interplanar spacings of d_{331} = 0.26 nm and d_{220} = 0.28 nm, which interlaced with each other at an angle of 31.5° and matched with the spinel Ni-Co oxide phase (JCPDS file nos. 20–0781, a = 8.110 Å).

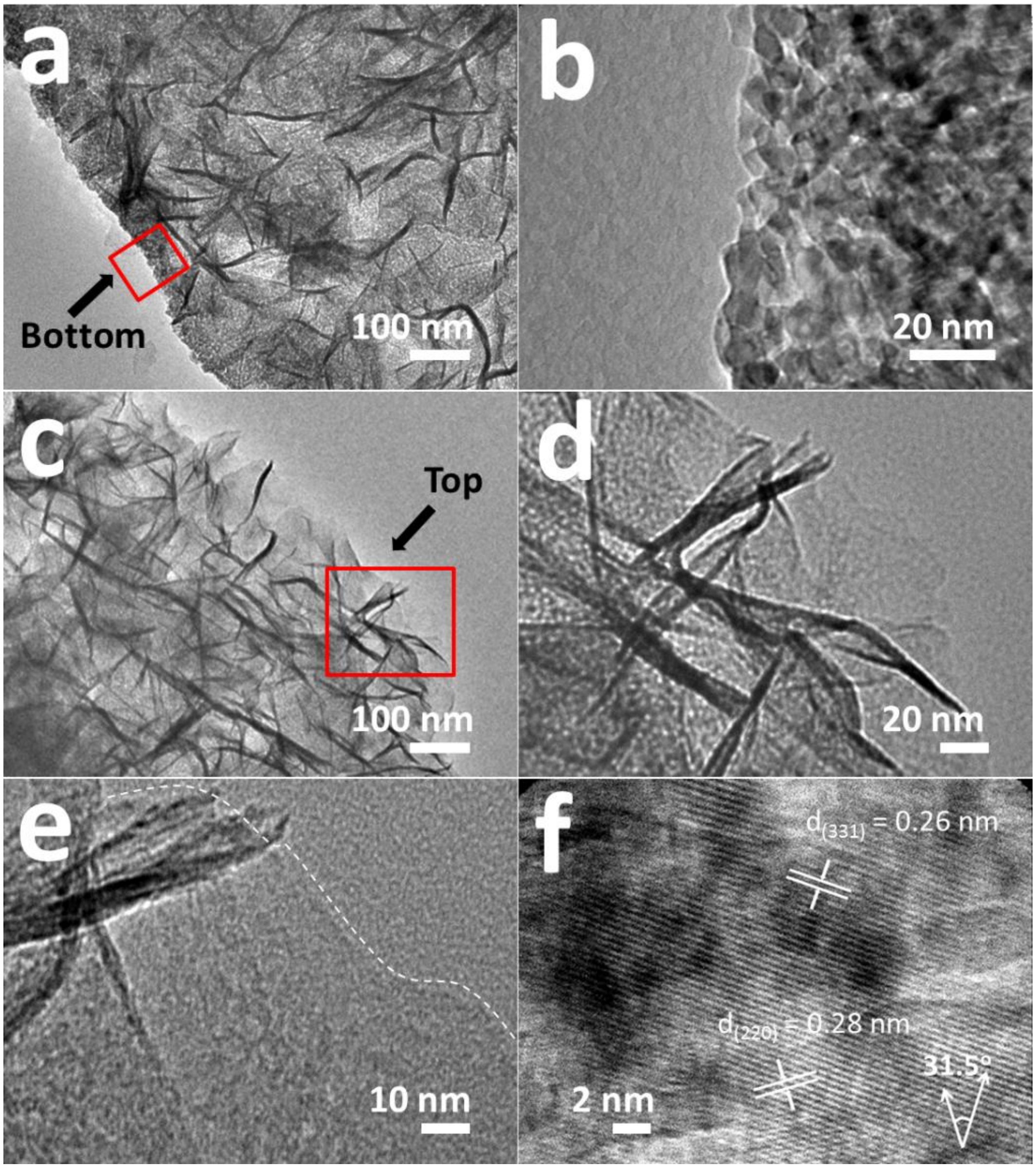

Figure 2-6. (a) & (b) TEM images of NCO-HNSs showing the bottom connecting FTO substrate, (c) & (d) TEM images of NCO-HNSs showing the main body, (e) high-magnification TEM image, and (f) HRTEM image of NCO-HNSs. Reproduced with permission from ref.[80] (© 2015 WILEYVCH Verlag GmbH & Co. KGaA, Weinheim).

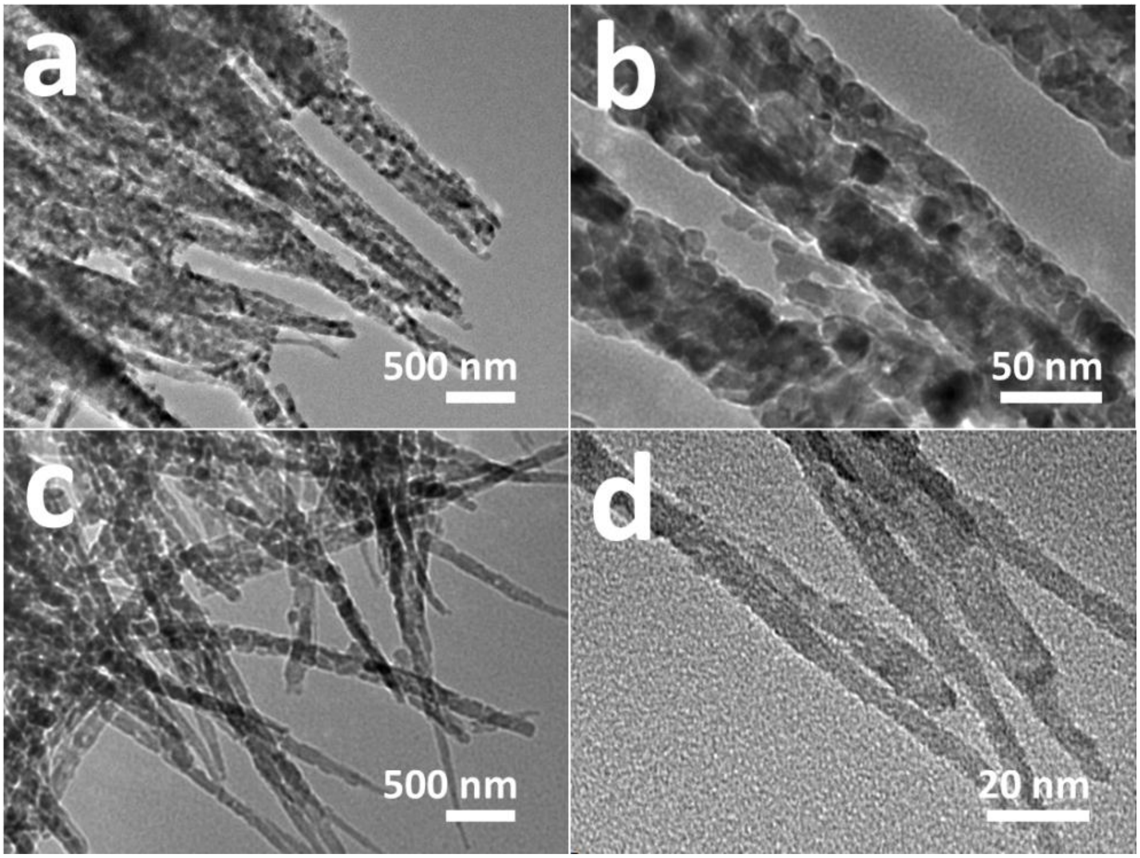

Figure 2-7. TEM images of Co_3O_4-NRs (a & b), and NCO-NRs (c & d). Reproduced with permission from ref.[80] (© 2015 WILEYVCH Verlag GmbH & Co. KGaA, Weinheim).

The composition and chemical valence states of the samples were probed by X-ray photoelectron spectroscopy (XPS). To compare the chemical valence state of cobalt, Co_3O_4 nanorods (Co_3O_4-NRs) were used as a reference. As shown in **Figure 2-8a**, Co $2p_{1/2}$ can be de-convoluted into Co^{2+} (796.18 eV) and Co^{3+} (794.57 eV) for all samples.[82] Note that NCO-HNSs possessed stronger Co^{2+} signal than Co^{3+}. In addition, NCO-HNSs also showed stronger cobalt satellite peak at 802.67 eV as well as the widest FWHM of Co 2p peak as compared to that of NCO-NRs and Co_3O_4-NRs (**Table 1-1**), suggesting that surface of NCO-HNSs was made of higher percentage of Co^{2+} than Co^{3+},[83] which was different from that of both NCO-NRs and Co_3O_4-NRs. In the case of NCO-HNSs, the intensity of Ni^{3+} $2p_{3/2}$ peak was much stronger than that of the Ni^{2+} $2p_{3/2}$ peak with Ni^{3+} $2p_{3/2}$ binding energy (854.03 eV) comparable to the binding energy of Ni^{3+} occupied in the octahedral site of Ni_2O_3,[84] suggesting that the majority of the nickel at the NCO-HNSs surface was Ni^{3+} (**Figure 2-8b**). **Figure 2-8c** shows the O 1s spectra of all samples, in which the first peak with a lower binding energy in the range of 529.66 – 529.94 eV could be assigned to lattice oxygen in spinel oxides.[83,85,86] The second peak with a higher binding energy at 531.30 eV was attributed to the formation of oxygen-Ni^{3+} bond.[87] Clearly, NCO-HNSs have the highest Ni^{3+} content on the surface as compared to that of both NCO-NRs and Co_3O_4-NRs, which is consistent with the observation from the case of Co 2p and Ni 2p spectra.[88] We would like to point out here that the Ni^{3+} rich surface for NCO-HNSs was resulted from the growth of secondary nanosheets on primary nanosheet arrays through the dissolution-recrystallization process since Ni^{2+}-rich surface appeared when a shorter hydrothermal reaction with a higher intensity of Co^{3+}. The change of the relative intensity between Co^{2+}/Co^{3+}, Ni^{2+}/Ni^{3+}, and O of the NCO-HNSs with reaction time extending was shown in **Figure 2-8d-f**.

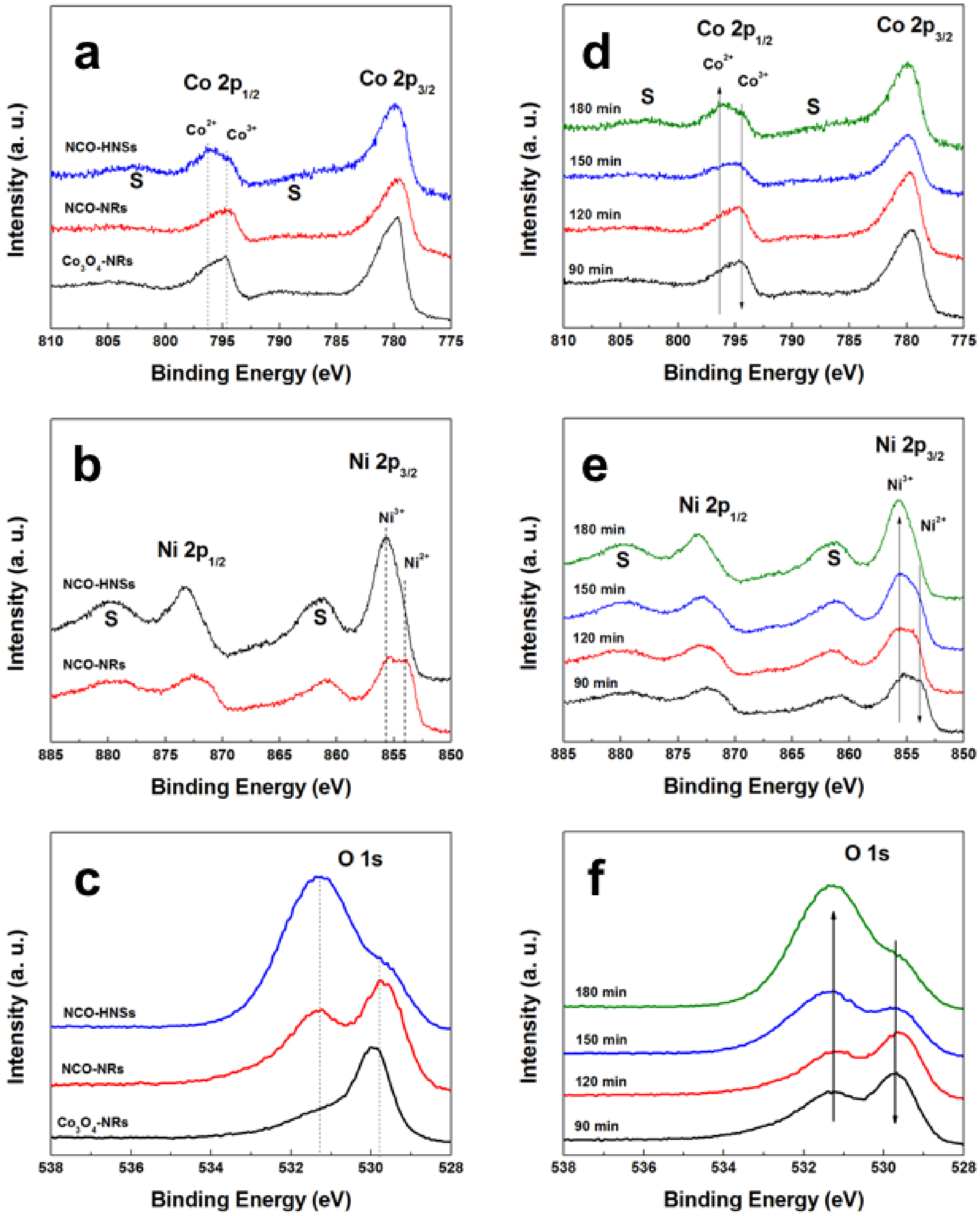

Figure 2-8. XPS spectra of (a) Co 2p, (b) Ni 2p, and (c) O 1s for Co_3O_4-NRs, NCO-NRs, and NCO-HNSs where S represents satellite peak. XPS spectra of (ad) Co 2p, (e) Ni 2p, and (f) O 1s for NCO-HNSs synthesized after various durations of hydrothermal growth where S represents satellite peak. Reproduced with permission from ref.[80] (© 2015 WILEYVCH Verlag GmbH & Co. KGaA, Weinheim).

Table 2-1. Physical properties of theCo_3O_4-NRs, NCO-NRs, and NCO-HNSs electrocatalysts. Reproduced with permission from ref.[80] (© 2015 WILEYVCH Verlag GmbH & Co. KGaA, Weinheim).

	Co_3O_4-NRs	**NCO-NRs**	**NCO-HNSs**
Ni/Co in growth solution	0/1	1/1	1/1
FWHM of Co 2p [eV]	2.69	2.95	3.26
Roughness factor ($R_f \times 10^3$)	0.23	0.41	0.68

2.4 Electrochemical properties and catalytic activity of NCO-NHSs toward water oxidation

Electrochemical impedance spectroscopy (EIS) was employed to examine the charge transfer kinetics across the electrode (**Figure 2-9**). The fitting results as shown in **Table 2-2** revealed a reduced series resistance (Rs) for NCO-NRs and NCO-HNSs, indicating improved conductivity of the electrode material via Ni introduction. Aside from a stringent requirement for high activity, excellent durability is another key factor for electrocatalyst development. The polarization curve confirmed the enhanced OER electrocatalytic activity for NCO-HNSs by showing a lower overpotential required to oxidize water at a desired current density (**Figure 2-10a**). The overpotential required to drive a current density of 10 mA/cm^2 for OER decreased from ~0.45 V for Co_3O_4-NRs to ~0.35 V and ~0.34 V for NCO-NRs and NCO-HNSs, respectively. Tafel slope is a principal kinetic parameter to realize the electrochemical behavior especially for the rate determining step of the re-arrangement and deprotonation of OH^- at low overpotential regime for OER.[89] The Tafel slope for Co_3O_4-NRs and NCO-NRs were 65 mV/decade and 54 mV/decade, respectively (**Figure 2-10b**), suggesting that Ni incorporation in NCO-NRs enabled a faster deprotonation of OH^- as compared the Co_3O_4-NRs. The Tafel slope for NCO-HNSs further decreased to 51 mV/decade while the enhanced OER performance was attributed to the introduction of nickel into NCO and the majority of Ni was Ni^{3+}. Additionally, the growth of secondary nanosheets on primary nanosheet arrays further increased the surface area(a higher R_f value compared to that of NCO-NRs), which should also contribute to enhanced OER activity for NCO-HNSs. It should be noting that the R_{CT} and R_S on electrodes of substrate-supported active materials should be coupled to each other. Therefore, the Tafel slope is also influenced by the electric resistance of the active materials as well as the reaction mechanism. To make a fair comparison among those catalysts, the current density was normalized by the R_f value as shown in **Table 2-2**, which indicated a higher activity per active site on NCO-HNSs (Ni^{3+} dominated) compared to that of NCO-NRs (Ni^{2+}/Ni^{3+} mixture). Chronoamperometric studies showed that the NCO-HNSs were stable in alkaline medium (**Figure 2-10c**) with current loss less than 4 % at an overpotential of 0.37 V after 18 hours of continuous oxidation reaction. To disclose the relaction between the superior activity with the substituted Ni^{3+} ion in the NCO-HNSs, in-stiu X-ray absorption spectroscopy (XAS) method was then carried out.

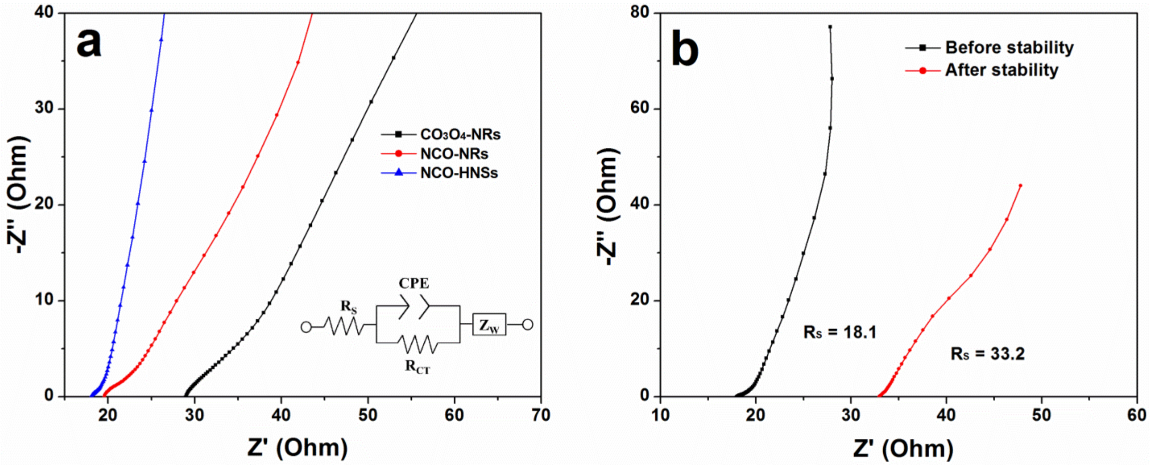

Figure 2-9. Nyquist plots of Co_3O_4-NRs, NCO-NRs, and NCO-HNSs electrodes in 1 M NaOH solution at open circuit potential before (a) and after (b) stability test. Reproduced with permission from ref.[80] (© 2015 WILEYVCH Verlag GmbH & Co. KGaA, Weinheim).

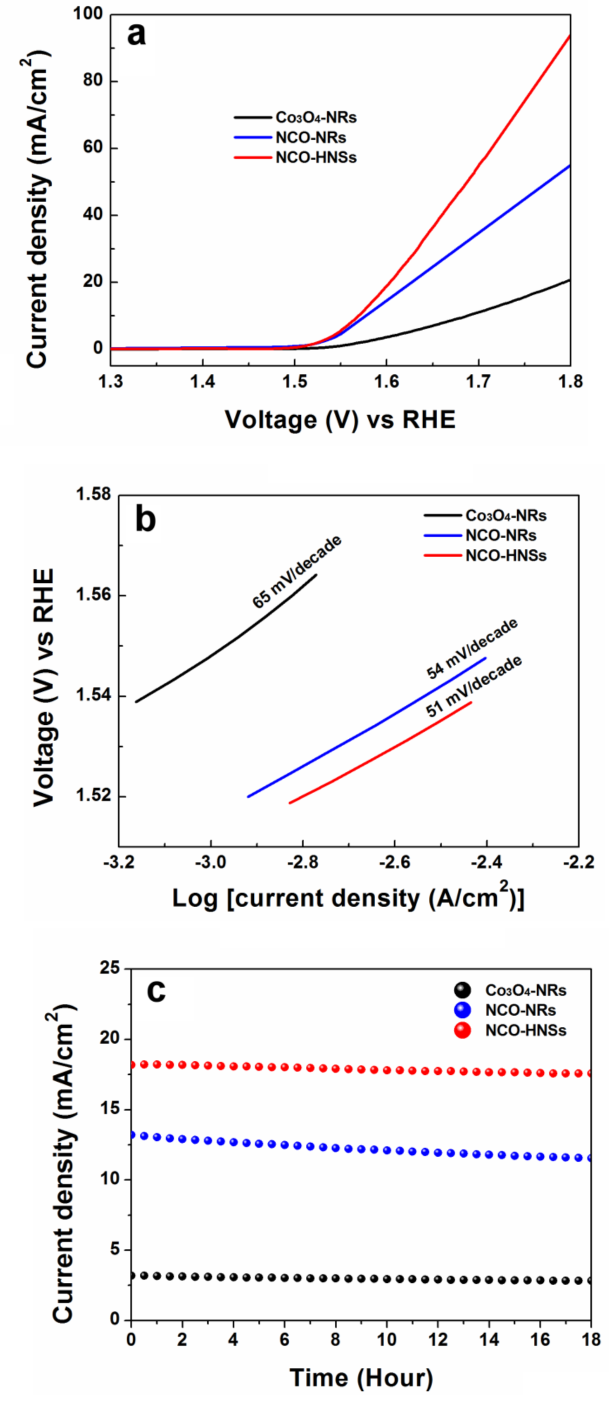

Figure 2-10. (a) Polarization curves recorded at a scan rate of 1 mV/s, (b) corresponding Tafel plots, and (c) chronoamperometric records (current density vs. reaction time) of Co_3O_4-NRs, NCO-NRs, and NCO-HNSs electrodes in 1 M NaOH solution. Reproduced with permission from ref.[80] (© 2015 WILEYVCH Verlag GmbH & Co. KGaA, Weinheim).

Table 2-2. Electrochemical properties of Co_3O_4-NRs, NCO-NRs, and NCO-HNSs electrocatalysts. Reproduced with permission from ref.[80] (© 2015 WILEYVCH Verlag GmbH & Co. KGaA, Weinheim).

	Co_3O_4-NRs	**NCO-NRs**	**NCO-HNSs**
Specific current at a voltage of 1.8 vs. RHE [mA/(cm^2 × R_f × 10^3)]	91.3	134.9	141.2
Tafel slope [mV/dec]	64	55	51
Overpotential at a current density of 10 mA/cm^2	0.45	0.35	0.34
Current density [mA/cm^2] at applied voltage of 1.8 V vs. RHE	20.1	53.7	93.2
Series resistance [Rs, ohm]	29.3	19.7	18.1

2.5 Disclosing the role of Ni in NCO-HNSs toward electrochemical water oxidation via in-stiu X-ray absorption spectroscopy

In-stiu X-ray absorption spectroscopy is a powerful tool to determine the crystallographic structure. **Figure 2-11** shows the typical atomic geometry of spinel Co_3O_4 structure. If the metal ion of interest sits at the octahedral site, there should exist two types of distances for this metal ion connecting the other neighboring metal ions: $Atom_{(Oh)}$-$Atom_{(Oh)}$ (yellow arrow), and $Atom_{(Oh)}$-$Atom_{(Td)}$ (purple arrow). While, if the metal ion of interest sits at the tetrahedral site, the distance from this metal ion to its neighboring metal ion is $Atom_{(Td)}$-$Atom_{(Oh)}$ which is accidently equal the distance of $Atom_{(Td)}$-$Atom_{(Td)}$. In brief, if we observe two different atom-atom distances in the EXAFS spectra, the metal ion of interest should be located at the octahedral site. On the contrary, if there is only one atom-atom distance, the metal ion of interest should be at the tetrahedral site.

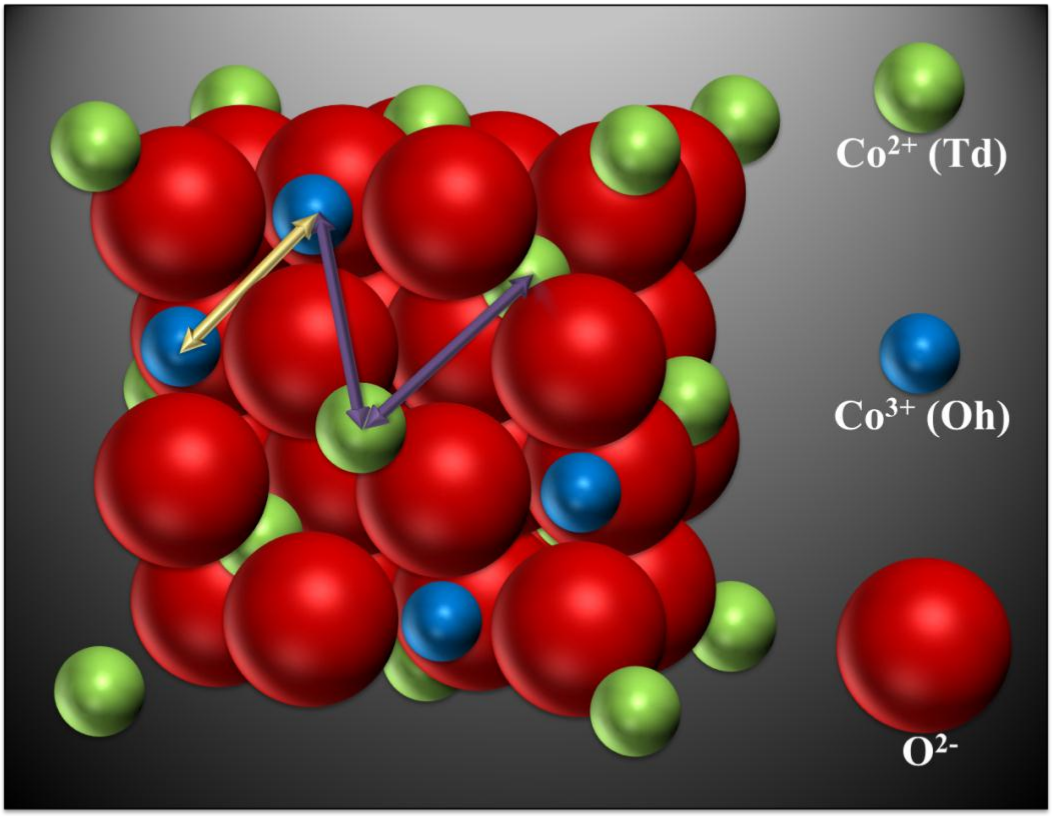

Figure 2-11. The relation of interatomic distance between $\text{atom}_{(Oh)}$ and $\text{atom}_{(Td)}$ in spinel structure. Reproduced with permission from ref.[90] (Copyright © 2016, American Chemical Society).

To realize the real active site for OER in present Ni-Co hierarchical nanostructures, the oxidation states of the NCO-HNSs were monitored using *in-situ* X-ray absorption near edge structure (XANES) during oxidation process in alkaline media. The XANES of Ni K-edge spectra of the NCO-HNSs electrode with and without applied bias in 1 M NaOH were plotted in **Figure 2-12a**. The XANES results exhibited a continuous increase in energy of absorption edge from 8350.2 eV to 8350.7 eV during water oxidation which was consistent with the general overall electrochemical scenario for the formation of NiOOH,[91] resulting in a modification of the edge features related to the variation of Ni-O local environment. The edge position shift (~0.5 eV) was accompanied by a considerable decrease in the intensity of the white line. The continuous decrease in the white line intensity of the XANES spectra evidenced the crystal evolved into a distorted octahedral structure upon oxidation.[92] *In-situ* Co K-edge (~7729.3 eV) XANES spectra of NCO-HNSs were shown in **Figure 2-12b**. Surprisingly, the XANES spectra revealed that the features of Co-K edge absorption spectra and the intensity of white line were not obviously affected by the applied potential from 0.6 V to 2.0 V vs RHE, indicating Co remained as the mixture of Co(II)/Co(III) during the oxygen evolution reaction. To further realize the roles of Ni and Co cations during OER, the extended X-ray absorption fine structure (EXAFS) oscillations of NCO-HNSs electrode were analyzed to clarify the local structural variations around Ni site and Co site in NCO-HNSs structure.

As shown in **Figure 2-12c**, the first peak at approximately 1.5 Å and the second peak at ~ 2.5 Å can be attributed to the single scattering paths of the Ni-O and the closest neighboring transition metals around absorbing atoms Ni, respectively. It has to be noted that there was only one FT peak in single scattering path from closest neighboring transition metals, indicating that Ni cations were located in tetrahedral site surrounded by coordinated oxygen. By contrast, as shown in **Figure 2-12d**, three FT peaks were present in EXAFS spectra of Co K-edge for NCO-HNSs electrode. In addition to the first peak at approximately 1.5 Å from single-scattering path of Co-O, the second peak at ~ 2.5 Å and third FT peak at ~ 3.0 Å are resulted from the single-scattering path of closest neighboring transition metals around Co cations. This phenomenon was owing to the presence of scattering transition metal around Co at two distances, suggesting that Co cations were located in octahedral site of coordinated oxygen, since the octahedrally coordinated cations have two different bond distances (interatomic distances) from surrounding transition metal in octahedral site and tetrahedral site (as indicated in **Figure 2-12e**). Once a desired bias was applied in NCO-HNSs electrode, the second FT peak from single-scattering of Ni-Co path became shorter than that of unbiased condition (**Figure 2-12c**; Ni K-edge), which could be attributed to the partial oxidation of Ni cations. Notably, the X-ray absorption spectroscopy is an assembly measurement, in our present study, underlying Ni atoms can also contribute to the experimental spectra even for fluorescence signal. In terms of Co cations, there was no considerable change with and without applied potential, which suggested that Ni cations acted more active roles than Co cations in oxygen evolution reaction. Nevertheless, the role of Co on the surface of NCO-HNSs during water oxidation cannot be totally ruled out since a more active property of Ni cation might result from the local environment generated by coordinated Co cations and oxygen anions. Furthermore, Co oxide can also act as scaffold to provide a conductive matrix for charge-carriers. Consequently, the XAS data revealed the fact that enriched Ni^{3+} on the surface of NCO-HNSs was more active than Co to initiate the formation of NiOOH and was responsible for most of the redox sites acting for OH^- adsorption in alkaline solution,[89,93] which was critical for enhancing oxygen evolution reaction.

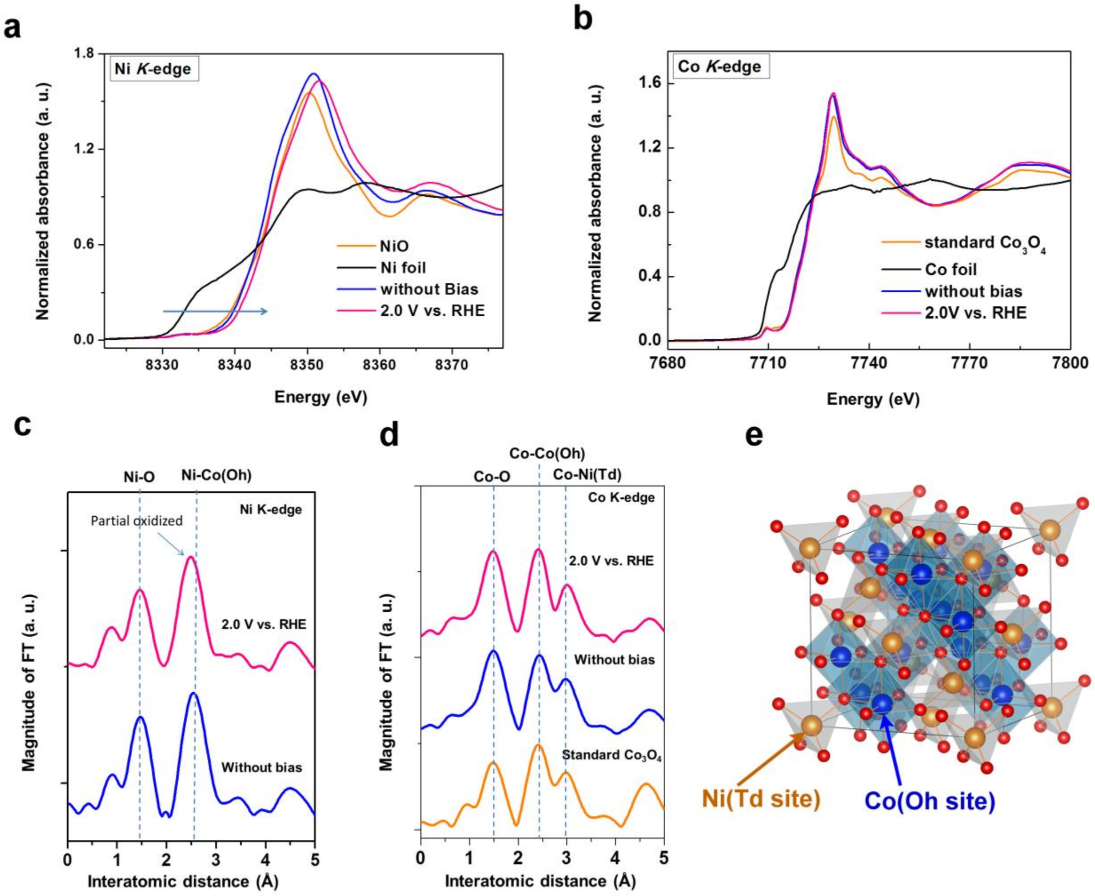

Figure 2-12. Normalized in-situ (a) Ni K-edge and (b) Co K-edge XANES spectra for NCO-HNSs electrode with and without applied bias in 1 M NaOH solution. EXAFS oscillations extracted from in-situ (c) Ni K-edge and (d) Co K-edge EXAFS spectra for NCO-HNSs with and without applied bias in 1 M NaOH solution. (e) The structural geometry model of NCO-NHSs. The interatomic distances are shorter than the real owing to the fact that FT spectra were not phase-corrected. Reproduced with permission from ref.[80] (© 2015 WILEYVCH Verlag GmbH & Co. KGaA, Weinheim).

After the long-term stability test, the morphology, crystalline structure, and nickel and cobalt composition of NCO-HNSs (**Figure 2-13a-d**) remained almost identical after electrochemical reaction, demonstrating the high stability of NCO-HNSs as an OER electrocatalyst. The increased peak intensity at ~ 530.6 eV for O 1s (**Figure 2-13e**) after electrolysis could be assigned to OH^- group of the remaining NiOOH or $Ni(OH)_2$ on NCO-HNSs surface after water oxidation reaction.[31]

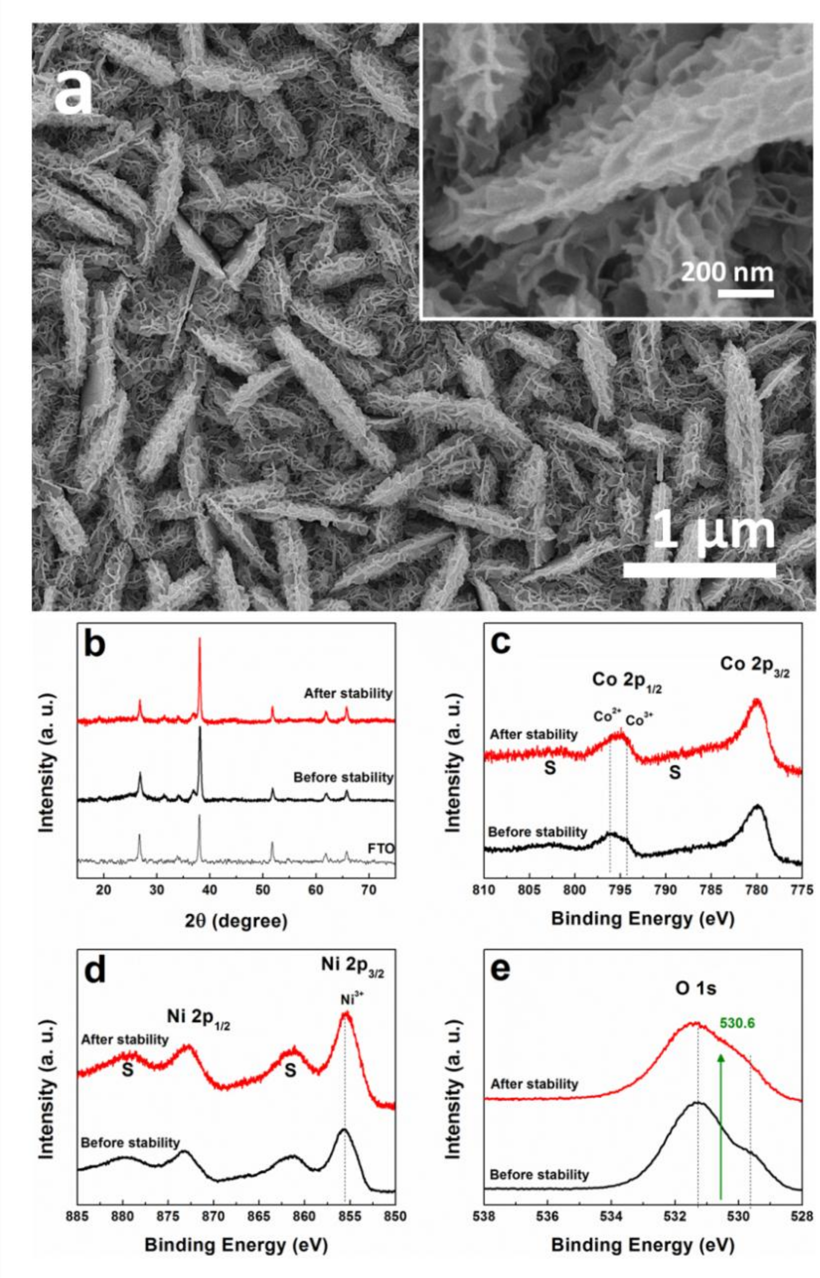

Figure 2-13. (a) FESEM image, (b) XRD pattern, and (c) Co 2p, (d) Ni 2p, and (e) O 1s XPS spectra of NCO-HNSs electrode before and after stability test. Reproduced with permission from ref.[80] (© 2015 WILEYVCH Verlag GmbH & Co. KGaA, Weinheim).

2.6 A brief summary and the remaining issue of NCO-HNSs catalyst

NCO-HNSs composed of secondary nanosheets on primary nanosheet arrays were synthesized via a simple hydrothermal reaction followed by calcination in air. The as-prepared NCO-HNSs not only show large surface area, but also have high content of Ni^{3+} on the surface, which concurrently benefit the oxygen evolution reaction. *In-situ* XANES and EXAFS data of Ni and Co K-edge revealed that Ni cations in NCO-HNSs were located in tetrahedral site surround by coordinated oxygen while Co cations occupied the octahedral site, and Ni was transformed into NiOOH while Co remained in its original valence state with the increase of applied potential. In alkaline medium, the NCO-HNSs exhibited efficient and durable activity for the oxygen evolution reaction, with a low overpotential of 0.34 V to generate a current density of 10 mA/cm^2 and a small Tafel slope of 51 mV/decade. The outstanding electrocatalytic performance of NCO-HNSs can be attributed to the synergy of large surface area offered by the 3D hierarchical nanostructure to facilitate the active site formation and the incorporation of Ni^{3+} as the main active sites on the surface to decrease the overpotential and facilitate the catalytic reaction. A quick literature survey summarized the comparison of OER performance of Ni-Co base electrotalyst is shown in **Table 2-3**.

Table 2-3. Comparison of OER performance of Ni-Co based electrocatalyst. Reproduced with permission from ref.[80] (© 2015 WILEYVCH Verlag GmbH & Co. KGaA, Weinheim).

References	**Electrode & Experimental condition**	**Onset potential [mV]**	**Overpotential at a current density of 10 mA/cm^2 [mV]**	**Tafel slope [mV/dec]**	**Double layer capacitance roughness factor (R_f × 10^3)**	**BET Surface Area (m^2/g)**	**Stability**
Our work	NCO-HNSs on FTO, 1.0 M NaOH	290	340	51	0.68	N.A.	Fixed overpotential at 370 mV for 18 h, 96 % current retention
Ref.[73]	Core-shell $NiCo_2O_4$ nanowire arrays on carbon cloth, 1.0 M NaOH	290	320	63.1	5.2	208	Fixed η in current density range of 10.7 - 23.6 mA/cm^2 for 30 h, 98.8 % current retention

Ref.[94]	$NiCo_2O_4$/Graphene/MnO_2 on Nickel form, 0.1 M KOH	321	N.A.	371.3	N.A.	70	Electrolysis at 6 mA/cm^2 for 12 h, 83.3 % current retention
Ref.[71]	$NiCo_2O_4$/Nitrogen doped grapheme hybrid film, 0.1 M KOH	310	434	156	N.A.	155	Electrolysis at 1.75 mA/cm^2 for 10 h, 90 % current retention
Ref.[95]	$NiCo_2O_4$/Graphene powder coated on glassy carbon disk, 0.1 M KOH	331	471	161	N.A.	77	1000 CV cycles, 99.6 % current retention
Ref.[96]	$NiCo_2O_4$ Nanowire powder coated on glassy carbon disk, 0.1 M KOH	337	412	NA	N.A.	124	Electrolysis at 20 mA/cm^2 for 12.5 h, 95.2 % current retention
Ref.[40]	$Ni_xCO_{1-x}O_4$ nanowire arrays on Ti foil, 1.0 M NaOH	436	N.A.	64	2.8	N.A.	N.A.
Ref.[70]	Teflon-bonded $NiCo_2O_4$ film on Nickel screen, 3.5 M KOH	339	572	44	11.5	14	N.A.
Ref. [97]	Dip-coated Ni-Co LDH on FTO, 0.1 M potassium phosphate	393	N.A.	230-260	1.3	N.A.	N.A.
Ref. [98]	NiFe-LDH/CNT complex on glassy carbon disk, 1 M KOH	220	N.A.	31	N.A.	N.A.	Fixed overpotential at 230 mV for 1000s, stable

It has been revealed that NCO-NHSs catalyst is capable to exhibit an enhanced OER performance mainly due to its rich Ni^{3+} surface. Apart from this observation, the structure of NCO-HNSs is rather interesting because it seems like we accidently substitute Ni ion into the tetrahedral site, which is quite different from that of usual inverse spinel structure where Ni ions usually occupy the octahedral site of Ni doped Co_3O_4. As a result, the tetrahedral Ni ion substituted Co_3O_4 is able to perform a better activity toward OER compared to usual Ni-Co oxide catalyst as pointed out in the **Table 2-3**. This phenomenon attracts our attention to think about is it possible that the activity of Co_3O_4 is geometrical-site dependent in turn the Co^{2+}_{oh} and Co^{3+}_{Oh} could play different role for OER? To further understand the underlying properties of spinel Co_3O_4 catalyst, the geometrical-site dependent activity shall be discussed in the next chapter.

Chapter 3. *Operando* identification of geometrical-site-dependent water oxidation activity of spinel Co_3O_4

3.1 Speculation about the activity of spinel Co_3O_4 toward electrochemical water oxidation: Could the activity be geometrical-site-dependent?

As we have mentioned, water electrolysis could provide a promising way to supply and store clean and sustainable energy,[4,99,100] which consists of two core half reactions: the hydrogen evolution reaction (HER) and the oxygen evolution reaction (OER).[22] Among these two reactions, water oxidation is the rate-determining step because of the thermodynamic up-hill reaction that involves four-electron transfer, which usually requires a high overpotential to drive the reaction.[7] Thus, it becomes extremely important to develop efficient OER electrocatalysts. Spinel cobalt oxide (Co_3O_4) is an earth-abundant and efficient OER catalyst with activity close to the state-of-the-art noble metal based catalysts.[67,101,102] Interestingly, it has been disclosed that the catalytic activity of Co_3O_4 is sensitively dependent on the exposed crystal facets, which could influence the adsorption/desorption of reactants/products.[103] Spinel Co_3O_4 comprises two types of geometrical cobalt ions with different oxidation states: one Co^{2+} ion in the tetrahedral site and two Co^{3+} ions in the octahedral site (denoted as $Co^{2+}{}_{Td}$ and $Co^{3+}{}_{Oh}$, respectively. The population of $Co^{2+}{}_{Td}$ and $Co^{3+}{}_{Oh}$ on different exposed facets of Co_3O_4 nanostructures has been demonstrated as the key to influence the catalytic performance, in which, $Co^{3+}{}_{Oh}$ with higher oxidation state was suggested to offer better catalytic activity.[104,105] For example, in heterogeneous catalysis, Co_3O_4 nanorods with predominately exposed $Co^{3+}{}_{Oh}$ species showed superior catalytic activities towards CO[103,106] and ethylene oxidation[107] as compared to other Co_3O_4 nanostructures because of the existence of abundant catalytic $Co^{3+}{}_{Oh}$ sites on the surface. In electrocatalysis, the vigorous electrochemical water oxidation of Co-Pi catalyst was ascribed to the CoO_6 octahedra geometry.[108,109] Meanwhile, the observed high turnover frequency (TOF) of OER on cobalt-based perovskite[110-112] and delithiated $Li_{1-x}CoO_2$[113,114] were attributable to their modified electronic states of d-orbital configuration of Co^{3+}_{Oh} species. Based on which, several previous works have proposed that the electrochemical OER performance of spinel Co_3O_4 is also geometry site dependent,[33,115-117] where Co^{3+}_{Oh} with higher oxidation state should dominate the water oxidation reaction, yet Co^{2+}_{Td} is relatively inactive. However, the chemical environment of Co_3O_4 is contributed by both Co^{2+}_{Td} and Co^{3+}_{Oh} species, and more importantly, such environment is dynamically changeable during electrocatalysis with applied bias. Without conclusive evidence, the OER active sites in Co_3O_4 remain elusive.

To differentiate the catalytic active sites for water oxidation in spinel Co_3O_4, we separately studied the activity of Co^{2+}_{Td} and Co^{3+}_{Oh} for OER based on a simple ion-substitution strategy. Catalytically inactive Zn^{2+} and Al^{3+} with d^{10} electronic configuration were used to replace Co^{2+} and Co^{3+} in their corresponding tetrahedral and octahedral sites, respectively. To disclose the real-time OER activities of substituted cobalt oxides, electrochemical water oxidation was probed *operando* by electrochemical impedance spectroscopy and X-ray absorption spectroscopy. Our results indicate that Co^{2+}_{Td} and Co^{3+}_{Oh} differ from each other in surface-kinetics and electrochemical reactivity towards OER, and more importantly, Co^{2+}_{Td} that is capable to release electron under applied bias is responsible for the formation of peroxide moieties, cobalt oxyhydroxide (Co-OOH), on Co_3O_4 surface, which acts as the main active site for OER.

3.2 Synthesis of Co_3O_4, $ZnCo_2O_4$, and $CoAl_2O_4$ particles and the detail of the experimental methods

The spinel oxides particles were synthesized by sol-gel method. In a typical synthesis, calculated amounts of $Co(NO_3)_2•6H_2O$, $Zn(NO_3)_2•6H_2O$, and $Al(NO_3)_2•9H_2O$ with an appropriate metal ion ratio (Zn/Co = 1/2 for $ZnCo_2O_4$ and Al/Co = 2/1 for $CoAl_2O_4$) were mixed in 9 mL of 1.5 M citric acid solution at room temperature where the total metal ion amount was fixed at 9 mmol. Following, the resulting solution was stirred and heated at 80 ^{o}C for 3 hours in order to obtain the sol, which was later converted into thick gel. The gel was dried at 120 ^oC followed by further calcined at 800 ^oC for 5 hours under the air atmosphere. The crystallographic information of Co_3O_4, $ZnCo_2O_4$, and $CoAl_2O_4$ particles were collected using X-ray diffraction with Cu Kα irradiation (λ = 1.5406 Å). The morphology was studied with field emission scanning electron microscopy (FESEM, JSM-6700F). The compositional information was probed via X-ray photoelectron spectroscopy (XPS, ESCALAB 250) with Al Kα mono chromatid flood and Mg Kα radiation (1253.6 eV) with a double pass cylindrical mirror analyzer. X-ray absorption spectroscopy (XAS) measurements and *operando* XAS of the oxide samples were collected by employing synchrotron radiation light source at 01C1 beam line of the National Synchrotron Radiation Research Center (NSRRC), Taiwan, and the measurements were made at Co K-edge (7709 eV) and Zn K-edge (9659 eV) with the sample held at room temperature. Homemade cell was designed for the *operando* experiments, which were operated in identical conditions as the electrochemical measurements.

The catalyst was dispersed in a mixed solution containing deionized (DI) water, ethanol, and Nafion (5 wt%) (v/v/v 9:1:0.2, catalyst concentration: 10 mg/mL) by sonication for 24 hours to obtain a homogeneous ink. Then 20 μL of catalyst ink was drop-casted on the FTO substrate ($F:SnO_2$, Tec 15, ~10 Ω/□). The electrode was dried at ambient condition and heated at 80 ^oC for 30 min. All electrochemical characterization were investigated on Bio-Logic VMP3 potentiostat in a three-electrode configuration cell using FTO electrode with precisely controlled active area of 0.384 cm^2 as the working electrode, platinum plate (1 × 2 cm^2) as the counter electrode, saturated calomel electrode (SCE) as the reference. The electrolyte was 0.1 M KOH aqueous solution (pH = 12.73). The reference was calibrated versus reversible hydrogen electrode (0.243 V vs. RHE) and all potentials were converted to the RHE scale. Before collecting the electrochemical data, the working electrodes were cycled between 0 and 0.65 V vs. CE at a scan rate of 10 mV/s for several times to achieve a stable performance. The roughness factor (R_f) was estimated from double-layer capacitance using cyclic voltammetry in a small potential range (0.25 to 0.3 V vs. SCE), from which the double layer capacitance was determined from the slope of the capacitive current (I_{cap}) at the midpoint of the scan range (0.275V vs. SCE) versus the scan rate according to $C_{dl} = I_{cap}/(dE/dt)$, where C_{dl} is the double layer capacitance and dE/dt is the scan rate. R_f was calculated through dividing the slope by 40 μF/cm^2 (capacitance of a smooth surface for transition metal oxide n alkaline solution).[118] Electrochemical impedance spectroscopy (EIS) measurements were performed by applying an AC voltage with 10 mV amplitude in the frequency range of 10^5 Hz to 10^{-1} Hz under applied bias ranging from 0 to 0.75 V versus SCE. OER polarization curves were collected at a scan rate of 1.0 mV/s with iR-correction.

3.3 Structural information of substituted Co_3O_4

Substituted cobalt oxides were prepared by a simple sol-gel method (see the Supporting Information). As displayed in **Figure 3-1a,** both zinc substituted Co_3O_4 ($ZnCo_2O_4$) and aluminum substituted Co_3O_4 ($CoAl_2O_4$) maintain the cubic-spinel structure, which is identical to that of pure Co_3O_4. However, the size and morphology were unavoidably influenced due to different ionic size and electronic state of foreign atoms as compared with those of the host cobalt in Co_3O_4 (see **Figure 3-1b-d**). The polyhedron-like Co_3O_4 particles are ~100 nm in diameter (**Figure 3-1b**), while the size of $ZnCo_2O_4$ and $CoAl_2O_4$ particles become larger and smaller, respectively (**Figure 3-1c&d**). The valence states of cobalt in substituted cobalt oxides were revealed using X-ray absorption near edge structure (XANES), where the position of the absorption edge could be used as an indicator. **Figure 3-1e** shows the valence state of cobalt in different Co_3O_4 samples, which follows the order of $ZnCo_2O_4 > Co_3O_4 > CoAl_2O_4$. This trend agrees well with our expectation that Co^{3+} was preserved in $ZnCo_2O_4$, while Co^{2+} was preserved in $CoAl_2O_4$, and an average oxidation state ($Co^{+2.67}$) of cobalt is expected for Co_3O_4. Furthermore, X-ray photoelectron spectroscopy (XPS) spectra (**Figure 3-2**) confirm the exposed metal ions: Co^{3+} on $ZnCo_2O_4$, Co^{2+} on $CoAl_2O_4$, and Co^{2+} & Co^{3+} on Co_3O_4. The structural position of various metals in substituted cobalt oxides was probed by extended X-ray absorption fine structure (EXAFS). As displayed in

Figure 3-1f-i, the first peak at approximately 1.5 Å can be assigned to single scattering paths of the metal ion to the closest neighboring crystal oxygen. The second peak at ~2.5 Å and the third peak at ~3.0 Å are attributable to the scattering paths of the metal ion to its closest neighboring metal ion in octahedral or tetrahedral site, depending on the position where the metal ion initially stays. As discussed in Chapter 2.5 where it as illustrated a clear relationship of the interatomic distance between the two geometrical metal ions. Octahedrally coordinated cations should possess two different atom-atom bond distances (interatomic distance of ~2.5 Å and ~3.0 Å) from surrounding metal ions in octahedral site and tetrahedral site, respectively. On the other hand, the tetrahedrally coordinated cations only have one atom-atom bond distance of ~3.0 Å. Although no Al K-edge spectrum was collected due to the shortage of beamline resource which could fit the Al K-edge energy of ~ 1300 eV, we were still able to deduce the structure of $CoAl_2O_4$ based on the fact that the Co^{2+} ions only stay at the tetrahedral sites, and in order to fit the requirement of spinel structure as revealed in the XRD pattern, Al^{3+} ions must stay at the octahedral sites. Therefore, it is concluded that Co^{2+} in the tetrahedral site has been successfully replaced by Zn^{2+} in $ZnCo_2O_4$, while Co^{3+} in the octahedral site has been successfully replaced by Al^{3+} in $CoAl_2O_4$, and both $ZnCo_2O_4$ and $CoAl_2O_4$ still maintain the normal spinel structure.

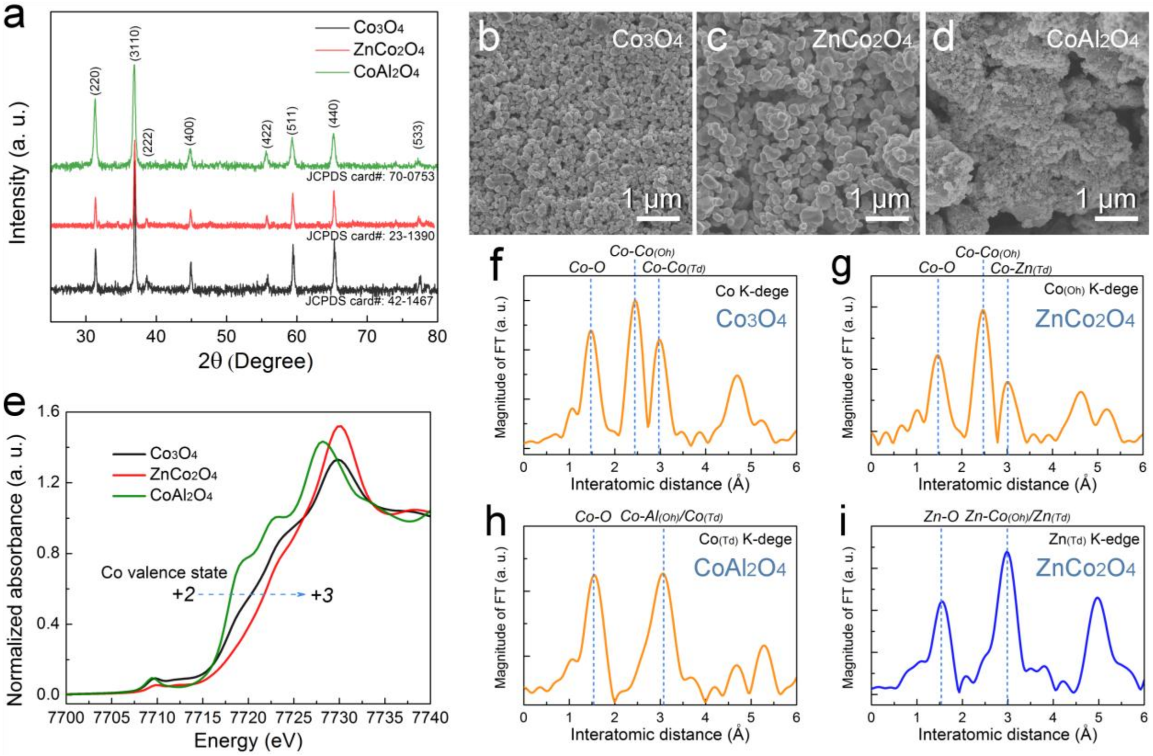

Figure 3-1. Structural information of substituted Co_3O_4. (a) XRD patterns and (b-d) SEM images of Co_3O_4, $ZnCo_2O_4$, and $CoAl_2O_4$. (e) Normalized ex-situ Co K-edge XANES spectra. From which, we could determine the Co valence states to be +2, between +2 and +3, and +3 in $CoAl_2O_4$, Co_3O_4, and $ZnCo_2O_4$, respectively. (f-h) Co K-edge EXAFS spectra for Co_3O_4, $ZnCo_2O_4$, and $CoAl_2O_4$, respectively. (i) Zn K-edge EXAFS spectrum for $ZnCo_2O_4$. For which, the interatomic distances are shorter than the actual values owing to the fact that Fourier transform (FT) spectra were not phase-corrected. Reproduced with permission from ref.[90] (Copyright © 2016, American Chemical Society).

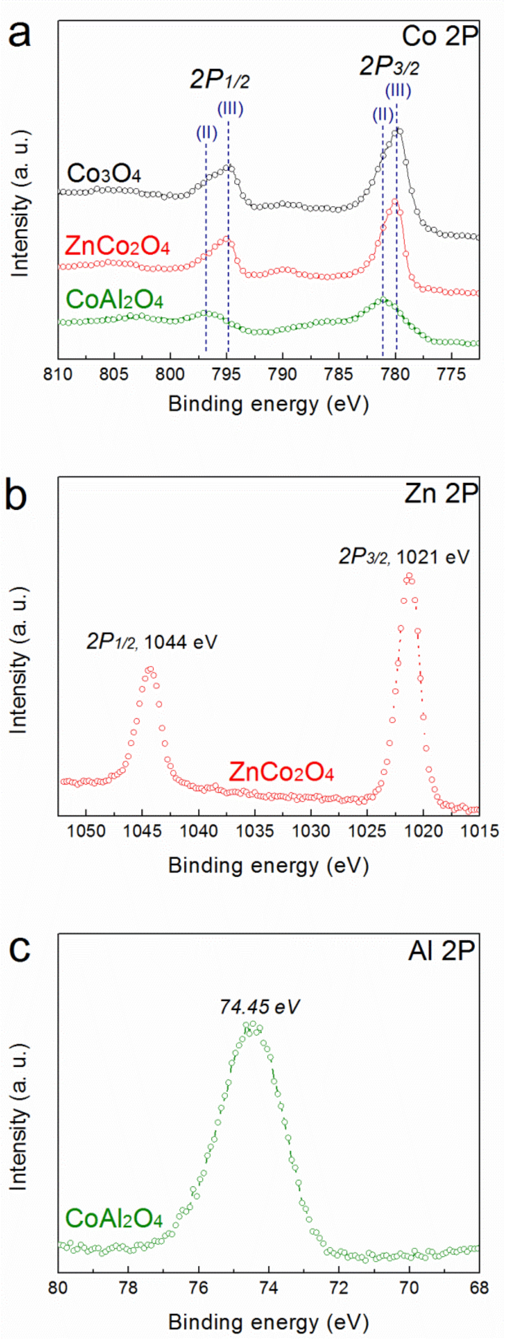

Figure 3-2. XPS spectra of (a) Co 2p for Co_3O_4, $ZnCo_2O_4$, and $CoAl_2O_4$, where Co $2p_{1/2}$ can be de-convoluted into Co^{2+} (796.81 eV) and Co^{3+} (794.85 eV).[80] (b) XPS spectra of Zn 2p for $ZnCo_2O_4$ showing the appearance of characteristic Zn^{2+} (2p) peaks.[119] (c) XPS spectra of Al 2p for $CoAl_2O_4$ showing the appearance of characteristic Al^{3+} (2p) peak.[120] Reproduced with permission from ref.[90] (Copyright © 2016, American Chemical Society).

3.4 Electrochemical performance of the subsituted Co_3O_4

The OER activities of pristine and substituted cobalt oxides were evaluated by cyclic voltammetry (CV) and linear scanning voltammetry (LSV) with corresponding Tofel plots (**Figure 3-3**). The OER activities were nomalized to the electrocatalytic active surface area (ECSA) as determined by double layer capacitance method (**Figure 3-4**).

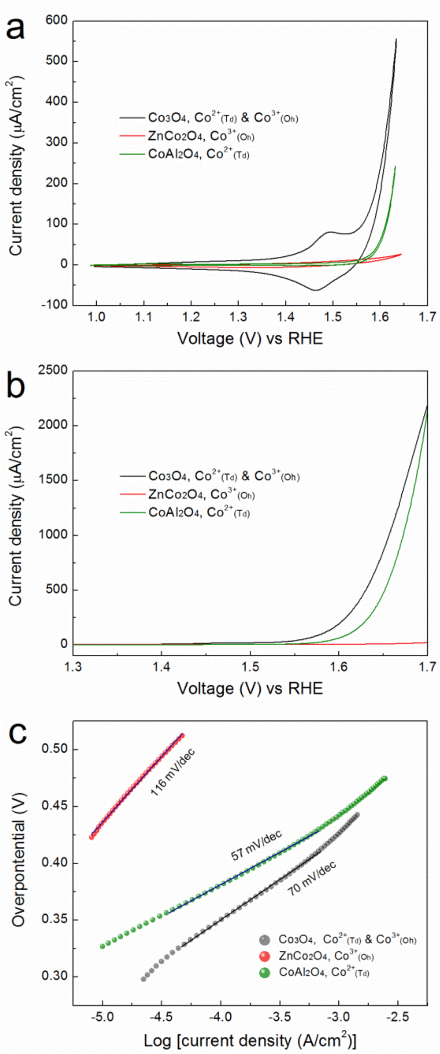

Figure 3-3. (a) Cycling voltammetry curves at a scan rate of 10 mV/s, (b) polarization curves recorded at a scan rate of 1 mV/s, and (c) corresponding Tafel plots of Co_3O_4, $ZnCo_2O_4$, and $CoAl_2O_4$, respectively. Reproduced with permission from ref.[90] (Copyright © 2016, American Chemical Society).

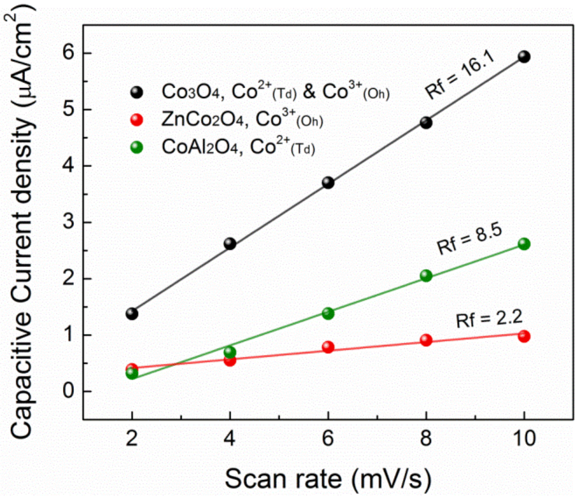

Figure 3-4. Dependence relation of the capacitive current vs. scan rate for Co_3O_4, $ZnCo_2O_4$, and $CoAl_2O_4$. Reproduced with permission from ref.[90] (Copyright © 2016, American Chemical Society).

As shown in the normalized CV curves (**Figure 3-5a**), a pair of redox peaks for Co_3O_4 at 1.49 V (anodic) and 1.47 V (cathodic) vs. RHE is observable, which can be assigned to the redox couple of Co(III)/Co(IV),[37] but such characteristic feature vanishes for $ZnCo_2O_4$, in which there only observes a typical capacitive current. It was proposed that the redox process could only be related to the Co^{2+} tetrahedral sites in Co_3O_4.[116] CV curve of $CoAl_2O_4$ exhibits an almost non-capacitance feature in the voltage range between 1.0 and 1.55 V vs. RHE. However, a small pair of redox peaks can still be identified at 1.13 V (anodic) and 1.10 V (cathodic) vs. RHE (**Figure 3-5a, insert**), which can be attributed to the redox couple of some hydrated cobalt oxides impurities (Co^{2+}/Co^{3+} redox pair).[39,121] A sharp rising in OER current after 1.55 V vs. RHE indicates that a high overpotential is needed to trigger the reaction of water oxidation for Co^{2+}_{Td} predominated $CoAl_2O_4$. It is interesting to find the absence of redox peak at around 1.45 V vs. RHE for $CoAl_2O_4$, which is usually assigned to Co(III)/Co(IV) couple as that in Co_3O_4. For which, the oxidation of Co(III) at tetrahedral site is suggested to be postponed and appear together with OER current rising due to the influence of Al substituent. A series of variation of OER current behaving as a function of Zn and Al substituting amount are shown in **Figure 3-6**. Tafel plots (**Figure 3-6b**) obtained from the normalized polarization curves (**Figure 3-7**) reveal surface kinetic properties of OER. The general OER mechanism in alkaline solution on the metal site (M) begins with a proton-coupled electron transfer from a surface-bound aquo species followed by an O-O bond formation,[19,20] which has been described as eqn.11-14 in Chapter 1.2:

$$\text{M-OH}_2 + \text{OH}^- \rightarrow \text{M-OH} + \text{H}_2\text{O} + e^-$$

$$\text{M-OH} + \text{OH}^- \rightarrow \text{M-O}^* + \text{H}_2\text{O} + e^-$$

$$\text{M-O}^* + \text{OH}^- \rightarrow \text{M-OOH} + e^-$$

$$\text{M-OOH} + \text{OH}^- \rightarrow \text{M-OH}_2 + \text{O}_2 + e^-$$

Among different samples tested, $ZnCo_2O_4$ shows a Tafel slope of 113 mV/dec, indicating that the OER process in $ZnCo_2O_4$ is rate-limited at the first stage where the surface of catalyst is strongly bonded with –OH groups (reaction order = 1 with respect to OH^- species with featured Tafel slope of 120 mV/dec).[18] The Tafel slope for $CoAl_2O_4$ (~56 mV/dec) and Co_3O_4 (~69 mV/dec) are much smaller than that for $ZnCo_2O_4$ and close to a featured Tafel slope of 60 mV/dec, suggesting a different rate-determining step. The OER reactions of $CoAl_2O_4$ and Co_3O_4 are controlled by the equilibrium state between the –OH adsorption and O-O formation in an intermediate coverage regime of –OH groups on the active sites.[18]

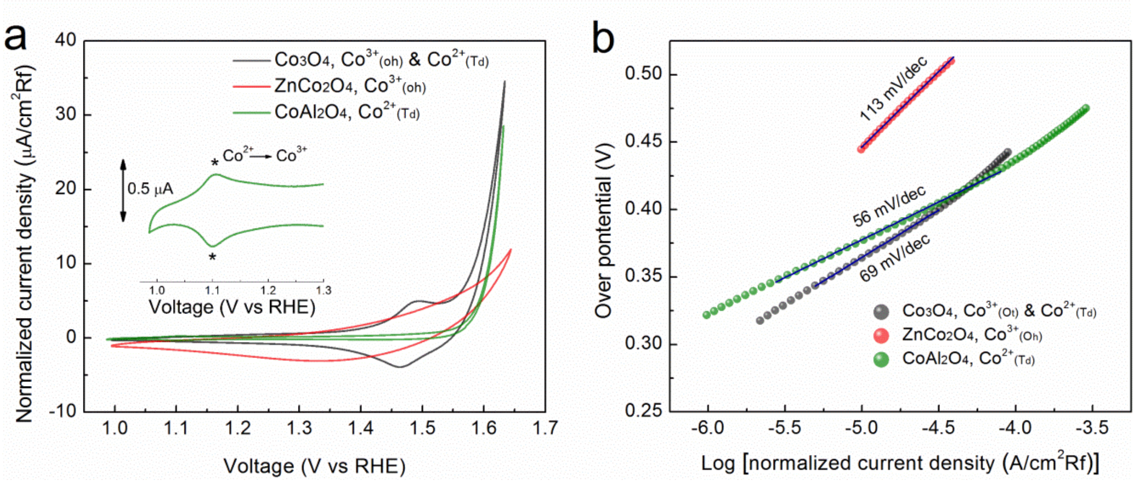

Figure 3-5. Electrochemical performance toward oxygen evolution reaction. (a) Normalized cycling voltammetry curves and (b) corresponding Tafel slopes for Co_3O_4, $ZnCo_2O_4$, and $CoAl_2O_4$. Reproduced with permission from ref.[90] (Copyright © 2016, American Chemical Society).

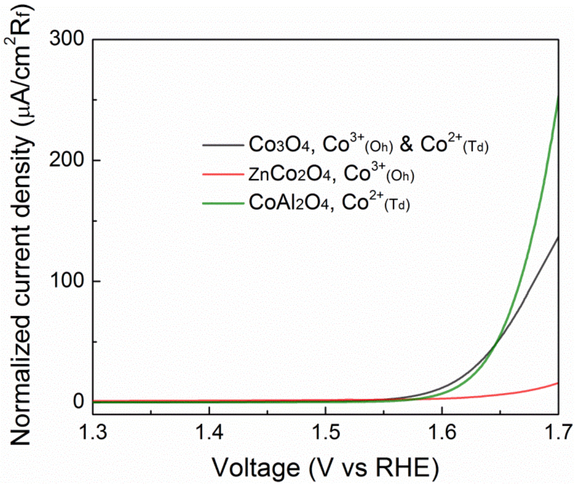

Figure 3-6. Normalized polarization curves recorded at a scan rate of 1 mV/s for Co_3O_4, $ZnCo_2O_4$, and $CoAl_2O_4$, respectively. Reproduced with permission from ref.[90] (Copyright © 2016, American Chemical Society).

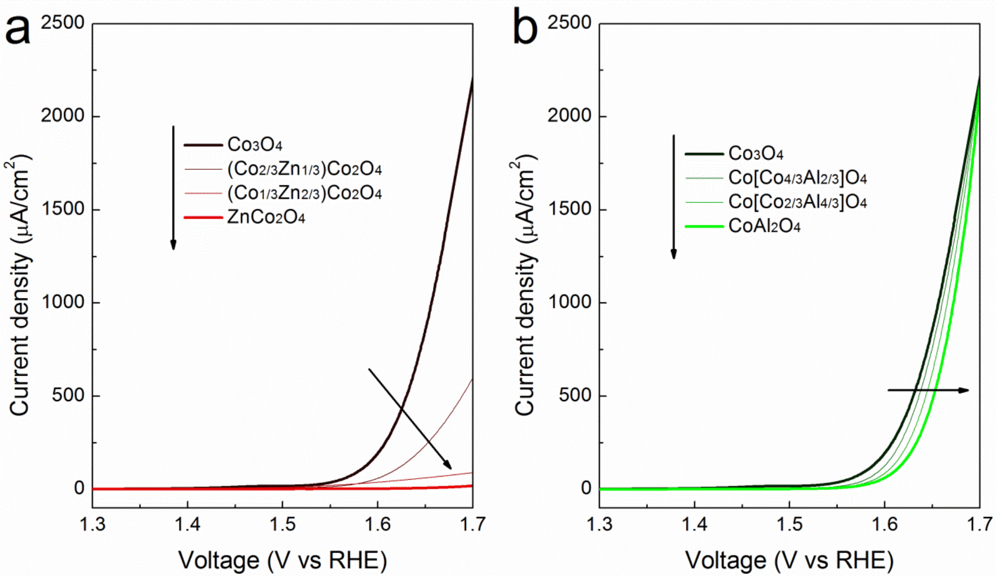

Figure 3-7. OER current behaving as a function of Zn and Al substituting amount. (a) OER current of Zn substituted Co oxide, which shows the performance is gradually reduced with Zn ratio increasing. (b) OER current of Al substituted Co oxide, which shows the performance is unchanged but the onset is gradually postponed with Al ratio increasing. Reproduced with permission from ref.[90] (Copyright © 2016, American Chemical Society).

3.5 *Operando* electrochemical impedance spectroscopy

To gain in-depth information of underlying controlling factors for water oxidation, *operando* electrochemical impedance spectroscopy (EIS) measurements were carried out. The current response was measured over a frequency range of 10^5 - 10^{-1} Hz under AC perturbation voltage with a small amplitude (10 mV) superimposed on an applied DC bias. **Figure 3-8a-b** show the phase angle relaxation as a function of frequency in terms of various electrochemical reactions (Bode phase plot). A brief illustration of the relation between the phase angle and the electrochemical reactions are shown in the following Figure:

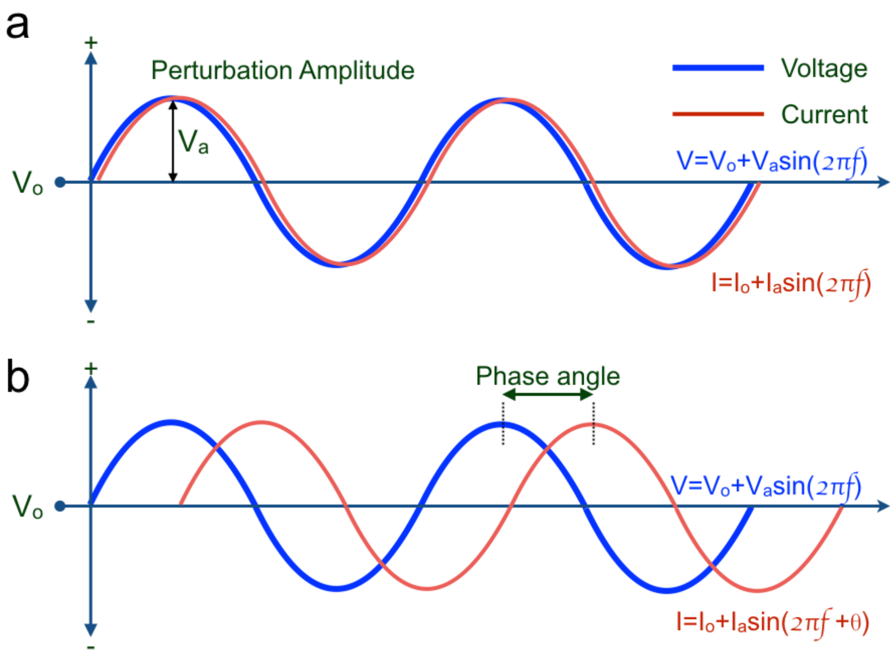

Figure 3-8. Illustration of the generation of phase angle under (a) no specific reaction and (b) a specific reaction on the electrode surface.

Once a perturbation bias with a sine wave is introduced into a steady system, a corresponding vibrating current will be almost simultaneously induced (**Figure 3-8a**). However, if there is a particular electrochemical reaction, e.g., capacitance effect exciting on the electrode surface, the induced current may be stored for a while and then released out. As a result, we will see a time-delay in terms of phase angle (θ) between the voltage and current response (**Figure 3-8b**).

As displayed in **Figure 3-9a**, two phase peaks in Co_3O_4 (one at middle frequency and the other at low frequency) gradually move towards each other with increase in applied external bias. The corresponding Nyquist plot (**Figure 3-9d**) shows two semi-circles at high applied potential (0.7 V vs. SCE). While only one phase peak was observed in $ZnCo_2O_4$ at the middle frequency region if Co^{2+} in the tetrahedral site of Co_3O_4 was replaced by Zn^{2+} (**Figure 3-9b**), and the corresponding Nyquist plot (**Figure 3-9e**) only displays one large semi-circle in the entire bias range of testing. Interestingly, if Co^{3+} in the octahedral site of Co_3O_4 was replaced by Al^{3+}, only one phase peak could be identified at the low frequency region in the Bode phase plot, which moved towards lower frequency with increase in applied bias, opposite as compared to Co_3O_4 and $ZnCo_2O_4$. The corresponding Nyquist plot shows steep straight lines nearly perpendicular to x-axis (**Figure 3-9f**) in the potential range of 0 - 0.55 V vs. SCE, indicating infinite charge transfer resistance. This observation is consistent with the result obtained in the CV measurement, in which almost no capacitive feature could be identified due to weak electronic interaction. When applied bias was higher than 0.55 V vs. SCE, a corresponding semi-circle appeared in its Nyquist plot. **Figure 3-9g** merges the relaxation curves selected from Co_3O_4 (0.6 V vs. SCE), $ZnCo_2O_4$ (0.75 V vs. SCE), and $CoAl_2O_4$ (0.6 V vs. SCE). The relaxation curves were selected at different applied potentials based on comparable OER current densities (**Figure 3-5b**). As shown in **Figure 3-9g**, two electrochemical processes at two different frequency regions can be clearly identified: the middle frequency region (10^2 - 10^3 Hz) is associated with surface double layer capacitance (DLC),[122,123] and the low frequency region (10^0-10^1 Hz) could be related to the non-homogeneous charge distribution caused by surface oxidized species (e.g., Co^{3+}→Co^{4+}[123-125] or the oxidation of the surface intermediates) Thus, based on the EIS results, it is reasonable to deduce that Co^{3+}_{Oh} in Co_3O_4 is responsible for surface DLC, while Co^{2+}_{Td} is responsible for water oxidation. Our conclusion coincides well with the observation in CV and Tafel plots, in which $ZnCo_2O_4$ exhibits pure capacitive behavior with strong –OH affinity, while $CoAl_2O_4$ shows week electronic interaction followed by rising in OER current. Meanwhile, the synergistic effect of Co^{2+}_{Td} and Co^{3+}_{Oh} in Co_3O_4 needs to be emphasized. The –OH accumulation induced DLC should benefit the overall catalytic driving force, which could be seen from the CV curve as shown in **Figure 3-5a**. As compared with Co_3O_4, the OER onset is postponed and the potential of redox couple of Co(III)/Co(IV) is shifted after OER current for $CoAl_2O_4$. On the other hand, the kinetics of Co^{2+}_{Td} could also be masked by DLC[123] as a larger Tafel slope (69 mV/dec) was observed in Co_3O_4 as compared to that of $CoAl_2O_4$ (56 mV/dec).

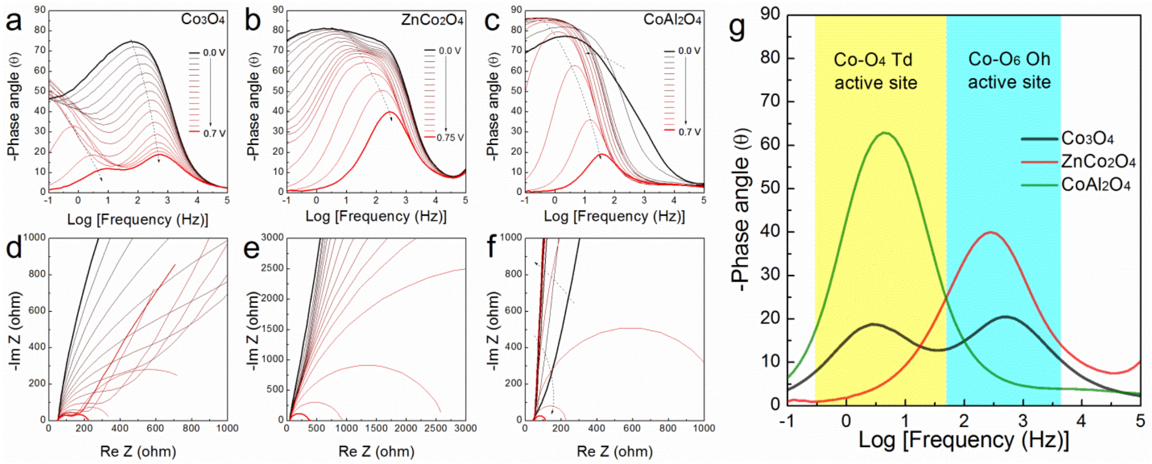

Figure 3-9. *Operando* electrochemical impedance spectroscopy. (a-c) Phase angle vs. log(frequency) plots of EIS data recorded at various voltages and (d-f) the corresponding Nyquist Plots for Co_3O_4, $ZnCo_2O_4$, and $CoAl_2O_4$, respectively. In which, the applied voltage is referenced to SCE. (g) Phase angle vs. log(frequency) plots from Co_3O_4, $ZnCo_2O_4$, and $CoAl_2O_4$ based on similar OER current densities. Reproduced with permission from ref.[90] (Copyright © 2016, American Chemical Society).

3.6 *Operando* X-ray absorption spectroscopy

Operando EXAFS was performed to probe the variation of chemical environment on the catalyst during OER using a home-made *operando* cell (**Figure 3-10**).[126]

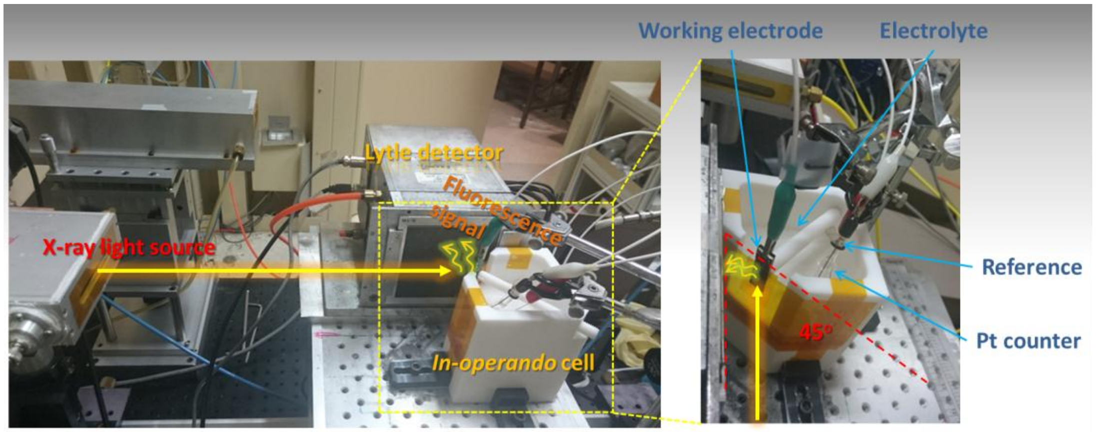

Figure 3-10. The detail of the *operando* X-ray absorption spectroscopy measurement. The device is set-up at 01C1 beam line with the support form National Synchrotron Radiation Research Center (NSRRC), where the X-ray induced fluorescence model is applied. Reproduced with permission from ref.[90] (Copyright © 2016, American Chemical Society).

Figure 3-11a-c display the Co K-edge spectra, which show that the corresponding interatomic distances of Co^{3+}_{Oh} and Co^{2+}_{Td} to their neighboring atoms in all catalysts remain nearly constant at the voltage range between 1.2 and 1.8 V vs. RHE, indicating a highly stable bulk structure of spinel.[127] However, slightly compressed Co-O bond could still be observed in Co_3O_4 during OER (**Figure 3-11d**), indicating partial oxidation of the catalyst surface. Interestingly, the shrinking in length of Co-O bond with applied bias could only be observed on Co^{2+}_{Td} predominated $CoAl_2O_4$, but not on $ZnCo_2O_4$. The corresponding k^3-weighting k-space spectra (**Figure 3-12**) also reveal the variation between 1.0 V and 1.8 V vs. RHE in Co_3O_4 and $CoAl_2O_4$. The Co K-edge EXAFS spectra (**Figure 3-11e**) show that the white line intensity remains constant for $ZnCo_2O_4$, but keeps growing up for $CoAl_2O_4$ with increase in applied positive bias (**Figure 3-11f**), indicating accumulation of positive charges on the cobalt ions on $CoAl_2O_4$, i.e., Co^{2+}_{Td} with initially low oxidation state is able to release electron under applied bias, which can facilitate the interaction with oxygen intermediates on the catalyst surface. This electron-releasing and oxygen-adopting process suggests the formation of Co-OOH moieties (eqn. 3), which acts as the main active sites in the turnover-limiting pathway for water oxidation on Co_3O_4.[18,126] As compared with reported phosphate containg cobalt oxide (or *Co-Pi*), where the octahedral Co center in cubane structure[128,129] is capable to be oxidized to Co(IV) in the OER cycle involving a chemical turnover-limiting process of Co-OOH formation,[108] our work reveals that the Co^{3+}_{Oh} species should be relatively inactive as compared to Co^{2+}_{Td} in Co_3O_4 spinel. Based on the fact of the present result, it is concluded that to form Co-OOH intermediate species, oxidation process on active Co ion is the critical process, and Co^{2+}_{Td} is disclosed as the active species in Co_3O_4, which can be oxidized under applied anodic bias. Thus, the accumulated positive charge within the catalyst can greatly assist the Co-OOH formation (eqn. (3)) on Co_3O_4 surface.

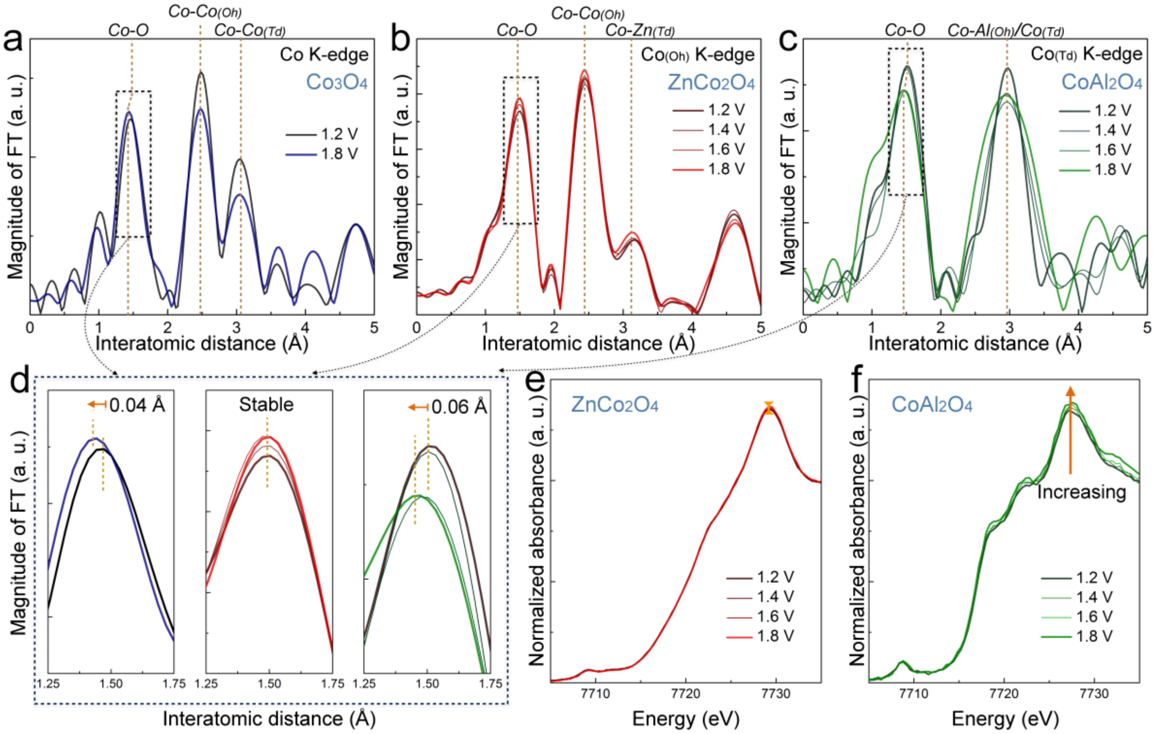

Figure 3-11. *Operando* X-ray absorption spectroscopy. (a-c) Co K-edge EXAFS spectra for Co_3O_4, $ZnCo_2O_4$, and $CoAl_2O_4$. (d) Enlarged Co K-edge EXAFS spectra on Co-O interatomic distance for Co_3O_4 (blue), $ZnCo_2O_4$ (red), and $CoAl_2O_4$ (green). (e & f) Normalized *operando* Co K-edge XANES spectra for $ZnCo_2O_4$ and $CoAl_2O_4$. Reproduced with permission from ref.[90] (Copyright © 2016, American Chemical Society).

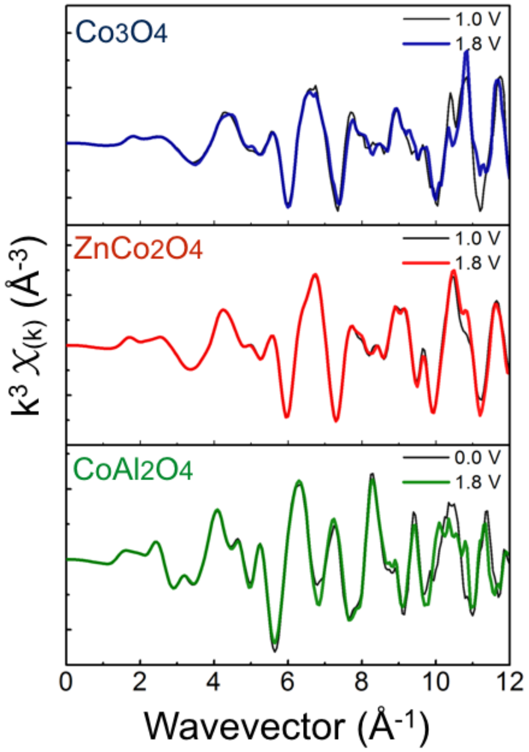

Figure 3-12. k^3-weighting k-space spectra of Co_3O_4, $ZnCo_2O_4$, and $CoAl_2O_4$ at applied bias of 1.0 V and 1.8 V vs, RHE. From which, we can observe the vibration is obviously changed at the range of 8 – 12 wavevector number for Co_3O_4 and $CoAl_2O_4$. Reproduced with permission from ref.[90] (Copyright © 2016, American Chemical Society).

3.7 Conclusion of the study on geometrical-site-dependent activity

In summary, we have successfully identified distinct kinetics and electrochemical reactivity of $Co^{2+}{}_{Td}$ and $Co^{3+}{}_{Oh}$ towards oxygen evolution reaction in spinel Co_3O_4. Our study showed that $Co^{2+}{}_{Td}$ in Co_3O_4 is capable to release electrons under applied bias, promoting the affinity to oxygen intermediates on the catalyst surface to form Co-OOH moieties, which acted as the main active site for OER, yet $Co^{3+}{}_{Oh}$ predominated catalyst, $ZnCo_2O_4$, tended to stably bond with –OH groups, limiting its catalytic activity. Our work further emphasizes the importance of *operando* investigations on electrocatalysis for instantaneously probing the real-time electrochemical kinetics and surface reactions.

Although geometrical-site-dependent activity of spinel Co_3O_4 has been successfully disclosed by a facile substitution method, during the experiment, the changeable feature of the anodic peak prior to the onset of OER current gives rise to our attention. This anodic peak has been usually ascribed to the bulk redox reaction along with a phase transformation from spinel Co_3O_4 to a layered Cobalt oxhydroxide (CoOOH). We want to emphasize here that the layered CoOOH structure is different from the surface moieties, Co-OOH, which is the intermediate species during the water oxidation as we mentioned in this chapter. As discussed in Chapter 1.4, this structural transformation has been generally accepted because of the Co-H_2O Purbaix diagram calculated based on the thermodynamics. However, recently, the work[130] by Prof. Peter Strasser has employed an in-situ XRD technique to reveal that such phase evolution was actually hard to be observed before the rise of OER current. Instead, only a sub-nanometer hydrated cobalt oxide, $Co_x(OH)_y$ could form on the surface once the applied bias is higher than the onset. Besides, in this chapter, our *operando* XAS result also indicated no obvious increase of the oxidation state of Co ions and variation of cobalt atom-atom distance could be detected before the onset. Thus, if it is true that there is no such "phase transformation" taking place prior to the onset, then what are the underlying properties of that anodic peak before the rise of OER current? To go a step further to understand the real scenario happing on the spinel Co_3O_4 during the whole OER process, we use a series of *in-situ* techniques to real-time study the surface reaction as exhibited in the next chapter.

Chapter 4. *In-Situ* Spectroscopic Identification of μ-OO bridging on Co_3O_4 Water Oxidation electrocatalysts before Onset

4.1 What is the underlying reaction as indicated by the anodic peak before the rise of OER current?

Earth-abundant Spinel Co_3O_4, composed of one Co^{2+} ion in the tetrahedral site ($Co^{2+}{}_{Td}$) and two Co^{3+} ions in the octahedral site ($Co^{3+}{}_{Oh}$), has been extensively studied as an effective electrocatalyst for water oxidation[67,101,102] because of its capability to boost the bottleneck oxygen evolution reaction (OER) in water electrolysis, which involves a stepwise four-electron transfer.[7] Meanwhile, the oxygen reduction reaction (ORR) of Co_3O_4 has also been evaluated, enabling it to work as a bifunctional air cathode for metal-air batteries.[67,131] It has been generally accepted that the spinel structure of Co_3O_4 will be transformed to layered hydroxide/oxyhydroxide ($Co(OH)_2$/COOH) structure by means of oxidation of cobalt ions to higher valence states as indicated by the anodic peak prior to the onset of OER current[26,35-38] as indicated in **Figure 4-1**:

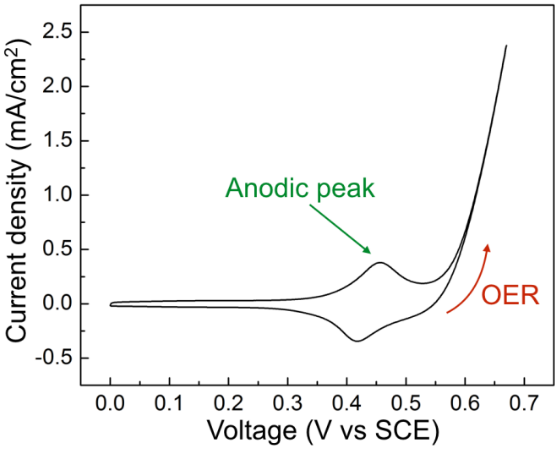

Figure 4-1. A typical cycling voltammetry curve of Co_3O_4 in 1 M KOH, where saturated calomel electrode (SCE) was used as reference. From which, an obvious anodic peak prior to the OER onset can been easily identified (This figure is the duplicate of Figure 1-10 from Chapter 1.4).

This phase transformation step is crucial because the newly formed oxyhydroxide is considered as the active species for water oxidation.[33] It has evidenced by *in-situ* X-ray photoelectron spectroscopy (XPS) measurement that the electrochemical deposited cobalt oxide without calcination could be transformed from spinel Co_3O_4 to layered CoOOH structure under positive bias.[35] If the above conclusion is true, principally, we should be able to observe clear evidence for the hydroxide/oxyhydroxide formation. However, as indicated in Chapter 3,[90] the *in-situ* X-ray absorption (XAS) measurement revealed almost no variation of valence states for cobalt ions in Co_3O_4 during water oxidation. Meanwhile, in the work performed by Prof. Strasser et. al.,[130] their CV result clearly indicated an obvious pair of redox peaks before the OER onset. However, in the *in-situ* XRD results, we could not find any new phase formation before the onset voltage of 1.62 V vs. RHE. Meanwhile, the corresponding atom-atom distance also remained constant. Thus, if there was indeed a new phase formation as indicated by the anodic peak prior to the OER onset, we should see the changes in the *in-situ* XRD and XAS spectroscopy data. On the contrary, once the applied voltage was higher than 1.62 V vs. RHE, some slight variation could be identified by data fitting. Thus, they concluded that a "sub-nanometer" reversible new phase could be formed only when the applied bias was higher than the onset voltage. Besides, they also did not assign the newly formed phase as cobalt oxyhydroxide (CoOOH), but an amorphous hydrated cobalt oxide, $CoO_x(OH)_y$ by doing data fitting. More interestingly, as revealed Chapter 3, the anodic peak was originally ascribed to the oxidation of cobalt in the cycling voltammetry (CV) scan could be completely vanished if the tetrahedral Co^{2+} ions in Co_3O_4 were substituted by Zn^{2+} ions.[90,116] This phenomenon attracts our attention to understanding the underlying chemical and physical properties of this anodic peak prior to the rise in the OER current.

To instantaneously probe the variation of the chemical environments on Co_3O_4 electrocatalyst under operando conditions, we redesigned several in-situ cells for a series of in-situ techniques including X-ray absorption spectroscopy, X-ray diffraction spectroscopy, and Raman measurement. With the conjoint observations from these measurements, we should be able to realize the truthful scenario of the integrated surface reaction on Co_3O_4 during the electrochemical water oxidation process

4.2 Catalyst Preparation, physical characterization, electrochemical measurements, and the detail of the *in-situ* measurements.

All chemicals were of analytical grade, purchased from Sigma-Aldrich and used without any further purification. The spinel cobalt oxide (Co_3O_4) and Zn or Al substituted Co_3O_4 particles (denoted as $ZnCo_2O_4$ and $CoAl_2O_4$, respectively) were synthesized by a sol-gel method as reported in our previous Chapter.[90] In brief, $Co(NO_3)_2{\cdot}6H_2O$, $Zn(NO_3)_2{\cdot}6H_2O$, and $Al(NO_3)_2{\cdot}9H_2O$ with an appropriate metal ion ratio (Zn/Co = 1/2 for $ZnCo_2O_4$ and Al/Co = 2/1 for $CoAl_2O_4$, where the overall metal ion amount was fixed at 9 mmol) were added into 9 mL of 1.5 M citric acid solution. The mixture was stirred at 80 ^{o}C for 3 h to obtain the sol, which was later converted into a thick gel. The gel was dried at 120 ^{o}C followed by calcined at 800 ^{o}C for 5 h under ambient atmosphere. In the pH-dependent and scan rate-dependent cycling voltammetry studies, Co_3O_4 and nickel oxide (NiO_x) were directly grown on FTO substrate ($F:SnO_2$, Tec 15,

~10 Ω/□) to facilitate the preparation of electrodes. In a typical synthesis, calculated amount of $Co(NO_3)_2 \cdot 6H_2O$ or $Ni(NO_3)_2 \cdot 6H_2O$ was added into 30 mL of deionized water with a fixed metal ion concentration of 0.02 M. Afterwards, 6 mmol of NH_4F and 10 mmol of urea were introduced into the mixture under vigorous stirring for 15 min. The homogeneous solution was transferred into a Teflon-lined stainless steel autoclave. Two pieces of FTO substrate, which were ultrasonically cleaned for 30 min in a mixed solution of deionized water, acetone, and 2-propanol with volume ratios of 1 : 1 : 1, were placed at an angle against the wall of the Teflon-liner with the conducting side facing down. The hydrothermal reaction was carried out at 120 °C for 3 h in a temperature-controlled oven. After synthesis, the autoclave was cooled to room temperature under flowing air for 2 h. The FTO substrate was rinsed with deionized water and dried in ambient air, followed by calcined at 450 °C for 2 h in atmosphere. Morphologies of the as-synthesized FTO electrodes are shown in **Figure 4-2**.

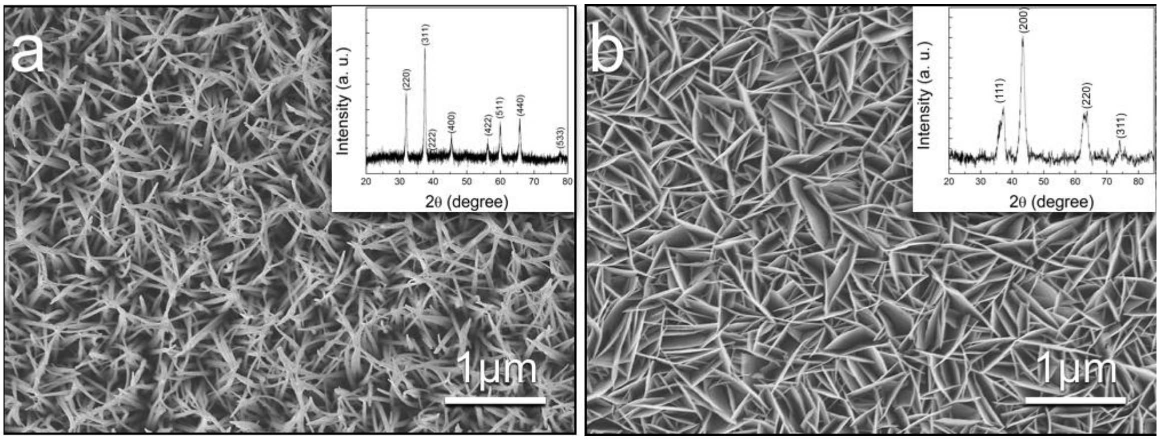

Figure 4-2. Morphological and crystallographic information of hydrothermally prepared (a) Co_3O_4 and (NiO_x) electrodes. In which, spinal Co_3O_4 and rock-salt NiO_x match well with the JCPDS #42-1467 and JCPDS #47-1049 data-base cards, respectively.

The materials properties and confirmation of normal spinel structure for Co_3O_4, $ZnCo_2O_4$, and $CoAl_2O_4$ were reported in the Chapter 3,[90] where Co ions in $ZnCo_2O_4$, and $CoAl_2O_4$ solely occupy the octahedral and tetrahedral sites, respectively. To gain the crystallographic information of hydrothermally synthesized Co_3O_4 and NiO_x, the active materials were scraped from the FTO substrates followed by ground for 1 min before collecting the X-ray diffraction (XRD) spectra with in-house Cu Kα irradiation (λ = 1.5406 Å). The morphological information of Co_3O_4 and NiO_x electrodes was examined by field emission scanning electron microscopy (FESEM, JSM-6700F).

In the scan rate-dependent and pH-dependent cycling voltammetry measurements, the hydrothermally synthesized Co_3O_4 and NiO_x electrodes with confined active area 1×1 cm^2 were directly used as the working electrodes. All electrochemical characterization were investigated on the Bio-Logic VMP3 potentiostat in a three-electrode configuration using platinum plate (1×2 cm^2) as the counter electrode, saturated calomel electrode (SCE) as the reference. The electrolyte was prepared using high purity KOH. The concentration of OH^- in solution was adjusted by the amounts of KOH and KCl was used to fix the cation concentration at 2 M in the electrolyte for pH-dependent CV measurement. The reference was calibrated versus standard hydrogen electrode (V^o = 0.241 V vs. SHE) and the recorded potential was converted to the RHE scale using the following equation: $V_{RHE} = V_{SCE} + V^o_{SCE} + 0.059 \times pH$. Before collecting the electrochemical data, the working electrodes were cycled between 0 and 0.65 V vs. SCE at a scan rate of 20 mV/s for several times to achieve a stable performance. For NiO_x electrode, the stabilization process took over 200 cycles to achieve a stable redox couple of Ni(II)/Ni(III). The color of NiO_x film abruptly changed from light brown-green ($Ni(OH)_2$) to deep black (NiOOH) after passing the oxidation peak.

In-situ X-ray absorption spectroscopy (XAS) measurements were conducted by employing synchrotron radiation light source at 01C1 beam line from the National Synchrotron Radiation Research Center (NSRRC), Taiwan. The measurements were made at Co K-edge (7709 eV) at room temperature. X-ray absorption data were analyzed according to the universal standards, including pre-edge and post-edge background subtraction, normalization with respect to edge-jumping height, and Fourier transformation with k^3 weighting yet without phase correction. Before introducing the X-ray light beam, the cell was cycled between 1.4 to 2.3 V vs $Zn/Zn(OH)_4^{2-}$ at 5 mV/s for 10 cycles and conditioned at each desired voltage for 15 min, and the period token in XAS measurement at each voltage point was around 43 min due to a slow scan rate (10 eV / point / 2s for pre-edge range of -200 to -30 eV, 0.35 eV / point / 2s for near edge range of -30 to 40 eV, and 0.06 k / point / 4s for the post-edge range of 40 eV to 1200 eV). The XAS fluorescent mode used here is relatively surface-sensitive than that of penetration mode. *In-situ* grazing-angle XRD measurements were conducted using the 01C2 beam line at NSRRC with a radiation light energy of 12 keV (λ = 1.0332 Å). The XRD patterns were captured at each 7.45 mV interval and it spent 2.5 min to capture one XRD pattern at each voltage point. We adopted the configuration of the metal-air battery cell[132] (**Figure 4-3**), where Co_3O_4 acted as the cathode in an operating metal-air battery, a homemade zinc-air battery cell (made of polymethylmethacrylate, PMMA) was designed for both *in-situ* XAS and XRD experiments as shown in **Figure 4-4 and 4-5**, respectively.

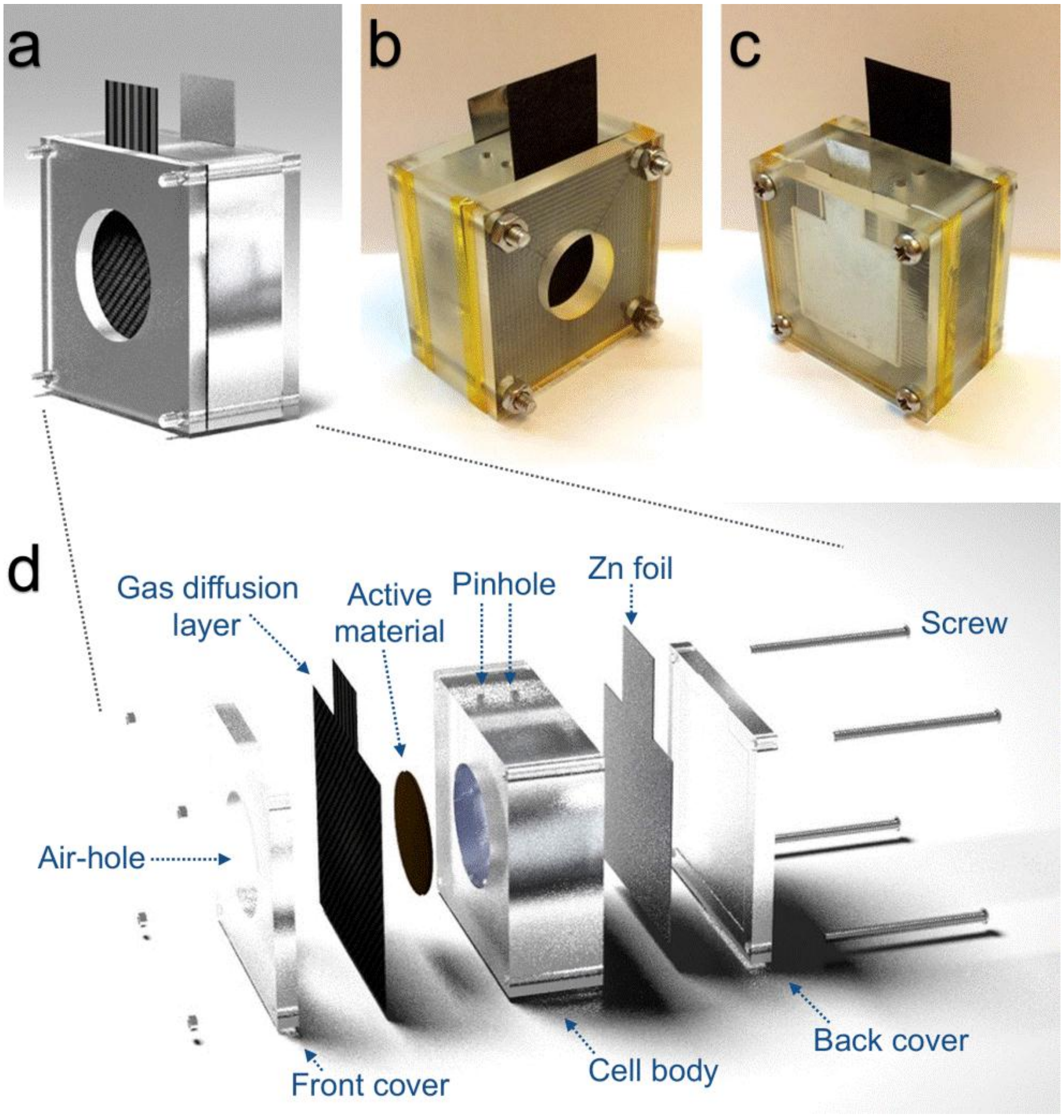

Figure 4-3. Zinc-air battery cell designed for *in-situ* studies. (a) Concept and design of zinc-air battery cell. (b) Digital image of the *in-situ* cell (front view). (c) Digital image of the *in-situ* cell (back view). (d) Details of the components.

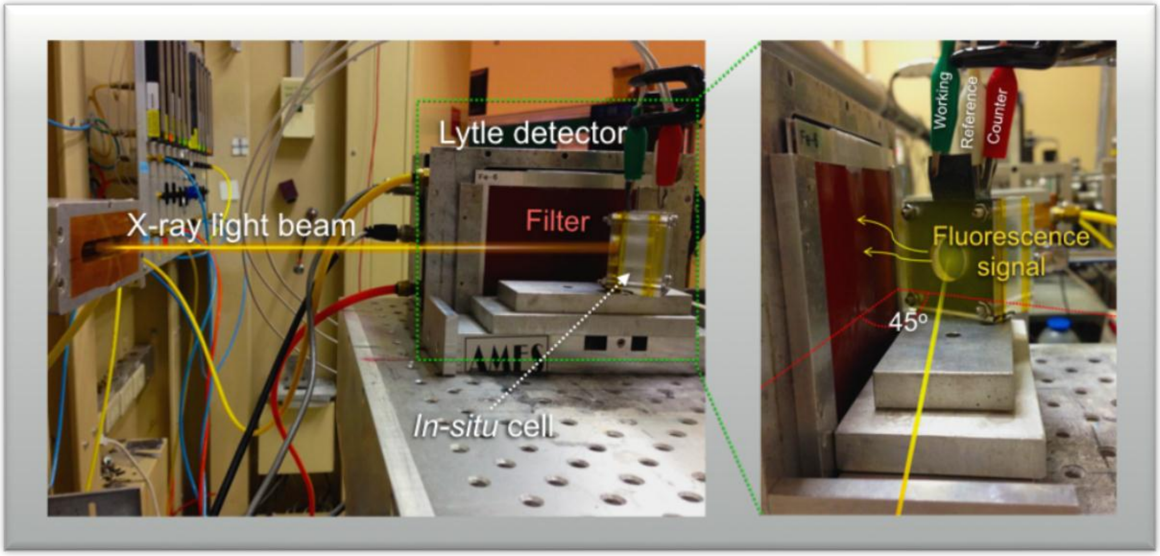

Figure 4-4. Details of the *in-situ* XAS apparatus. The device is set up at 01C1 beam line with the support from National Synchrotron Radiation Research Center (NSRRC), where the X-ray induced fluorescence model is applied.

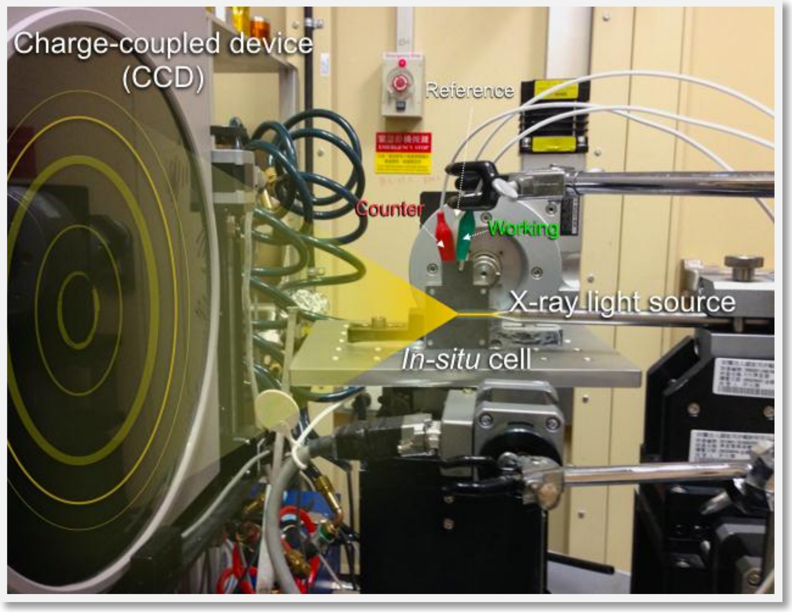

Figure 4-5. Details of the *in-situ* grazing-angle XRD apparatus. The device is set up at 01C2 beam line with the support from National Synchrotron Radiation Research Center (NSRRC). Note: the front cover of the cell was removed.

To prepare the air electrode, 8 mg of Co_3O_4 particles and 0.8 mg of carbon black were dispersed in 4 ml of ethanol/water (1 : 1 ratio) and 70 μL of 5% Nafion solution by ultrasonication for 30 min to form a homogeneous catalyst ink. The air electrode (gas diffusion layer, PTFE treated carbon paper) with confined circular area of 1.54 cm^2 was drop coated with 600 μL of the ink to achieve a catalyst loading of 0.779 mg/cm^2. 2 M KOH was used as the electrolyte, and a polished Zn foil was used as the negative electrode. In the two-electrode configuration cell, the Zn foil functioned as counter and reference electrodes, simultaneously. The phase transformation on the surface of a cobalt-based catalyst is detectable due to the fact that the synchrotron radiation is a powerful tool with a very high resolution. It has been demonstrated that a layered CoOOH formation on rock-salt CoO_x coated on Co_3O_4 cube, where Co_3O_4 acted as the support, was detected by using the same X-ray light beam source.[36] In which, although the coating layer of CoO_x was only ~ 9 Å in thickness on surface, the *in-situ* XRD signals of layered CoOOH formation were still very clear, indicating the phase evolution on the CoO_x layer during OER. In addition, the *in-situ* XAS measurement of Co_3O_4-cube could be able to further verify the applicability and accuracy of our *in-situ* metal-air cell in which it was capable to detect the small variation happening on the catalyst surface.

In-situ Raman spectra were collected under controlled electrochemical potentials using a homemade epoxy pool cell on FTO substrate, in which a controlled active area of 0.384 cm^2 by using an insulation layer on FTO conductive side was used as the working electrode. The catalyst was dispersed in deionized (DI) water (catalyst concentration: 5 mg/mL) by sonication for 24 h to obtain a homogeneous ink. Following, 10 μL of the catalyst ink was drop-casted on the confined active area (0.385 cm^2). The electrode was dried at ambient condition for 24 h, followed by heated at 60 ^oC for 30 min. Two polished Zn foils were attached near to the active catalyst, used as counter and reference electrodes, respectively. Epoxy pool was directly built on the FTO substrate. Only a few droplets of 1 M KOH were placed inside the pool as electrolyte to minimize the light scattering. Raman spectra were collected using a Raman spectrometer (JY HR Evolution) with a

532 nm excitation laser with a power of 2.1 mW measured at the objective. Acquisition time was set as 200 s for the spectral Raman shift ranging from 400 to 1200 cm^{-1} window using a 600 g/mm grating. Additional details for *in-situ* Raman measurements can be found in **Figure 4-6**. To quantify the relative variation in the peak intensities, the method of baseline substitution was used. The standard redox potential ($Zn/Zn(OH)_4^{2-}$) of the reference electrode is -1.25 V vs. SHE,[133] and thus, the applied potential was converted to the RHE scale using the following equation: $V_{RHE} = V_{Zn/Zn(OH)_4^{2-}} + V^0{}_{Zn/Zn(OH)_4^{2-}} + 0.059 \times pH$.

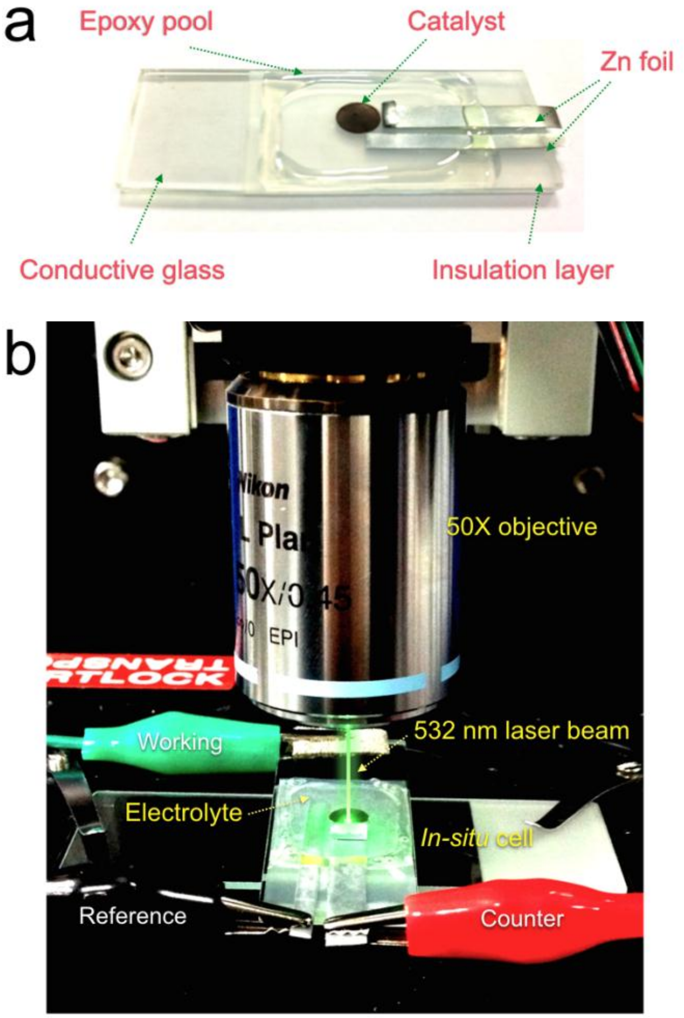

Figure 4-6. *In-situ* Raman measurement. (a) Details of the *in-situ* Raman cell. (b) Set-up of *in-situ* Raman measurement.

4.3 Real-time observation of the crystallographic information of Co_3O_4 during the Zn-Air cell operation.

We adopted the configuration of the metal-air battery cell, where Co_3O_4 powder (calcined at 800 ^oC) dropped coated on PTFE treated graphite paper acted as the cathode in an operating metal-air battery (see the supporting information for the detail),[132] for *in-situ* XAS and grazing-angle XRD studies. As shown in **Figure 4-7a**, during cell discharging, ORR took place on Co_3O_4, which displayed negative current. While upon charging the cell by increasing bias, a typical LSV curve of OER with an obvious anodic peak at 1.89 V vs. $Zn/Zn(OH)_4^{2-}$ (or 1.45 vs. RHE, refer to the Supporting Information for the details of voltage conversion) and an onset voltage at 2.01 V vs. $Zn/Zn(OH)_4^{2-}$ were developed. The declined performance at high voltages (> 2.15 V vs. $Zn/Zn(OH)_4^{2-}$) is due to the limited coverage of surface intermediates.[123] The anodic peak prior to the rise of OER current was usually attributed to the increase of valence states of cobalt ions (e.g., Co^{2+}/Co^{3+} or Co^{3+}/Co^{4+} redox couple) with an expected phase transformation (e.g., $Co_3O_4 \rightarrow Co(OH)_2/CoOOH$ or $CoOOH \rightarrow CoO_2$).[26,35-39,34] However, as depicted in **Figure 4-7b**, our *in-situ* grazing angle XRD result indicated that the intensities and positions of the main diffraction peaks of Co_3O_4 were nearly unaffected during the entire ORR and OER processes, suggesting stable cubic-spinel structure under either negative or positive bias. **Figure 4-7c** displays the *in-situ* extended X-ray absorption fine structure (EXAFS) spectra obtained from the k^3-weighting EXAFS spectra in k-space (**Figure 4-8a and b**). It reveals that the interatomic distances of Co^{3+}_{Oh} and Co^{2+}_{Td} to their neighboring metal atoms in Co_3O_4 remain nearly unchanged in the voltage range between 0.9 to 2.3 V vs. $Zn/Zn(OH)_4^{2-}$, where the intensity ratio between the $Co\text{-}Co_{(Oh)}$ peak, I_{Oh}, to $Co\text{-}Co_{(Td)}$ peak, I_{Td}, is estimated as $I_{Oh}/I_{Td} = 1.42$ for the entire process. The corresponding Co K-edge X-ray absorption near edge structure (XANES) spectra (**Figure 4-8c and d**) give the edge-jumping positions, which show no obvious variation in cobalt valence states under different applied biases, yet a slightly expanded and compressed Co-O bond can be noticed during ORR and OER (**Figure 4-7c**), suggesting that there are some negative/positive charges accumulated on the cobalt centers with increasing/decreasing bias. The High resolution transmission electron microscopy (HRTEM) images further indicates that there is no newly formed CoOOH layer structure on the Co_3O_4 surface after applying bias (**Figure 4-9**).

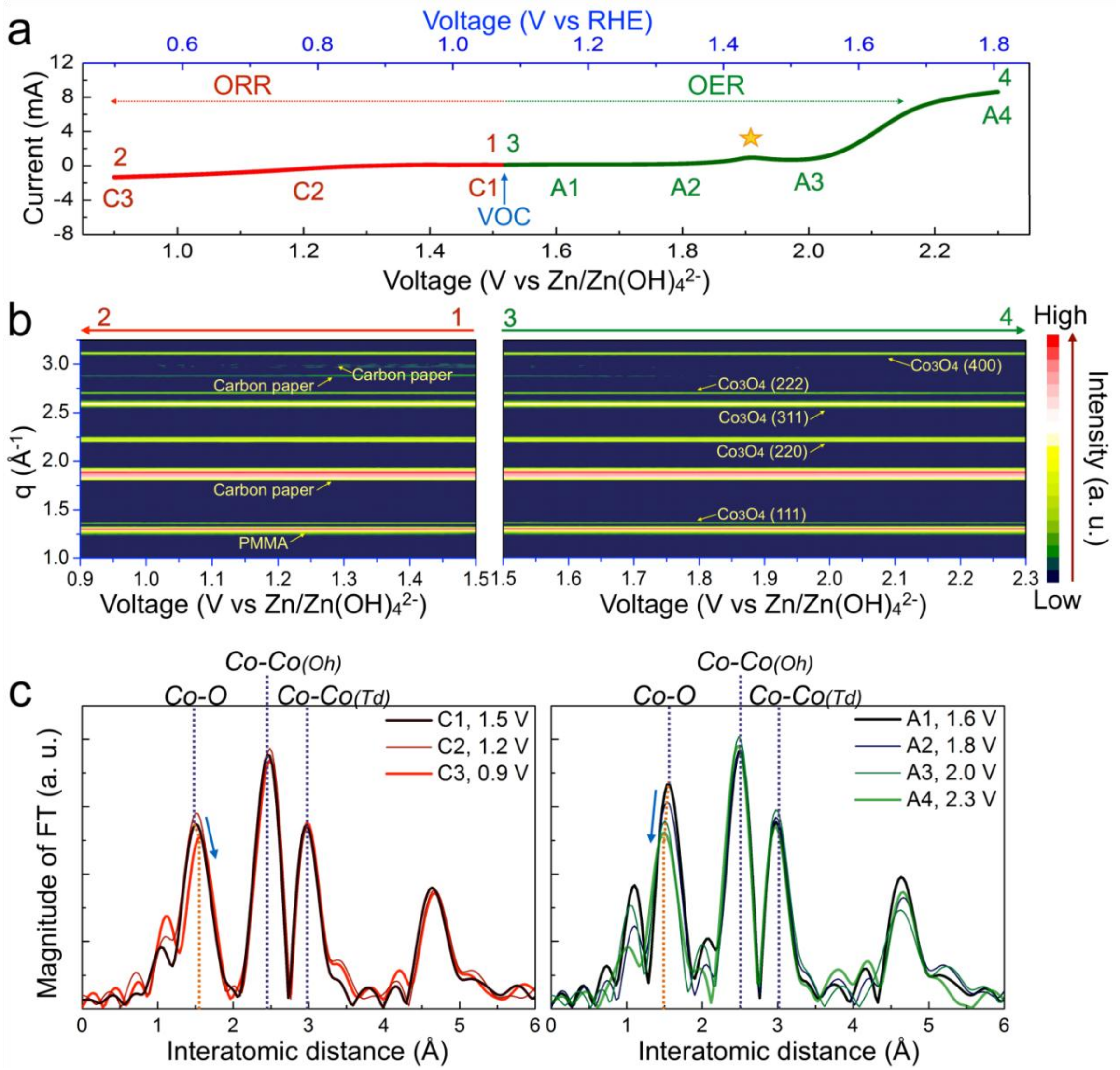

Figure 4-7. *In-situ* grazing-angle X-ray diffraction and X-ray absorption spectroscopy measurements. (a) The linear scanning voltammetry (LSV) curve of Co_3O_4, where the voltage at open circuit (VOC) was 1.52 V vs. $Zn/Zn(OH)_4^{2-}$ at the beginning and the yellow star marked an obvious anodic peak. (b) X-ray diffraction patterns recorded following the sequence from 1→2

(ORR condition) then 3→4 (OER condition) as indicated in the LSV curve. (c) Co K-edge EXAFS spectra measured following the sequence from C1→C2→C3 (ORR condition) then A1→A2→A3→A4 (OER condition) as indicated in the LSV curve, in which the voltage is in the scale vs. Zn/Zn(OH)$_4^{2-}$.

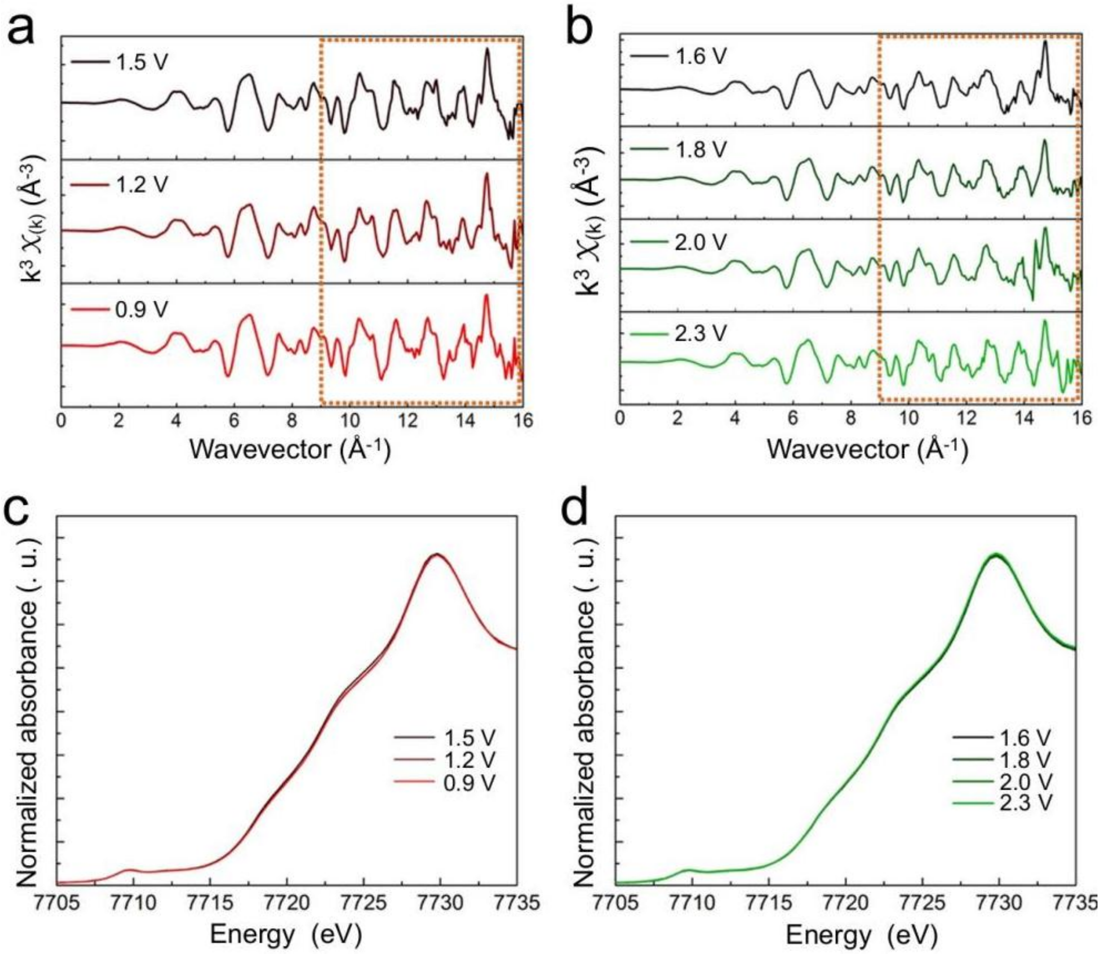

Figure 4-8. k^3-weighting X-ray absorption near edge structure (XANES) spectra of Co_3O_4 in k-space under (a) ORR and (b) OER conditions. From which, it can be observed that the vibration gradually changes in the range of 9 – 16 wavevector during both ORR and OER. Normalized *in-situ* Co K-edge extended X-ray absorption fine structure (EXAFS) spectra under (c) ORR and (d) OER conditions, where the voltage is in the scale vs. Zn/Zn(OH)$_4^{2-}$.

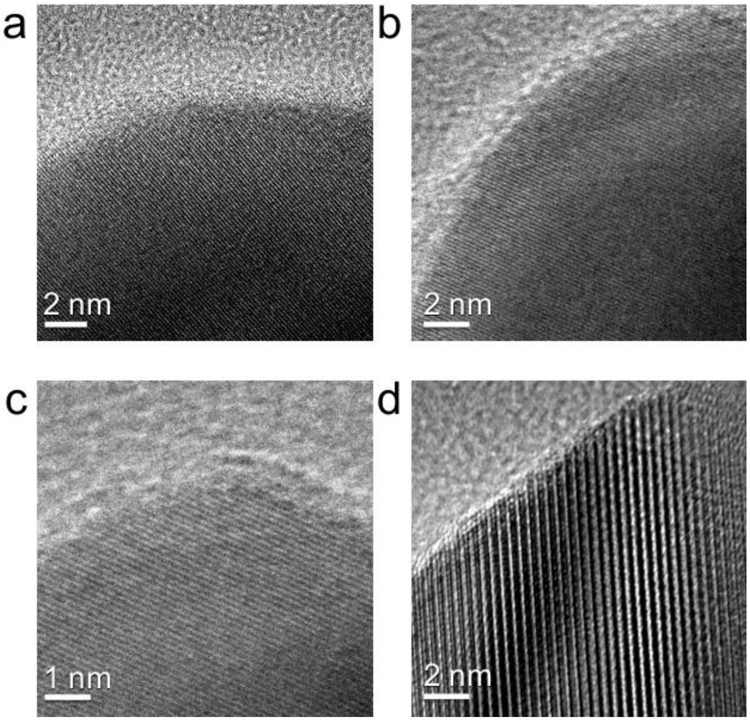

Figure 4-9. HRTEM images of clacined Co_3O_4 particle (a) before and (b-d) after *in-situ* XAS measurement.

Our *in-situ* XAS and XRD results are contradictory to the current literature,[35,36,53,134,135] in which it is believed that layered cobalt oxyhydroxide will be formed on the surface of spinel Co_3O_4 prior to the onset potential of OER as indicated by the obvious anodic peak. Although it has been evidenced by EPR study that the Co ions in phosphate containing cobalt oxide (or *Co-Pi*) catalyst can be oxidized to Co^{4+} during water oxidation,[136] our XAS data demostrates no clear influence of cobalt valence states in Co_3O_4 with increase in aoolued bias. In addition, the EXAFS spectra revealed a similar feature of *Co-Pi* with layered CoOOH, suggesting an edge-sharing CoO_6 geometry in *Co-Pi* with the octahedral Co ions center in the cubane structure.[109] Furthermore, it is worth noting that some cobalt based catalysts synthesized by electrochemical deposition (ED)[53,135] did not go through the Co_3O_4 phase with bias increasing as indicated in the Co-H_2O Pourbaix diagram, where Co_3O_4 should be present as the intermediate phase between cobalt hydroxide and cobalt oxyhydroxide.[34] James B. *et al.* revised the Pourbaix diagram due to the fact of lacking a characteristic signal of tetrahedral Co^{2+} in their *in-situ* EPR spectra of the electrochemically deposited cobalt oxide (denoted as CoO_x), suggesting that CoO_x could not be converted to Co_3O_4 electrochemically.[135] To reconcile the observed apparent stable cubic spinel structure and unchanged valence states of Co ions in Co_3O_4 during OER with the adjustable structure of CoO_x, we propose that spinel Co_3O_4 should be intrinsically distinct from CoO_x. The Co-H_2O Pourbaix diagram maps out the thermodynamic equilibrium of Co ions in a particular electrochemical aqueous system, in which only activities of free Co ions are considered.[34] However, the Co ions in solid spinel Co_3O_4 have been strongly bonded with O anions. Additionally, the Pourbaix diagram ignores the kinetic effects. As a result, it might not be appropriate to deduce the origin responsible to the anodic peak which shows up instantaneously with increase in bias simply based on the Co-H_2O Pourbaix diagram. The samples prepared by ED[35,53,134,135] or chemical bath deposition (CBD)[36] without thermal annealing may contain some impurities (e.g., rock-salt CoO) or allow certain amounts of hydroxyl groups and/or water molecules to remain in the bulk structure, making them flexible to undergo bulk redox activity and therefore phase transformation.[127] On the contrary, it usually requires a high-temperature treatment to convert cobalt based hydrates to pure spinel Co_3O_4.[130,137]

4.4 Physical and chemical characteristic of the anodic peak of spinel Co_3O_4 prior to the rise of OER current.

To gain more in-depth information about the anodic peak of Co_3O_4 prior to the OER onset, a series of well-designed CV experiments were carried out. Nickel oxide (NiO_x), which exhibits an obvious reversible wave in the CV resulting from the Ni redox process (Ni^{2+}/Ni^{3+}) in an alkaline solution along with phase transformation from rock-salt structure to layered $Ni(OH)_2$/NiOOH structure,[127,138] is selected as the control to demonstrate the electrochemical behavior of the oxidation peak where bulk redox reaction indeed takes place. The Co_3O_4 and NiO_x grown on FTO (F:SnO_2) substrate were directly used as the working electrode. Notably, it required a long-time cycling to achieve complete $NiO_x \rightarrow Ni(OH)_2$ transformation as the wave kept increasing in area, and eventually, nearly all of the Ni centers were electrochemically active (reversible $Ni(OH)_2 \rightarrow NiOOH$) and the wave became stable in the subsequent CV scans[127] (**Figure 4-10**).

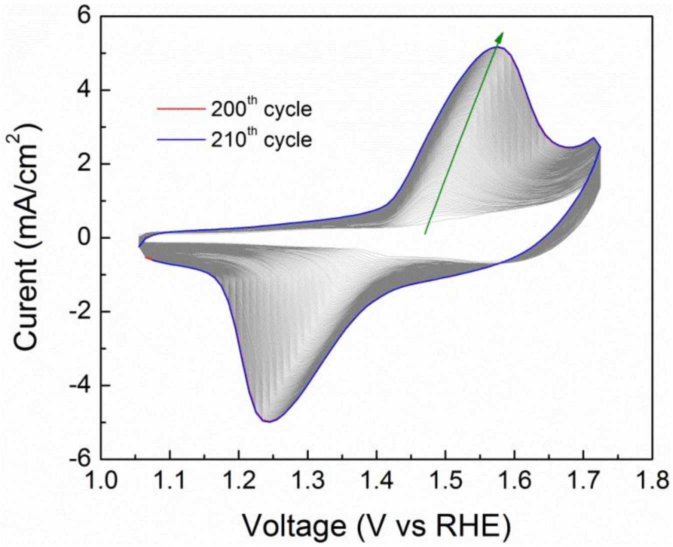

Figure 4-10. Activation process of NiO_x to $Ni(OH)_2$/NiOOH. After 200 CV cycles, the oxidation wave tended to be stable as revealed by the comparison between the CV curves of the 200th and 210th cycle.

Generally, the oxidation peak current (I_P) obeys the power-law relation with scan rate (ν)[139]:

$$I_p = a\nu^b$$

where I_P is the peak current, a and b are adjustable parameters, and the value of b can be estimated from the slope of the log I_P vs. log ν plot. There are two well-defined conditions: (i) if b is close to 0.5, the current is controlled by semi-infinite linear charge diffusion, indicative of a faradaic redox process in the bulk, and (ii) if b is close to 1.0, it indicates that the oxidation peak is a surface reaction limited response.[140] As revealed in **Figure 4-11a**, b was determined to be ~ 0.56 for NiO_x

during anodic scan, suggesting a charge diffusion limited bulk redox process. On the contrary, spinel Co_3O_4 showed a surface reaction controlled behavior as its b value was ~ 0.93 (**Figure 4-11b**). The underlying properties of surface reaction could be further differentiated from the bulk redox process by observing the influence of the alkaline concentration on the maximum intensity of the anodic peak. As NiO_x went through $Ni^{2+} \rightarrow Ni^{3+}$ even higher valent nickel peroxide[141] transition with nearly all Ni centers being electrochemically active, increasing OH^- concentration could improve the faradaic kinetics (e.g., charge diffusion rate into the bulk), leading to enhanced peak current intensity as shown in **Figure 4-11c**. However, the peak current remained nearly constant for spinel Co_3O_4 (**Figure 4-11d**), indicating that the reaction kinetics was mainly controlled by the number of exposed active sites on surface.

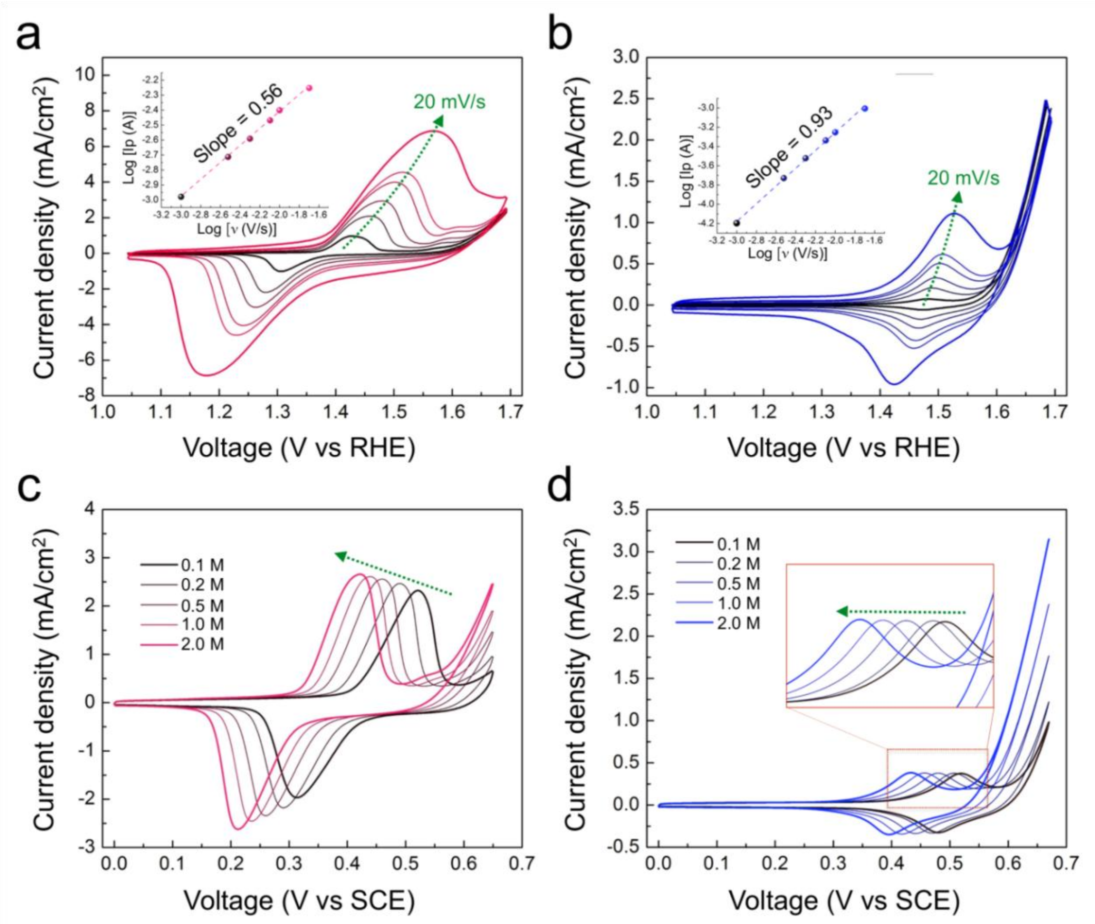

Figure 4-11. Electrochemical properties of the oxidation peak. CV curves with scan rate at 1 mV/s, 3 mV/s, 5 mV/s, 8 mV/s, 10 mV/s, and 20 mV/s of (a) NiO_x and (b) Co_3O_4 electrode. From which, parameter b can be determined by plotting log(I_P, anodic peak current) versus log(ν, scan rate). CV curves with scan rate at 5 mV/s in 0.1 M (pH = 12.61), 0.2 M (pH = 12.82), 0.5 M (pH = 13.32), 1.0 M (pH = 13.73), and 2.0 M (pH = 13.89) KOH of (c) NiO_x and (d) Co_3O_4 electrode. It is noted that the position of oxidation peak shifts toward the lower voltage vs. SCE with increase of KOH concentration due to the fact of pH increase.

The redox wave observed on spinel Co_3O_4 is intrinsically different from the redox wave of $Co(OH)_2$/CoOOH. Here, we used the work by Burke et. al.[142] as the example, First, in Burke's work, the redox position of $Co(OH)_2$/CoOOH is around 1.05 V vs. RHE. But, the anodic peak on spinel Co_3O_4 is ~1.45 V vs. RHE. Second, it was found that there existed an irreversible phenomenon of $Co(OH)_2$/CoOOH in the first CV cycle, but for Co_3O_4, the redox wave prior to the OER onset remained almost unchanged between the first and the second cycle as shown in **Figure 4-12a**.

The integrated capacitance of the anodic peak in the voltage range between 1.35 to 1.55 V vs. RHE (based on CV result of Figure 2b in the manuscript) is ~ 7.035×10^{-4} C /cm^2. The measured roughness factor (R_f) was estimated from the double-layer capacitance method using cyclic voltammetry in a small potential range (1.16 to 1.24 V vs. RHE), from which the double layer capacitance was determined from the slope of the capacitive current (I_{cap}) at the midpoint of the scan range (1.2V vs. RHE) versus the scan rate according to $C_{dl} = I_{cap}/(dE/dt)$, where C_{dl} is the double layer capacitance and dE/dt is the scan rate. R_f was calculated through dividing the slope by 40 μF/cm^2 (capacitance of a smooth surface for transition metal oxide in alkaline solution).[118] The calculated R_f for the hydrothermally synthesized Co_3O_4 electrode is ~112 (**Figure 4-12b**). Here we take the (100) facet of spinel Co_3O_4 as an example (the cobalt atomic density on other Co_3O_4 facets should be within the same scale). The lattice constant for cubic spinel Co_3O_4 is 8.048 Å, and each unit square on (100) facet contains 2 cobalt atoms.[105] Thus, the cobalt atomic density is estimated as ~ 4.3×10^{16} atoms/cm^2. If we assume all surface cobalt atoms participating in the reaction ($1e^-$/atom), the theoretical surface capacitance on the electrode will be 5.53×10^{-3} C /cm^2, which is 7.86 times larger than the integrated capacitance of the anodic peak. We believe this is an acceptable number, which supports that the anodic peak of spinel Co_3O_4 is mainly related to the surface reaction rather than a bulk redox reation.

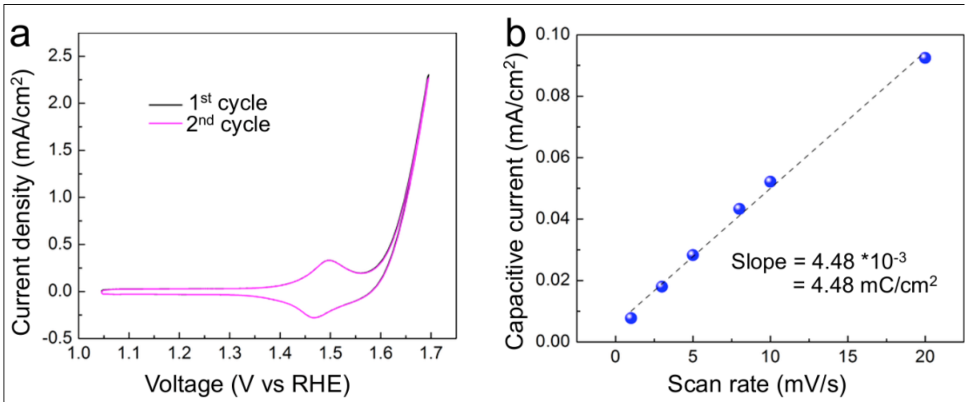

Figure 4-12. (a) The first two CV curves of hydrothermally prepared Co_3O_4 electrode at a scan rate of 5 mV/s in 1 M KOH. (b) Dependence relation of the capacitive current vs. scan rate.

Although the anodic peak is well separated from the OER onset, we could not totally exclude the possibility of occurrence of reactions involving the oxygenated intermediates before the OER onset. In general, the OER mechanism in alkaline solution on metal sites begins with a proton-coupled electron transfer from the surface adsorbed aquo species (OH*), which is the crucial beginning step for the OER process [19,20] as as eqn.11-14 in Chapter 1.2. Unlike photocatalysis where driving force can be suddenly pumped by light irradiation, the activation energy for electrocatalysis is provided by the external bias. For an ideal OER electrocatalyst, the required activation energy (ΔG) in each elementary step is 1.23 V vs. RHE. However, for a real electrocatalyst, the OER onset is controlled by the rate determining step (RDS), which requires the highest ΔG (> 1.23 V vs. RHE), meanwhile some of the elementary steps require less ΔG (< 1.23 V vs. RHE). Therefore, we concluded that the anodic peak could be ascribed to the formation of some particular intermediates, which should be justifiable due to that fact that the voltage of the anodic peak is already larger than 1.23 V vs. RHE once the applied bias is large enough to satisfy the requirement of ΔG for the RDS and other kinetical influences, the OER current will start to rise, and all elementary steps shall have no obstacle to complete the OER cycles repeatedly. Thus, based on the above observations and discussions, we could conclude that the anodic peak prior to the OER onset for spinel Co_3O_4 should be ascribed to a specific surface reaction rather than pure bulk redox process.

Single-crystal Co_3O_4 nanocubes synthesized by chemical deposition under reflux condition without calcination[36] was employed to verify our assumption. Owing to the wet synthesis process, the impurities or hydroxyl groups and/or water molecules may be introduced into the structure of Co_3O_4 nanocubes, and thus the surface of Co_3O_4 nanocubes could be partially oxidized and transformed to layered CoOOH structure[36] as indicated in **Figure 4-13**. Moreover, the b value was estimated to be 0.82 based on the CV measurement (**Figure 4-14**), which suggests the anodic peak current was partially shifted to be charge diffusion controlled in terms of bulk oxidation as well as structural transformation from Co_3O_4 to layered CoOOH.

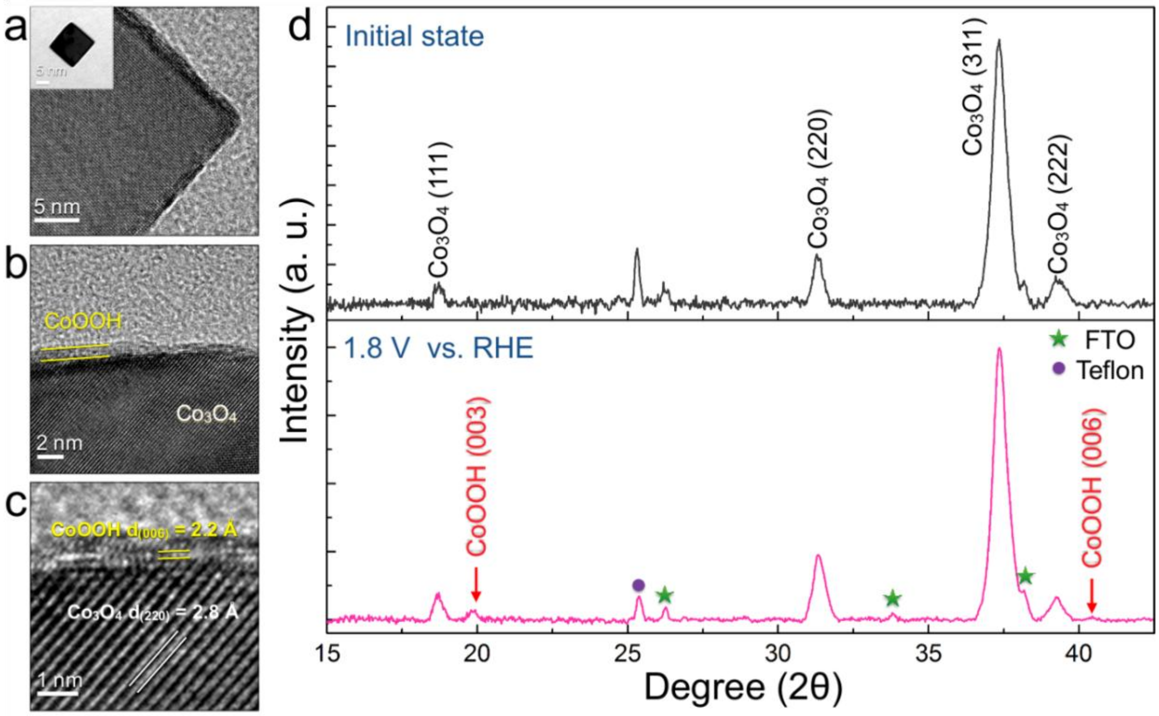

Figure 4-13. (a) Typical TEM (insert) and HRTEM image of a single Co_3O_4 cube. (b-c) HRTEM images of Co_3O_4 cube after applied 1.8 V bias for 2 hrs. (d) The XRD patterns of Co_3O_4 cube before and after applied 1.8 V bias for 2 hrs. This measurement was carried out using a three-electrodes cell where 1 M KOH was employed as electrolyte, Co_3O_4 cube dropped coated FTO

was used as working electrode, Pt foil and SCE was used as counter electrode and reference, respectively.

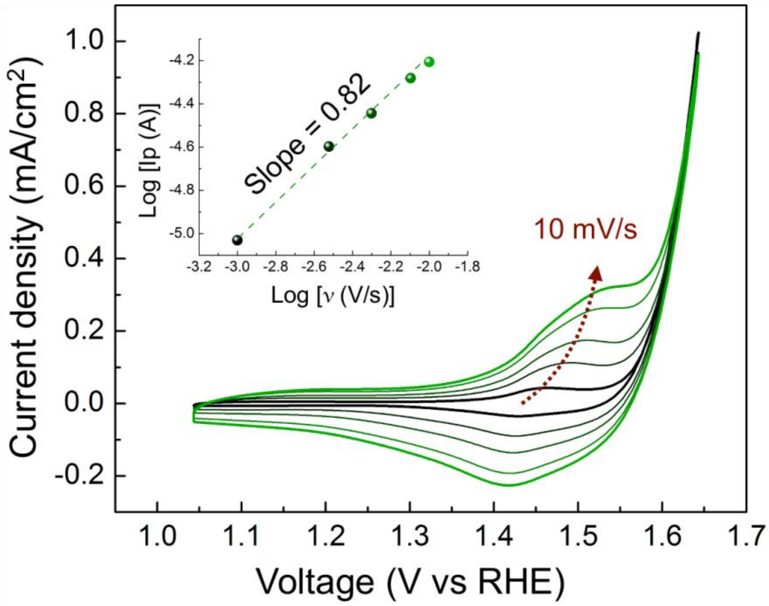

Figure 4-14. CV curves with scan rate at 1 mV/s, 3 mV/s, 5 mV/s, 8 mV/s, and 10 mV/s of Co_3O_4 cube FTO electrode. From which, parameter b can be determined to be ~ 0.82 (insert). This measurement was carried out using a three-electrodes cell where 1 M KOH was employed as electrolyte, Co_3O_4 cube dropped coated FTO was used as working electrode, Pt foil and SCE was used as counter electrode and reference, respectively.

The bulk oxidation of Co_3O_4 nanocubes was further verified by the in-situ XAS measurement using our metal-air cell. As depicted in **Figure 4-15a**, the *in-situ* XANES spectra reveal a slow positive shift of cobalt valence states with the increase of bias. The *in-situ* EXAFS spectra obtained from the k^3-weighting EXAFS spectra in k-space (**Figure 4-15b**) reveals that the interatomic distances of Co^{3+}_{Oh} and Co^{2+}_{Td} to their neighboring metal atoms in Co_3O_4 was gradually changed, as indicated by the peak intensity ratio (I_{Oh}/I_{Td}) shifted from 1.46 to 1.78 with the increase of bias due to the formation of layered CoOOH, in which the Co^{3+} ion is surrounded by six oxygen atoms in the octahedral geometry (**Figure 4-15c**). The aforementioned results support our assumption that the structure of calcined Co_3O_4 should be relatively stable, where the layered CoOOH structure should be not that easily electrochemical transformed on the surface. Based on the above analysis, we could conclude that the anodic peak prior to the OER onset for spinel Co_3O_4 should be mainly contributed from a specific surface reaction rather than the bulk redox process.

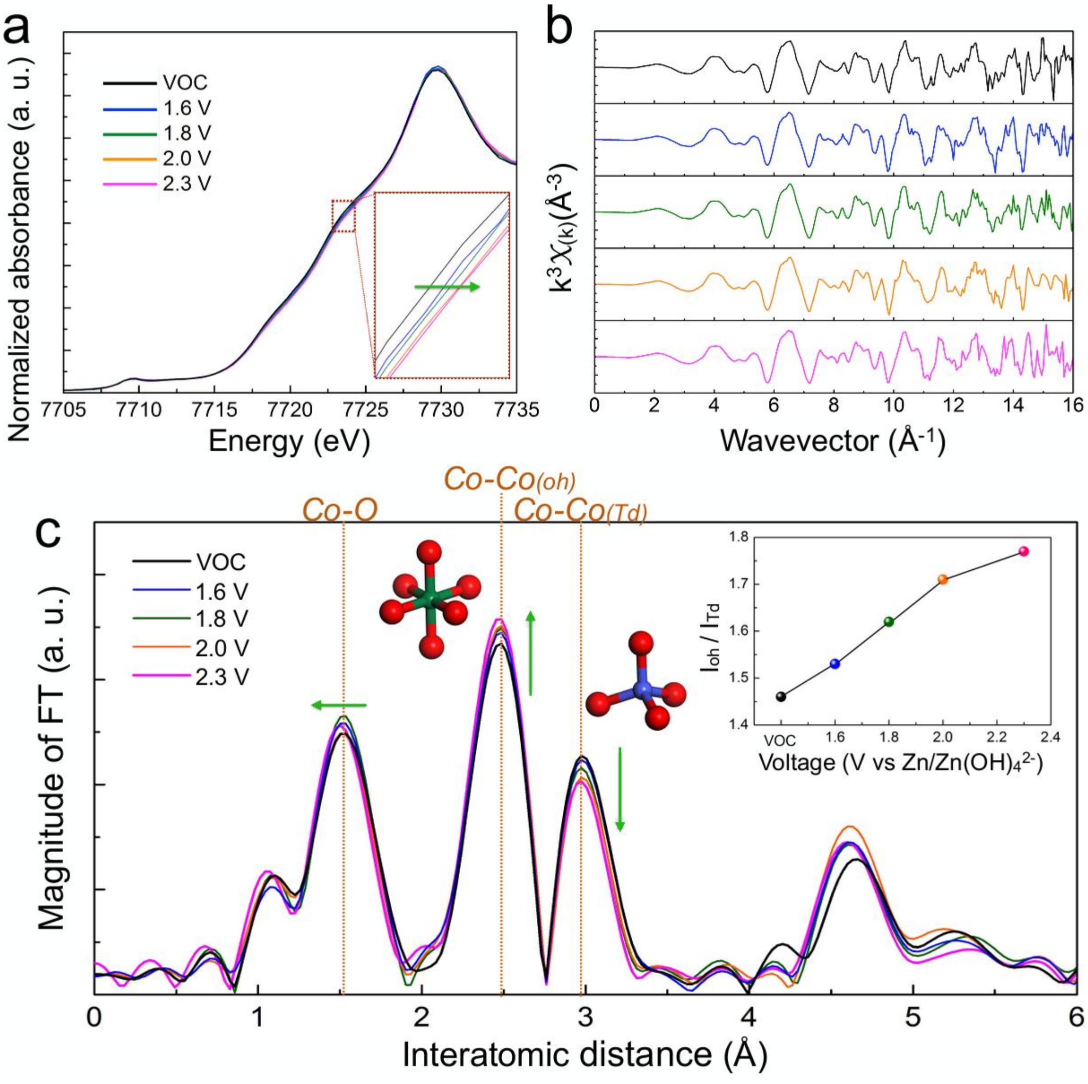

Figure 4-15. (a) Normalized *in-situ* Co K-edge extended X-ray absorption fine structure (EXAFS) spectra of Co_3O_4 cube under conditions, and (b) corresponding k^3-weighting X-ray absorption near edge structure (XANES) spectra in k-space under OER conditions. (c) Co K-edge EXAFS spectra measured under OER condition, in which the Co-Co($_{Oh}$) peak intensity (I_{Oh}) greadually increased

and Co-Co($_{Td}$) peak intensity graudally decreased with the increase of bias as indicated in the inset. In addition, a slightly expanded Co-O bond can also be noticed. This in-situ XAS measurement was carried out using the in-situ metal-air cell where the voltage is in the scale vs. Zn/Zn(OH)$_4^{2-}$.

4.5 Determination of the surface reaction on spinel Co_3O_4 via the *in-situ* Raman spectroscopy

The general OER mechanism in alkaline solution on a metal site begins with a surface-adsorbed aquo species (OH_{ads}) followed by an oxygen-oxygen (OO) single bond formation.[19,20] Therefore, we hypothesize that the anodic peak of spinel Co_3O_4 could be nothing but the outcome of the oxidation of surface intermediates. *In-situ* Raman measurement was then carried out to probe the potential-resolved variation of the intermediates on Co_3O_4 surface.

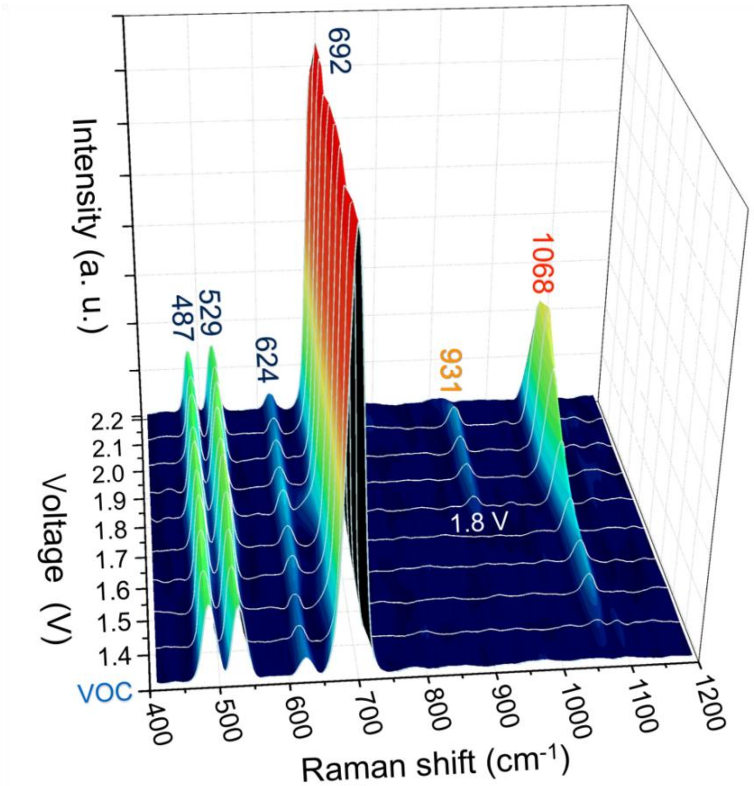

Figure 4-16. *In-situ* Raman measurements. Raman spectra of Co_3O_4 recorded in the voltage range of 1.4 to 2.2 V vs. Zn/Zn(OH)$_4^{2-}$, where VOC was around 1.32 V vs. Zn/Zn(OH)$_4^{2-}$.

As shown in **Figure 4-16**, four Raman-active phonon modes of cubic spinel Co_3O_4, E_g (487 cm^{-1}), F_{2g} (529 cm^{-1}), F_{2g} (624 cm^{-1}), and A_{1g} (692 cm^{-1})[143] were clearly observed, which were nearly unaffected with increase in applied bias. Meanwhile, no other structural Raman signals including $Co(OH)_2$ and layered CoOOH could be detected.[144] Under anodic sweeping, a new Raman peak at 1068 cm^{-1} gradually emerged. The position of this newly formed peak is lower than adsorbed molecular O_2 species (~ 1556 cm^{-1})[145] and free superoxide species (1070–1200 cm^{-1}).[146] Although the Raman peak in the wavenumber region of 800–1150 cm^{-1} was assigned to the "active oxygen" species on Ni oxyhydroxide[147] and Ni-Fe oxyhydroxide,[148] this "active oxygen" assignment may not be appropriate in our case as the crystal structure of spinel Co_3O_4 was well maintained during the electrochemical conditioning. Besides, the nature and formation mechanism of the "active oxygen" species still cannot be equivocally specified.[38] Koper *et. al.*, recently corrected the assignment of the band in the range of 800-1150 cm^{-1} based on the ^{18}O-labeling *in-situ* surface enhanced Raman spectroscopy (SERS) experiments, which revealed a superoxo-type surface species possessing a redshift characteristic as a superoxide moiety.[149] The redshift to lower frequencies by *ca.* 26 cm^{-1} in $H_2{}^{18}O$ electrolyte is also observed for the new Raman peak at 1068 cm^{-1} (**Figure 4-17**) in our experiment, which is identical to the characteristics of the superoxo (OO) species.[146,149] Therefore, we attribute the newly evolved Raman peak to the superoxide moieties that could be produced by a 3-electron oxidation process of the surface adsorbed H_2O intermediates.

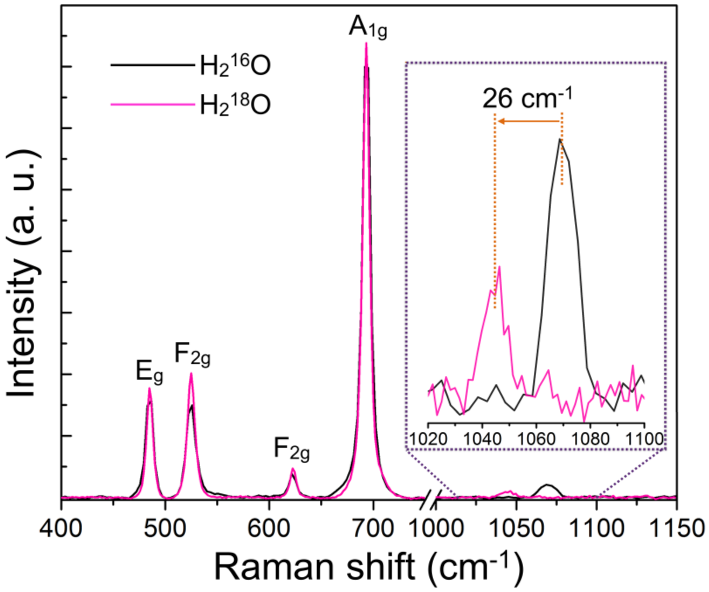

Figure 4-17. Raman spectra of Co_3O_4 obtained at 1.7 V vs $Zn/Zn(OH)_4^{2-}$ in $H_2{}^{16}O$ 1 M KOH and 1.7 V vs $Zn/Zn(OH)_4^{2-}$ in $H_2{}^{18}O$ 1M KOH.

With further increase of bias, another new peak at 931 cm^{-1} starts emerging at the voltage of 1.8 V vs. $Zn/Zn(OH)_4^{2-}$ (or 1.36 V vs. RHE), which is in line with the onset of the anodic peak (**Figure 4-7a and Figure 4-18**) in the LSV scan.

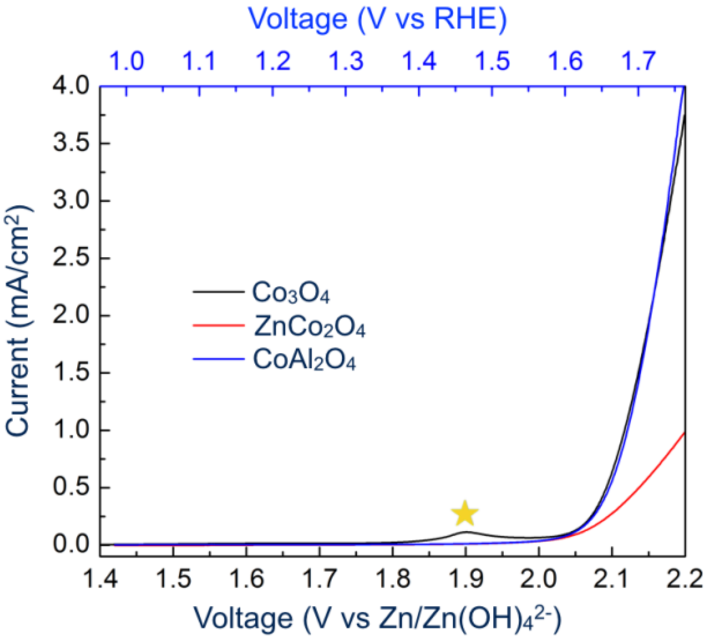

Figure 4-18. Linear scanning voltammetry curves of Co_3O_4, $ZnCo_2O_4$, and $CoAl_2O_4$ obtained at a can rate of 10 mV/s during *in-situ* Raman measurement without i-R compensation. The yellow star marks the position of oxidation peak of Co_3O_4 prior to the rise of OER current.

The position of this peak is higher than the Co(IV)=O vibrational mode at around 840 cm^{-1}.[146] A possible assignment of the peak at 931 cm^{-1} is the peroxide moiety as the OO stretching modes of peroxide generally fall in the range of 640–970 cm^{-1}.[150] Besides, this Raman peak also exhibits a redshift in the ^{18}O-labeled electrolyte (**Figure 4-19**), suggesting that the surface moieties possess the nature of OO bond.[151,152]

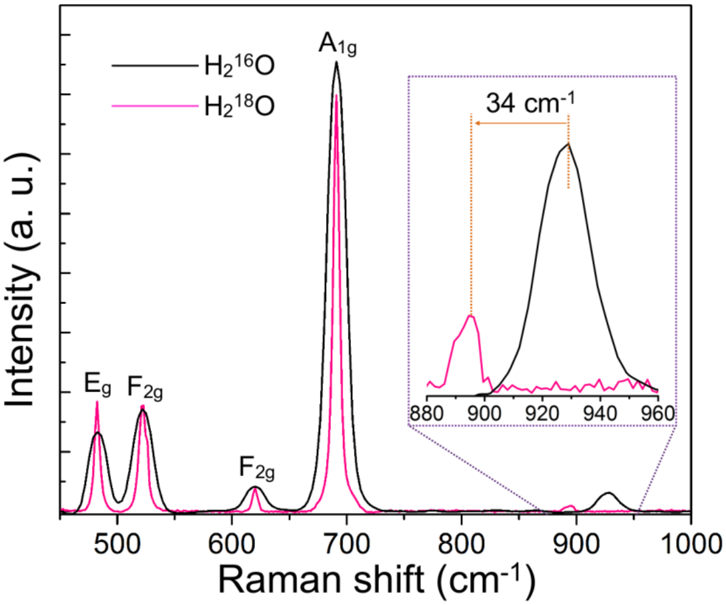

Figure 4-19. Raman spectra of Co_3O_4 obtained at 1.9 V vs $Zn/Zn(OH)_4^{2-}$ in $H_2^{16}O$ 1 M KOH and 1.9 V vs $Zn/Zn(OH)_4^{2-}$ in $H_2^{18}O$ 1 M KOH.

However, since the peroxide is a 2-electron oxidation intermediate during the H_2O oxidation to O_2, this later formed species cannot be directly produced from the early formed superoxide moieties under a positive bias due to the fact that the peroxide (O_2^{2-}) is the product of 1-electron reduction of superoxide (O_2^-). Nevertheless, it seems that the first emerging Raman peak at 1068 cm^{-1} can also fit in the range of 1015–1160 cm^{-1} as assigned for the μ-superoxo (μ-OO) species bridging on two metal centers in CoO–MgO solid solution,[153,154] and the superoxide with μ-OO structure could be produced from the particular peroxide with μ-OO feature by 1-electorn oxidation process. This assignment provides a probable explanation to the formation of the second evolved Raman peak at 931 cm^{-1}. As it has been revealed that the μ-OO coupling process on two metal centers is kinetically slow,[155] an individual observation of μ-OO peroxide (Co-OO-Co) under a higher positive bias should be possible. Because the Co_3O_4 surface is saturated with OH_{ads}, the neighboring OH_{ads} moieties could connect to each other undergo a 2-electron oxidation process, leading to the surface moieties with μ-OO structure, in which the μ-OO peroxide moieties can thus be produced. A similar bridging scenario of direct μ-OO coupling on the dicobalt edge sites has been probed using a dinuclear cobalt complex.[155]

As previously reported,[90] we found that tetrahedral zinc (Zn^{2+}_{Td}) substituted Co_3O_4 ($ZnCo_2O_4$) showed a vanishing anodic peak feature (**Figure 4-18**), which now may be comprehended due to the missing characteristic of μ-OO peroxide moieties (**Figure 4-19a**). The low intensity of superoxide at 1065 cm^{-1} and the vanishing Raman peak at around 926 cm^{-1} indicates the crucial role of Co^{2+}_{Td} to initiate the μ-OO bridging process, and thus, the OER catalyzed by $ZnCo_2O_4$ is rate-limited at the beginning step where the coverage of surface intermediate is low (Tafel slope of 113 mV/dec[90] close to the featured Tafel slope of 120 mV/dec[18]). Though octahedral aluminum (Al^{3+}_{Oh}) substituted Co_3O_4 ($CoAl_2O_4$) with a small Tafel slope (60 mV/dec) [90] exhibited a μ-OO peroxide stretching band at 928 cm^{-1} along with the characteristic $CoAl_2O_4$ Raman peaks[156] (**Figure 4-19b**), the required bias to form the μ-OO peroxide moieties is too high at 2.0 V vs. $Zn/Zn(OH)_4^{2-}$. Therefore, the anodic peak current could be overlapped with its OER current in which the onset is ~ 2.05 V vs. $Zn/Zn(OH)_4^{2-}$ (**Figure 4-18**).

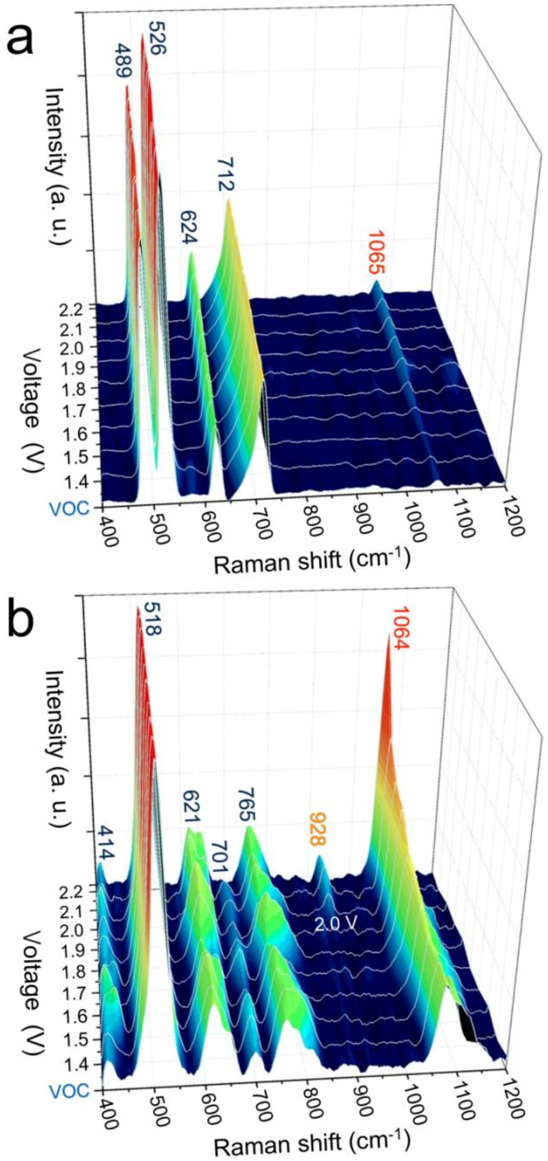

Figure 4-20. *In-situ* Raman measurements. Raman spectra of (a) $ZnCo_2O_4$ and (b) $CoAl_2O_4$ recorded in the voltage range of 1.4 to 2.2 V vs. $Zn/Zn(OH)_4^{2-}$ in the *in-situ* Raman cell, where VOC was around 1.35 V vs. $Zn/Zn(OH)_4^{2-}$ for $ZnCo_2O_4$ and 1.29 V vs. $Zn/Zn(OH)_4^{2-}$ for $CoAl_2O_4$. The characteristic Raman peaks of $ZnCo_2O_4$ and $CoAl_2O_4$ in the wavenumber range < 800 cm^{-1} match well with the reported data in the literature.[156,157] However, due to the inevitable fluorescence-effect for the $CoAl_2O_4$ sample, some feature peaks e.g., superoxide (1064 cm^{-1}) signal were superimposed with the fluorescence background that appeared at the beginning of the measurement.

4.6 The role for the anodic peak of spinel Co3O4 prior to the onset of OER.

We have revealed the underlying additional origin of the oxidation peak on Co_3O_4 during water oxidation electrocatalysis, which could be ascribed to the oxidation of surface adsorbed intermediates to form peroxide (O_2^{2-}, Co-OO-Co or Co-OOH) moieties rather than the bulk redox process. It was found that $Co^{2+}{}_{Td}$ in Co_3O_4 was essential for the formation of peroxide moieties due to its crucial role to bridge the μ-OO bond or the formation of negatively charged superoxo moieties. Our work disclosed the hiding chemical step reaction under the anodic peak current where $Co^{2+}{}_{Td}$ should be responsible for the initiation of the reaction. Though we did not find a clear phase transformation on the calcined Co_3O_4, the layered CoOOH strucutre can still be observed on the Co_3O_4 syntheized by wet method. Besides, the thermodynamically stable hydrated oxide products could be limited by the slow kinetics. Thus, we reserve the possibility that the hydrated oxide layer can be formed under a long-term OER as such “corrosion phenomenon” is commonly observed on metal oxide based electrocatalyst.[158]

Chapter 5. Conclusion

Efficient and earth abundant electrocatalyst for high-performance oxygen evolution reaction (OER) is essential for the development of sustainable energy conversion technology. In the first part of this thesis, a new hierarchical Ni-Co oxide nanostructure, composed of small secondary nanosheets grown on primary nanosheet arrays, was first synthesized via a topotactic transformation of Ni-Co layered double hydroxide (LDH). The Ni^{3+} rich surface benefited the formation of NiOOH, which is the main redox site as revealed via *in-situ* X-ray absorption near edge structure (XANES) and extended X-ray absorption fine structure (EXAFS) spectroscopy. The Ni-Co oxide hierarchical nanosheets (NCO-HNSs) deliver a stable current density of 10 mA/cm^2 at a low overpotential of ~0.34 V for OER with a Tafel slope of as low as 51 mV/decade in alkaline media. The improvement in the OER activity could be ascribed to the synergy of large surface area offered by the 3D hierarchical nanostructure and the facile formation of NiOOH as the main active species on the surface of NCO-HNSs to decrease the overpotential and facilitate the catalytic reaction.

We not only synthesized an advanced catalyst with unique structure and superior activity toward OER, but also found the substituted Ni ions selectively occupied the tetrahedral sites in the spinel Co_3O_4. This finding attracted our attention for thinking about the possibility of geometrical-site-dependent OER activity in the spinel structure because spinel Co_3O_4, comprising two types of cobalt ions: one Co^{2+} in the tetrahedral site ($Co^{2+}{}_{Td}$) and the other two Co^{3+} in the octahedral site ($Co^{3+}{}_{Oh}$), has been widely explored as promising oxygen evoltuion reaction (OER) catalyst for water electrolysis. However, the roles of two geometrical cobalt ions toward the OER have remained elusive. Thus, in the second part of my thesis, we investigated the geometrical-site-dependent OER activity of Co_3O_4 catalyst by substituting $Co^{2+}{}_{Td}$ and $Co^{3+}{}_{Oh}$ with inactive Zn^{2+} and Al^{3+}, respectively. Following a thorough *in-operando* analysis by electrochemical impedance spectroscopy and X-ray absorption spectroscopy, it was successfully revealed that $Co^{2+}{}_{Td}$ site was responsible for the formation of peroxide moieties, Co-OOH, which acted as the main active site for water oxidation. On the other hand, the Co^{3+}_{Oh} site ended to stably bond with –OH groups, limiting its catalytic activity.

Apart from the geometrical-site-dependent activity of spinel Co_3O_4 has been successfully disclosed, we were also surprised the anodic peak prior to the rise of OER current could be vanished if we substituted Zn^{2+} into the tetrahedral site of Co_3O_4. In general, it has been believed that the cobalt ions in spinel Co_3O_4 should be oxidized during the oxygen evolution reaction (OER). Therefore, the observed evident anodic peak prior to the rise of the OER current in the linear sweep voltammetry (LSV) scan in spinel Co_3O_4 was solely ascribed to the oxidation of cobalt ions accompanying with a phase transformation. Due to the fact that the present of this anodic peak could be manipulated by substituting the cobalt ions with other metal ions, we decided to further study the underlying properties of oxidation peak. Here, in the third part, through a combination of well-designed independent in-situ measurements including X-ray absorption and grazing-angle X-ray diffraction under operando conditions, we found that both the spinel structure and cobalt valence states in Co_3O_4 actually remained unchanged during electrochemical water oxidation, which contradicted to the current literatures in which a new phase of hydrated cobalt oxide should be formed. Following a potential-resolved in-situ Raman analysis, it was revealed that the anodic peak current could be mainly contributed from the formation of peroxide moieties (e.g., Co-OO-Co or Co-OOH) on the surface of Co_3O_4, and more importantly, the tetrahedral Co^{2+} ions in Co_3O_4 should be the crucial sites to bridge the μ-OO bond.

Compared to the Ni substituted Co_3O_4 hierarchical nanosheets (NCO-HNSs) where a new NiOOH phase was formed as the active main species toward OER, a pure spinel Co_3O_4 did not go through the phase transformation from spinel to layered CoOOH structure with the increase of bias, yet a surface intermediate of peroxide moiety (Co-OOH) was detectable instead. It was highlighted that not only the activity, but the physical and chemical properties of bulk spinel Co_3O_4 could also be changeable by replacing the Co ion with other OER active metal ions.

In summary, the complete scenario of the OER mechanism on spinel Co_3O_4 has been successfully revealed by a series of well-designed independent in-situ measurements including electrochemical impedance spectroscopy (EIS), X-ray absorption (XAS), grazing-angle X-ray diffraction (XRD), and Raman spectroscopy under operando conditions. We realize that in spinel Co_3O_4, the OER activity is actually geometrical-site dependent. The $Co^{2+}{}_{Td}$ and $Co^{3+}{}_{Oh}$ play different roles during the electrochemical water oxidation, where $Co^{2+}{}_{Td}$ dominates the main OER activity yet $Co^{3+}{}_{Oh}$ shows a relatively strong capacitance feature. Furthermore, the catalytic activity of spinel Co_3O_4 can be modulated by substituting foreign metal atoms with the Co ions at a desired geometrical site, e.g., we have demonstrated that the replacing the tetrahedral Co ion with another OER active species of Ni ion in Spinel Co_3O_4 could greatly enhance the overall activity toward OER.

Apart from the activity, we have disclosed the step-by-step surface intermediate reactions on Co_3O_4 by observing the underlying reactions as indicated as the present of anodic peak prior to the rise of OER current. Although the anodic peak is well separated from the OER onset, we could not totally exclude the possibility of occurrence of reactions involving the oxygenated intermediates before the OER onset. In fact, these two matters, the present of the anodic peak and the rise of OER current, are strongly related to each other. In general, unlike photocatalysis where driving force can be suddenly pumped by light irradiation, the activation energy for electrocatalysis is provided by the external bias. As discussed in chapter 1.3, for an ideal OER electrocatalyst, the required activation energy (ΔG) in each elementary step is 1.23 V vs. RHE, which is generally accepted by the density functional theory (DFT) calculations. However, for a real electrocatalyst, the OER onset is controlled by the rate determining step (RDS), which usually requires the highest ΔG (> 1.23 V vs. RHE), meanwhile some of the elementary steps require less ΔG (< 1.23 V vs.

RHE). Thus, with increasing applied voltage, the elementary steps which are not the RDS could still take place as reflected in our *in-situ* Raman spectra, where the negative charged μ-OO and peroxide moieties could be identified before the OER onset (1.45 V vs. RHE). Therefore, we can conclude that the anodic peak could be ascribed to the formation of some particular intermediates, which should be justifiable due to that fact that the voltage of the anodic peak is already larger than 1.23 V vs. RHE Once the applied bias is large enough to satisfy the thermodynamic requirement of ΔG for the RDS and other influences regarding to kinetics, the OER current will start to rise, and all elementary steps shall have no obstacle to complete the OER cycles repeatedly.

Now we can realize the crucial active site on Co_3O_4 toward the OER is Co^{2+}_{Td}, and we also understand that NCO-NHSs could perform a high activity is due to the substitution of Ni^{3+} at tetrahedral site of spinel Co_3O_4. Before the rise of OER current, the formation of peroxide moieties is the RDS. Here, we hypothesize that to further improve the OER efficiency of Co_3O_4 catalyst, further facilitating the formation of peroxide moieties on Co^{2+}_{Td} site is the most possible answer. Except the substitution method we have shown in thesis, intrinsic modulation the chemisorption affinity by turning the stress of Co_3O_4 crystal in terms of changing the d-orbital electronic configuration and distribution[159] is a practicable method because changing the chemisorption energy can be achieved by the means of the utilized interaction between the d-orbital of active Co ions and p-orbital of oxygen intermediates. Thus, a possible further work based on this thesis is then proposed.

In this thesis, we step-by-step revealed the full OER mechanism on spinel Co_3O_4 electrocatalyst carefully and rationally. Each part of the experiment gave rise to an unclear issue which inspired us to further dig out the truth hiding behind the phenomenon. We have modified and developed various *in-situ* techniques to observe the physical and chemical variations on Co_3O_4 during the full process of OER. Eventually, we were able to realize the complete scenario taking place on the spinel Co_3O_4 toward electrochemical water oxidation. In this study, we want to emphasize the importance of *operando* investigations on electrocatalysis for instantaneously probing the real-time electrochemical kinetics and surface reactions. Except the *in-situ* techniques which have been used in this thesis, we believe simultaneously observation the OER product (O_2 gas) generating during the electrochemical condition is also important. For example, Prof. Strasser's group has demonstrated that by coupling the electrochemical working station and mass spectrometry together, an *operando* differential electrochemical mass spectrometry (DEMS) technique can be used to quantitatively de-convolute of the charge injected into the nanostructured Ni–Fe oxyhydroxide OER catalysts or into the reaction for the production of gas molecules.[160] This technique is capable to verify the oxidation process of the catalyst bulk and theoretical Faraday efficiency of the generation of O_2. This in-situ technique has also been used by Prof. Nocera to probe the edge site reactivity of oxidic cobalt by labeling the isotopic O species of ^{17}O on cobaltate clusters.[155] Beyond this, the electrochemical working station could also be connected with different technique such as transmission electron microscopy (TEM), UV-vis spectra, gas chromatography (GC), and other apparatus in order to piece together the complete story of chemical and physical reaction on the catalyst. Our strategy and philosophy is universal, which is appropriate to be applied on various electrochemical catalytic reactions including oxygen evolution reaction, hydrogen evolution reaction, oxygen reduction reaction, and carbon dioxide reduction reaction, which are the latest hottest research topics in the electrocatalytic chemistry. We have demonstrated that by doing such detailed study and gathering all the necessary information regarding to the OER reaction mechanism, rational design a superior electrocatalyst with enhanced activity is possible. We believe this thesis not only concludes a complete story of how spinel Co_3O_4 catalyzes the water oxidation under electrochemical condition, but also encourages people to ruminate over the underlying mechanism and figure out the crucial parameter to further promote the efficiency of any catalytic reaction.

Reference

(1) Mase, K.; Yoneda, M.; Yamada, Y.; Fukuzumi, S. *Nat. Commun.* **2016**, *7*, 11470.

(2) Rasten, E.; Hagen, G.; Tunold, R. *Electrochim. Acta* **2003**, *48*, 3945.

(3) Ibrahim, H.; Ilinca, A.; Perron, J. *Renew. Sust. Energ. Rev.* **2008**, *12*, 1221.

(4) Steele, B. C. H.; Heinzel, A. *Nat.* **2001**, *414*, 345.

(5) Matsumoto, Y.; Sato, E. *Mater. Chem. Phys.* **1986**, *14*, 397.

(6) Fabbri, E.; Habereder, A.; Waltar, K.; Koetz, R.; Schmidt, T. J. *Catal. Sci. Technol.* **2014**, *4*, 3800.

(7) Koper, M. T. M. *J. Electroanal. Chem.* **2011**, *660*, 254.

(8) Lee, Y.; Suntivich, J.; May, K. J.; Perry, E. E.; Shao-Horn, Y. *J. Phys. Chem. Let.* **2012**, *3*, 399.

(9) Frame, F. A.; Townsend, T. K.; Chamousis, R. L.; Sabio, E. M.; Dittrich, T.; Browning, N. D.; Osterloh, F. E. *J. Am. Chem. Soc.* **2011**, *133*, 7264.

(10) Lee, Y.; Suntivich, J.; May, K. J.; Perry, E. E.; Shao-Horn, Y. *J. Phy. Chem. Lett.* **2012**, *3*, 399.

(11) Suntivich, J.; May, K. J.; Gasteiger, H. A.; Goodenough, J. B.; Shao-Horn, Y. *Sci.* **2011**, *334*, 1383.

(12) McCrory, C. C. L.; Jung, S.; Peters, J. C.; Jaramillo, T. F. *J. Am. Chem. Soc.* **2013**, *135*, 16977.

(13) Man, I. C.; Su, H.-Y.; Calle-Vallejo, F.; Hansen, H. A.; Martinez, J. I.; Inoglu, N. G.; Kitchin, J.; Jaramillo, T. F.; Norskov, J. K.; Rossmeisl, J. *Chemcatchem.* **2011**, *3*, 1159.

(14) Ayers, K. E.; Anderson, E. B.; Capuano, C. B.; Carter, B. D.; Dalton, L. T.; Hanlon, G.; Manco, J.; Niedzwiecki, M. In *Polymer Electrolyte Fuel Cells 10, Pts 1 and 2*; Gasteiger, H. A., Weber, A., Strasser, P., Edmundson, M., Lamy, C., Darling, R., Uchida, H.,

Schmidt, T. J., Shirvanian, P., Buchi, F. N., Mantz, R., Zawodzinski, T., Ramani, V., Fuller, T., Inaba, M., Jones, D., Narayanan, S. R., Eds. 2010; Vol. 33, p 3.

(15) Millet, P.; Ngameni, R.; Grigoriev, S. A.; Mbemba, N.; Brisset, F.; Ranjbari, A.; Etievant, C. *Int. J. Hydrogen Energy* **2010**, *35*, 5043.

(16) Smith, R. D. L.; Prevot, M. S.; Fagan, R. D.; Zhang, Z.; Sedach, P. A.; Siu, M. K. J.; Trudel, S.; Berlinguette, C. P. *Sci.* **2013**, *340*, 60.

(17) May, K. J.; Carlton, C. E.; Stoerzinger, K. A.; Risch, M.; Suntivich, J.; Lee, Y.-L.; Grimaud, A.; Shao-Horn, Y. *J. Phys. Chem. Lett.* **2012**, *3*, 3264.

(18) Surendranath, Y.; Nocera, D. G. In *Progress in Inorganic Chemistry*; John Wiley & Sons, Inc.: 2011, p 505.

(19) Bockris, J. O.; Otagawa, T. *J. Phys. Chem.* **1983**, *87*, 2960.

(20) Su, H.-Y.; Gorlin, Y.; Man, I. C.; Calle-Vallejo, F.; Norskov, J. K.; Jaramillo, T. F.; Rossmeisl, J. *Phys. Chem. Chem. Phys.* **2012**, *14*, 14010.

(21) Shinagawa, T.; Garcia-Esparza, A. T.; Takanabe, K. *Sci, Rep,* **2015**, *5*.

(22) Rossmeisl, J.; Qu, Z. W.; Zhu, H.; Kroes, G. J.; Norskov, J. K. *J, Electroanal, Chem,* **2007**, *607*, 83.

(23) Bockris, J. O.; Otagawa, T. *J. Electrochem. Soc.* **1984**, *131*, 290.

(24) Trasatti, S. *Electrochim. Acta* **1984**, *29*, 1503.

(25) *Earth Materials*; Ernst, W. G., Ed.; Englewood Cliffs, N.J. : Prentice-Hall, 1969.

(26) Hamdani, M.; Singh, R. N.; Chartier, P. *Int. J. Electrochem. Sci.* **2010**, *5*, 556.

(27) Rickard, D.; Butler, I. B.; Oldroyd, A. *Earth. Planet. Sci. Lett.* **2001**, *189*, 85.

(28) Burdett, J. K.; Price, G. D.; Price, S. L. *J. Am. Chem. Soc.* **1982**, *104*, 92.

(29) Briggs, D.; Gibson, V. A. *Chem. Phys. Lett.* **1974**, *25*, 493.

(30) Altavilla, C.; Ciliberto, E. *Appl. Phys. a-Mater. Sci. Process.* **2004**, *79*, 309.

(31) Vialat, P.; Mousty, C.; Taviot-Gueho, C.; Renaudin, G.; Martinez, H.; Dupin, J.-C.; Elkaim, E.; Leroux, F. *Adv. Func. Mater.* **2014**, *24*, 4831.

(32) Choudhury, T.; Saied, S. O.; Sullivan, J. L.; Abbot, A. M. *J. Phys. D* **1989**, *22*, 1185.

(33) Bajdich, M.; Garcia-Mota, M.; Vojvodic, A.; Norskov, J. K.; Bell, A. T. *J. Amer. Chem. Soc.* **2013**, *135*, 13521.

(34) Chivot, J.; Mendoza, L.; Mansour, C.; Pauporte, T.; Cassir, M. *Corrosion Science* **2008**, *50*, 62.

(35) Yeo, B. S.; Bell, A. T. *J. Amer. Chem. Soc.* **2011**, *133*, 5587.

(36) Tung, C.-W.; Hsu, Y.-Y.; Shen, Y.-P.; Zheng, Y.; Chan, T.-S.; Sheu, H.-S.; Cheng, Y.-C.; Chen, H. M. *Nat. Commun.* **2015**, *6*, 8106.

(37) Palmas, S.; Ferrara, F.; Vacca, A.; Mascia, M.; Polcaro, A. M. *Electrochim. Acta* **2007**, *53*, 400.

(38) Boggio, R.; Carugati, A.; Trasatti, S. *J. Appl. Electrochem.* **1987**, *17*, 828.

(39) Nkeng, P.; Poillerat, G.; Koenig, J. F.; Chartier, P.; Lefez, B.; Lopitaux, J.; Lenglet, M. *J. Electrochem. Soc.* **1995**, *142*, 1777.

(40) Li, Y.; Hasin, P.; Wu, Y. *Adv. Mater.* **2010**, *22*, 1926.

(41) Wu, X.; Scott, K. *J. Mater. Chem.* **2011**, *21*, 12344.

(42) Jia, J.; Li, X.; Chen, G. *Electrochim. Acta* **2010**, *55*, 8197.

(43) Godinho, M. I.; Catarino, M. A.; Pereira, M. I. D.; Mendonca, M. H.; Costa, F. M. *Electrochim. Acta* **2002**, *47*, 4307.

(44) Bian, W.; Yang, Z.; Strasser, P.; Yang, R. *J. Power Sources* **2014**, *250*, 196.

(45) Menezes, P. W.; Indra, A.; Sahraie, N. R.; Bergmann, A.; Strasser, P.; Driess, M. *ChemSusChem* **2014**, *8*, 164.

(46) Cui, B.; Lin, H.; Li, J.-B.; Li, X.; Yang, J.; Tao, J. *Adv. Funct. Materials* **2008**, *18*, 1440.

(47) Shi, H.; Zhao, G. *J. Phys. Chem. C* **2014**, *118*, 25939.

(48) Liu, X.; Chang, Z.; Luo, L.; Xu, T.; Lei, X.; Liu, J.; Sun, X. *Chem. Mater.* **2014**, *26*, 1889.

(49) Wen, T. C.; Kang, H. M. *Electrochim. Acta* **1998**, *43*, 1729.

(50) Lee, Y. S.; Hu, C. C.; Wen, T. C. *J. Electrochem. Soc.* **1996**, *143*, 1218.

(51) Rios, E.; Chartier, P.; Gautier, J. L. *Solid State Sci.* **1999**, *1*, 267.

(52) Chen, J. Y. C.; Miller, J. T.; Gerken, J. B.; Stahl, S. S. *Energ. Environm. Sci.* **2014**, *7*, 1382.

(53) Subbaraman, R.; Tripkovic, D.; Chang, K.-C.; Strmcnik, D.; Paulikas, A. P.; Hirunsit, P.; Chan, M.; Greeley, J.; Stamenkovic, V.; Markovic, N. M. *Nat. Mater.* **2012**, *11*, 550.

(54) Zhao, Y.; Han, C.; Yang, J.; Su, J.; Xu, X.; Li, S.; Xu, L.; Fang, R.; Jiang, H.; Zou, X.; Song, B.; Mai, L.; Zhang, Q. *Nano Lett.* **2015**, *15*, 2180.

(55) Marco, J. F.; Gancedo, J. R.; Gracia, M.; Gautier, J. L.; Rios, E.; Berry, F. J. *J. Solid State Chem.* **2000**, *153*, 74.

(56) Parent, A. R.; Crabtree, R. H.; Brudvig, G. W. *Chem. Soc. Rev.* **2013**, *42*, 2247.

(57) Blakemore, J. D.; Schley, N. D.; Olack, G. W.; Incarvito, C. D.; Brudvig, G. W.; Crabtree, R. H. *Chem. Sci.* **2011**, *2*, 94.

(58) Kudo, A.; Miseki, Y. *Chem. Soc. Rev.* **2009**, *38*, 253.

(59) Gray, H. B. *Nat. Chem.* **2009**, *1*, 7.

(60) Cheng, F.; Chen, J. *Chem. Soc. Rev.* **2012**, *41*, 2172.

(61) Herrero, C.; Quaranta, A.; Leibl, W.; Rutherford, A. W.; Aukauloo, A. *Energ. Environm. Sci.* **2011**, *4*, 2353.

(62) Bard, A. J.; Fox, M. A. *Acc. Chem. Res.* **1995**, *28*, 141.

(63) Gorlin, Y.; Jaramillo, T. F. *J. Am. Chem. Soc.* **2010**, *132*, 13612.

(64) Robinson, D. M.; Go, Y. B.; Greenblatt, M.; Dismukes, G. C. *J. Am. Chem. Soc.* **2010**, *132*, 11467.

(65) Gong, M.; Li, Y.; Wang, H.; Liang, Y.; Wu, J. Z.; Zhou, J.; Wang, J.; Regier, T.; Wei, F.; Dai, H. *J. Am. Chem. Soc.* **2013**, *135*, 8452.

(66) Kanan, M. W.; Nocera, D. G. *Sci.* **2008**, *321*, 1072.

(67) Liang, Y.; Li, Y.; Wang, H.; Zhou, J.; Wang, J.; Regier, T.; Dai, H. *Nat. Mater.* **2011**, *10*, 780.

(68) Yang, Y.; Fei, H. L.; Ruan, G. D.; Xiang, C. S.; Tour, J. M. *ACS Nano* **2014**, *8*, 9518.

(69) Singh, R. N.; Pandey, J. P.; Singh, N. K.; Lal, B.; Chartier, P.; Koenig, J. F. *Electrochim. Acta* **2000**, *45*, 1911.

(70) Nikolov, I.; Darkaoui, R.; Zhecheva, E.; Stoyanova, R.; Dimitrov, N.; Vitanov, T. *J. Electroanal. Chem.* **1997**, *429*, 157.

(71) Chen, S.; Qiao, S.-Z. *ACS Nano* **2013**, *7*, 10190.

(72) Chen, S.; Duan, J.; Jaroniec, M.; Qiao, S. Z. *Angew. Chem. Int. Ed.* **2013**, *52*, 13567.

(73) Chen, R.; Wang, H.-Y.; Miao, J.; Yang, H.; Liu, B. *Nano Energy* **2015**, *11*, 333.

(74) Chi, B.; Li, J.; Yang, X.; Lin, H.; Wang, N. *Electrochim. Acta* **2005**, *50*, 2059.

(75) Levine, S.; Smith, A. L. *Disc. Faraday Soc.* **1971**, *52*, 290.

(76) Gupta, V.; Kusahara, T.; Toyama, H.; Gupta, S.; Miura, N. *Electrochem. Commun.* **2007**, *9*, 2315.

(77) Hu, L.; Wu, L.; Liao, M.; Hu, X.; Fang, X. *Adv. Funct. Mater.* **2012**, *22*, 998.

(78) Kobayashi, Y.; Ke, X.; Hata, H.; Schiffer, P.; Mallouk, T. E. *Chem. Mater.* **2008**, *20*, 2374.

(79) Hu, L.; Ma, R.; Ozawa, T. C.; Sasaki, T. *Angew. Chem. Int. Edit.* **2009**, *48*, 3846.

(80) Wang, H.-Y.; Hsu, Y.-Y.; Chen, R.; Chan, T.-S.; Chen, H. M.; Liu, B. *Adv. Energy Mater.* **2015**, *5*, 1500091.

(81) Liu, B. *Nanoscale* **2012**, *4*, 7194.

(82) Kim, H.; Seo, D.-H.; Kim, H.; Park, I.; Hong, J.; Park, K.-Y.; Kang, K. *Chem. Mater.* **2012**, *24*, 720.

(83) Kim, J. G.; Pugmire, D. L.; Battaglia, D.; Langell, M. A. *Appl. Surf. Sci.* **2000**, *165*, 70.

(84) Davidson, A.; Tempere, J. F.; Che, M.; Roulet, H.; Dufour, G. *J. Phys. Chem.* **1996**, *100*, 4919.

(85) Jiménez, V. M.; Fernández, A.; Espinós, J. P.; González-Elipe, A. R. *J. Electron. Spectrosc. Relat. Phenom.* **1995**, *71*, 61.

(86) Shen, Z. X.; Shih, C. K.; Jepsen, O.; Spicer, W. E.; Lindau, I.; Allen, J. W. *Phys. Rev. Lett.* **1990**, *64*, 2442.

(87) Salvati, L.; Makovsky, L. E.; Stencel, J. M.; Brown, F. R.; Hercules, D. M. *J. Phys. Chem.* **1981**, *85*, 3700.

(88) Zhao, G.; Hu, H.; Chen, W.; Jiang, Z.; Zhang, S.; Huang, J.; Lu, Y. *Catal. Sci. Technolog.* **2013**, *3*, 404.

(89) Fang, Y.-H.; Liu, Z.-P. *J. Am. Chem. Soc.* **2010**, *132*, 18214.

(90) Wang, H.-Y.; Hung, S.-F.; Chen, H.-Y.; Chan, T.-S.; Chen, H. M.; Liu, B. *J. Am. Chem. Soc.* **2016**, *138*, 36.

(91) Conell, R. S.; Corrigan, D. A.; Powell, B. R. *Sol. Energy Mater. Sol. Cells* **1992**, *25*, 301.

(92) McBreen, J.; O'Grady, W. E.; Tourillon, G.; Dartyge, E.; Fontaine, A.; Pandya, K. I. *J. Phys. Chem.* **1989**, *93*, 6308.

(93) Lu, P. W. T.; Srinivasan, S. *J. Electrochem. Soc.* **1978**, *125*, 1416.

(94) Chen, S.; Duan, J.; Han, W.; Qiao, S. Z. *Chem. Commun.* **2014**, *50*, 207.

(95) Lee, D. U.; Kim, B. J.; Chen, Z. *J. Mater. Chem. A* **2013**, *1*, 4754.

(96) Jin, C.; Lu, F.; Cao, X.; Yang, Z.; Yang, R. *J. Mater. Chem. A* **2013**, *1*, 12170.

(97) Zhang, Y.; Cui, B.; Zhao, C.; Lin, H.; Li, J. *Phys. Chem. Chem. Phys.* **2013**, *15*, 7363.

(98) Gong, M.; Li, Y.; Wang, H.; Liang, Y.; Wu, J. Z.; Zhou, J.; Wang, J.; Regier, T.; Wei, F.; Dai, H. *J. Am. Chem. Soc.* **2013**, *135*, 8452.

(99) Armand, M.; Tarascon, J. M. *Nat.* **2008**, *451*, 652.

(100) Cook, T. R.; Dogutan, D. K.; Reece, S. Y.; Surendranath, Y.; Teets, T. S.; Nocera, D. G. *Chem. Rev.***2010**, *110*, 6474.

(101) Tueysuez, H.; Hwang, Y. J.; Khan, S. B.; Asiri, A. M.; Yang, P. *Nano Res.* **2013**, *6*, 47.

(102) Jiao, F.; Frei, H. *Angew. Chem. Int. Ed.* **2009**, *48*, 1841.

(103) Xie, X. W.; Li, Y.; Liu, Z. Q.; Haruta, M.; Shen, W. J. *Nat.* **2009**, *458*, 746.

(104) Li, Y.; Shen, W. *Chem. Soc. Rev.* **2014**, *43*, 1543.

(105) Xiao, J.; Kuang, Q.; Yang, S.; Xiao, F.; Wang, S.; Guo, L. *Sci. Rep.* **2013**, *3*.

(106) Hu, L.; Sun, K.; Peng, Q.; Xu, B.; Li, Y. *Nano Res.* **2010**, *3*, 363.

(107) Ma, C. Y.; Mu, Z.; Li, J. J.; Jin, Y. G.; Cheng, J.; Lu, G. Q.; Hao, Z. P.; Qiao, S. Z. *J. Am. Chem. Soc.* **2010**, *132*, 2608.

(108) Surendranath, Y.; Kanan, M. W.; Nocera, D. G. *J. Am. Chem. Soc.* **2010**, *132*, 16501.

(109) Kanan, M. W.; Yano, J.; Surendranath, Y.; Dinca, M.; Yachandra, V. K.; Nocera, D. G. *J. Am. Chem. Soc.* **2010**, *132*, 13692.

(110) Suntivich, J.; May, K. J.; Gasteiger, H. A.; Goodenough, J. B.; Yang, S.-H. *Sci.* **2011**, *334*, 1383.

(111) Mueller, D. N.; Machala, M. L.; Bluhm, H.; Chueh, W. C. *Nature Communications* **2015**, *6*.

(112) Grimaud, A.; May, K. J.; Carlton, C. E.; Lee, Y.-L.; Risch, M.; Hong, W. T.; Zhou, J.; Yang, S.-H. *Nat. Commun.* **2013**, *4*, 2439.

(113) Maitra, U.; Naidu, B. S.; Govindaraj, A.; Rao, C. N. R. *Proc. Natl. Acad. Sci. U. S. A.* **2013**, *110*, 11704.

(114) Maiyalagan, T.; Jarvis, K. A.; Therese, S.; Ferreira, P. J.; Manthiram, A. *Nat. Commun.* **2014**, *5*, 3949

(115) Song, K.; Cho, E.; Kang, Y.-M. *ACS Catal.* **2015**, *5*, 5116.

(116) Kim, T. W.; Woo, M. A.; Regis, M.; Choi, K.-S. *J. Phys. Chem. Lett.* **2014**, *5*, 2370.

(117) Zhang, Y.; Ding, F.; Deng, C.; Zhen, S.; Li, X.; Xue, Y.; Yan, Y.-M.; Sun, K. *Catal. Commun.* **2015**, *67*, 78.

(118) McCrory, C. C. L.; Jung, S. H.; Peters, J. C.; Jaramillo, T. F. *J. Am. Chem. Soc.* **2013**, *135*, 16977.

(119) Biesinger, M. C.; Lau, L. W. M.; Gerson, A. R.; Smart, R. S. C. *Appl. Surf. Sci.* **2010**, *257*, 887.

(120) Liu, I. L.; Shen, P.; Chen, S. Y. *J. Phys. Chem. C* **2010**, *114*, 7751.101)

(121) Belova, I. D.; Roginskaya, Y. E.; Shifrina, R. R.; Gagarin, S. G.; Plekhanov, Y. V.; Venevtsev, Y. N. *Solid State Commun.* **1983**, *47*, 577.

(122) Doyle, R. L.; Lyons, M. E. G. *J. Electrochem. Soc.* **2013**, *160*, H142.

(123) Lyons, M. E. G.; Brandon, M. P. *J. Electroanal. Chem.* **2009**, *631*, 62.

(124) Lian, K. K.; Kirk, D. W.; Thorpe, S. J. *J. Electrochem. Soc.* **1995**, *142*, 4309.

(125) Castro, E. B.; Gervasi, C. A.; Vilche, J. R. *J. Appl. Electrochem.* **1998**, *28*, 835.

(126) Tung, C.-W.; Hsu, Y.-Y.; Shen, Y.-P.; Zheng, Y.; Chan, T.-S.; Sheu, H.-S.; Cheng, Y.-C.; Chen, H. M. *Nat. Commun.* **2015**, *6*, 8106.

(127) Trotochaud, L.; Ranney, J. K.; Williams, K. N.; Boettcher, S. W. *J. Am. Chem. Soc.* **2012**, *134*, 17253.

(128) Marcel, R.; Franziska, R.; Varsha, K.; Petko, C.; Ivelina, Z.; Holger, D. *J. Phys. Conf. Ser.* **2009**, *190*, 012167.

(129) Cobo, S.; Heidkamp, J.; Jacques, P.-A.; Fize, J.; Fourmond, V.; Guetaz, L.; Jousselme, B.; Ivanova, V.; Dau, H.; Palacin, S.; Fontecave, M.; Artero, V. *Nat. Mat.* **2012**, *11*, 802.

(130) Bergmann, A.; Martinez-Moreno, E.; Teschner, D.; Chernev, P.; Gliech, M.; de Araujo, J. F.; Reier, T.; Dau, H.; Strasser, P. *Nat. Commun.* **2015**, *6*, 8625.

(131) Liang, Y.; Wang, H.; Diao, P.; Chang, W.; Hong, G.; Li, Y.; Gong, M.; Xie, L.; Zhou, J.; Wang, J.; Regier, T. Z.; Wei, F.; Dai, H. *J. Am. Chem. Soc.* **2012**, *134*, 15849.

(132) Yang, H. B.; Miao, J.; Hung, S.-F.; Chen, J.; Tao, H. B.; Wang, X.; Zhang, L.; Chen, R.; Gao, J.; Chen, H. M.; Dai, L.; Liu, B. *Sci. Adv.* **2016**, *2*, e1501122.

(133) Chakkaravarthy, C.; Waheed, A. K. A.; Udupa, H. V. K. *J. Power Sources* **1981**, *6*, 203.

(134) Koza, J. A.; He, Z.; Miller, A. S.; Switzer, J. A. *Chem. Mater.* **2012**, *24*, 3567.

(135) Gerken, J. B.; McAlpin, J. G.; Chen, J. Y. C.; Rigsby, M. L.; Casey, W. H.; Britt, R. D.; Stahl, S. S. *J. Am. Chem. Soc.* **2011**, *133*, 14431.

(136) McAlpin, J. G.; Surendranath, Y.; Dinca, M.; Stich, T. A.; Stoian, S. A.; Casey, W. H.; Nocera, D. G.; Britt, R. D. *J. Am. Chem. Soc.* **2010**, *132*, 6882.

(137) Liu, Y.-C.; Koza, J. A.; Switzer, J. A. *Electrochim. Acta* **2014**, *140*, 359.

(138) Goerlin, M.; Chernev, P.; Ferreira de Araújo, J.; Reier, T.; Dresp, S.; Paul, B.; Kraehnert, R.; Dau, H.; Strasser, P. *J. Am. Chem. Soc.* **2016**.

(139) Lindstrom, H.; Sodergren, S.; Solbrand, A.; Rensmo, H.; Hjelm, J.; Hagfeldt, A.; Lindquist, S. E. *J. Phys. Chem. B* **1997**, *101*, 7717.

(140) Brezesinski, T.; Wang, J.; Polleux, J.; Dunn, B.; Tolbert, S. H. *J. Am. Chem. Soc.* **2009**, *131*, 1802.

(141) Smith, R. D. L.; Berlinguette, C. P. *J. Am. Chem. Soc.* **2016**, *138*, 1561.

(142) Burke, M. S.; Kast, M. G.; Trotochaud, L.; Smith, A. M.; Boettcher, S. W. *J. Am. Chem. Soc.* **2015**, *137*, 3638.

(143) Hadjiev, V. G.; Iliev, M. N.; Vergilov, I. V. *J. Phys. C* **1988**, *21*, L199.

(144) Koza, J. A.; Hull, C. M.; Liu, Y.-C.; Switzer, J. A. *Chem. Mater.* **2013**, *25*, 1922.

(145) Shamir, J.; Binenboym, J.; Claassen, H. H. *J. Am. Chem. Soc.* **1968**, *90*, 6223.

(146) Zhang, M.; de Respinis, M.; Frei, H. *Nat. Chem.* **2014**, *6*, 362.

(147) Merrill, M.; Worsley, M.; Wittstock, A.; Biener, J.; Stadermann, M. *J. Electroanal. Chem.* **2014**, *717–718*, 177.

(148) Louie, M. W.; Bell, A. T. *J. Am. Chem. Soc.* **2013**, *135*, 12329.

(149) Diaz-Morales, O.; Ferrus-Suspedra, D.; Koper, M. T. M. *Chem. Sci.* **2016**, *7*, 2639.

(150) Long, R. Q.; Huang, Y. P.; Wan, H. L. *J. Raman Spectroscop.* **1997**, *28*, 29.

(151) Itoh, T.; Maeda, T.; Kasuya, A. *Faraday Discuss.***2006**, *132*, 95.

(152) Lunsford, J. H.; Yang, X.; Haller, K.; Laane, J.; Mestl, G.; Knoezinger, H. *The Journal of Physical Chemistry* **1993**, *97*, 13810.

(153) Giamello, E.; Sojka, Z.; Che, M.; Zecchina, A. *J. Phys. Chem.* **1986**, *90*, 6084.

(154) Zecchina, A.; Spoto, G.; Coluccia, S. *Journal of Molecular Catalysis* **1982**, *14*, 351.

(155) Ullman, A. M.; Brodsky, C. N.; Li, N.; Zheng, S.-L.; Nocera, D. G. *J. Am. Chem. Soc.* **2016**, *138*, 4229.

(156) Jongsomjit, B.; Panpranot, J.; Goodwin, J. G. *J. Catal.* **2001**, *204*, 98.

(157) Hadzic, B.; Romcevic, N.; Romcevic, M.; Kuryliszyn-Kudelska, I.; Dobrowolski, W.; Trajic, J.; Timotijevic, D.; Narkiewicz, U.; Sibera, D. *J. Alloys Compd.* **2012**, *540*, 49.

(158) Binninger, T.; Mohamed, R.; Waltar, K.; Fabbri, E.; Levecque, P.; Kotz, R.; Schmidt, T. J. *Sci. Rep.* **2015**, *5*, 12167.

(159) Mavrikakis, M.; Hammer, B.; Nørskov, J. K. *Phys. Rev. Lett.* **1998**, *81*, 2819.

(160) Görlin, M.; Chernev, P.; Ferreira de Araújo, J.; Reier, T.; Dresp, S.; Paul, B.; Krähnert, R.; Dau, H.; Strasser, P. *J. Am. Chem. Soc.* **2016**, *138*, 5603.

Publication List

§Paper

1. **Hsin-Yi Wang,** Sung-Fu Hung, Ying-Ya Hsu, Lulu Zhang, Jianwei Miao, Ting-Shan Chan, Qihua Xiong, and Bin Liu, In-Situ Spectroscopic Identification of μ-OO Bridging on Spinel Co3O4 Water Oxidation Electrocatalyst*, J. Phys. Chem. Lett.*, **2016**, *7*, 4847.
2. **Hsin-Yi Wang,** Han-Yi Chen, Ying-Ya Hsu, Ulrich Stimming, Hao Ming Chen, and Bin Liu,* Modulation of Crystal Surface and Lattice by Doping: Achieving Ultrafast Metal-Ion Insertion in Anatase TiO_2, *ACS Appl. Mater. Interfaces*, **2016**, *8*, 29186.
3. **Hsin-Yi Wang,** Hongbin Yang, Liping Zhang, Jiazang Chen, and Bin Lin,* Niobium Doping Enhances Charge Transport in TiO_2 Nanorods, *ChemNanoMat.,* **2016**, *2*, 660.
4. **Hsin-Yi Wang,** Sung-Fu Hung, Han-Yi Chen, Ting-Shan Chan, Hao Ming Chen, and Bin Lin,* In-Operando Identification of Geometrical-Site-Dependent Water Oxidation Activity of Spinel Co_3O_4. *J. Am. Chem. Soc.*, **2016**, *138*, 36.
5. **Hsin-Yi Wang,** Jianwei Zheng, Fang-Xing Xiao and Bin Lin* Doping-induced structural evolution from rutile to anatase: formation of Nb-doped anatase TiO_2 nanosheets with high photocatalytic activity, *J. Mater,.Chem. A*, **2016**, *4*, 6926.
6. **Hsin-Yi Wang,** Ying-Ya Hsu, Rong Chen, Ting-Shan Chan, Hao Ming Chen* and Bin Liu,* Surface Ni^{3+} Induced Formation of Active NiOOH on Spinel Ni-Co Oxide for Efficient Oxygen Evolution Reaction, *Adv. Energy Mater.*, **2015**, *5,* 1500091.
7. **Hsin-Yi Wang,** Jiazang Chen, Sunny Hy, Linghui Yu, Zhichuan Xu and Bin Liu,* High-surface-area mesoporous TiO_2 microspheres via one-step nanoparticle self-assembly for enhanced lithium-ion storage, *Nanoscale,* **2014**, *6,* 14926.
8. **Hsin-Yi Wang,** Fang-Xing Xiao, Le Y , Bin Liu,* and Xiong Wen (David) Lou,* Hierarchical α-MnO_2 Nanowires@$Ni_{1-x}Mn_xO_y$ Nanoflakes Core-Shell Nanostructures for Enhanced Energy Storage, *small,* **2014**, *10,* 3181.

9. **Hsin-Yi Wang** and Fu-Ming Wang,* Electrochemical investigation of an artificial solid electrolyte interface for improving the cycle-ability of lithium ion batteries using an atomic layer deposition on a graphite electrode, *J. Power sources,* **2013**, *233,* 1.
10. **Hsin-Yi Wang**, Fu-Ming Wang,* Yung-Yun Wang and Chi-Chao Wan, Electrochemical Formation of Pt Nanoparticles on Multiwalled Carbon Nanotubes: Useful for Fabricating Electrodes for Use in Dye-Sensitized Solar Cells*, J. Phys. Chem. C*, **2011***, 115,* 8439.
11. Rong Chen, **Hsin-Yi Wang**, Jianwei Miao, Hongbin Yang, Bin Liu,* A Flexible High-Performance Oxygen Evolution Electrode with Three-Dimensional $NiCo_2O_4$ Core-Shell Nanowires, *Nano Energy,* **2015**, *11,* 333.
12. Qian Zhang, **Hsin-Yi Wang**, Xinli Jia, Bin Liu* and Yanhui Yang*, One-dimensional metal oxide nanostructures for heterogeneous catalysis, *Nanoscale,* **2013**, *5,* 7175.
13. Fu-Ming Wang, **Hsin-Yi Wang**, Meng-Han Yu, Yi-Ju Hsiao and Ying Tsai, Differential pulse effects of solid electrolyte interface formation for improving performance on high-power lithium ion battery, *J. Power sources,* **2011**, *196,* 10395.
14. Fang-Xing Xiao, Jianwei Miao, **Hsin-Yi Wang**, Hongbin Yang, Jiazang Chen and Bin Liu,* Electrochemical construction of hierarchically ordered CdSe-sensitized TiO_2 nanotube arrays: towards versatile photoelectrochemical water splitting and photoredox applications, *Nanoscale,* **2014**, *6,* 6727.
15. Fang-Xing Xiao, Jianwei Miao, **Hsin-Yi Wang**, and Bin Liu,* Self-assembly of hierarchically ordered CdS quantum dots-TiO_2 nanotube array heterostructures as efficient visible light photocatalysts for photoredox applications, *J. Mater. Chem. A,* **2013**, *39,* 12229.
16. Fang-Xing Xiao, Sung-Fu Hung, Jianwei Miao, **Hsin-Yi Wang**, Hongbin Yang, Bin Liu,* TiO2 Nanotubes: Metal-Cluster-Decorated TiO2 Nanotube Arrays: A Composite Heterostructure toward Versatile Photocatalytic and Photoelectrochemical Applications, *Small*, **2015**, 11, 553.
17. Jiazang Chen, Hong Bin Yang, Jianwei Miao, **Hsin-Yi Wang**, and Bin Liu,*

Thermodynamically Driven One-Dimensional Evolution of Anatase TiO_2 Nanorods: One-Step Hydrothermal Synthesis for Emerging Intrinsic Superiority of Dimensionality, *J. Am. Chem. Soc.*, **2014,** *136,* 15310.

18. Bin Liu, Li-Min Liu, Xiu-Feng Lang, **Hsin-Yi Wang**, Xiong Wen (David) Lou, and Eray S. Aydil,* Doping high-surface-area mesoporous TiO_2 microspheres with carbonate for visible light hydrogen production, *Energy Environ. Sci.,* **2014,** *7,* 2592.

19. Fang-Xing Xiao, Jianwei Miao, Hua Bing Tao, Sung-Fu Hung, **Hsin-Yi Wang**, Hong Bin Yang, Jiazang Chen, Rong Chen, Bin Liu,* One-Dimensional Hybrid Nanostructures for Heterogeneous Photocatalysis and Photoelectrocatalysis, *Small*, **2015***, 11*, 15.

20. Jiazang Chen, Hong Bin Yang, Hua Bing Tao, Liping Zhang, Jianwei Miao, **Hsin-Yi Wang**, Junze Chen, Hua Zhang, Bin Liu,* Surface Rutilization of Anatase TiO_2 Nanorods for Creation of Synergistically Bridging and Fencing Electron Highways, *Adv. Funct. Mater.*, **2016**, *26*, 456.

§Patents

1. "CHARGING PROTOCOL" Patent, **Hsin-Yi Wang**, Bing-Joe Hwang, applying in Taiwan and US, Corrected Proof.

※" CHARGING PROTOCOL" could automatically modify its amplitude of charging current based on the voltage polarization during charging and applied the newly adjusted charging current to the following cycles.

2. ANODE PROTECTOR OF LITHIUM-ION BATTERY AND METHOD FOR FABRICATING THE SAME, Fu-Ming Wang*、**Hsin-Yi Wang**、Chin-Shu Cheng，R. O. C. Apply No. 101100658；P. R. C Patent No. 201210003022.4；U. S. A. Patent No. 8808901B2；Japan Apply No. 2012-113191

※" ANODE PROTECTOR" is an artificial passivation layer used to protect the electrode surface in Li-ion battery.

§Posters

1. **Hsin-Yi Wang**, Jianwei Zheng, Sung-Fu Hung, Han-Yi Chen, Ting-Shan Chan, Hao Ming Chen, and Bin Lin "*In-Operando Identification of Geometrical-Site-Dependent Water Oxidation Activity of Spinel* Co_3O_4." , The 251th ACS National Meeting, USA, San Diego, **2016**
2. **Hsin-Yi Wang**, Fu-Ming Wang, Yueh-Wen Chen "*Feedback controlled multistage constant current (FCMCC) charging protocol for improving performance on Li-ion battery*" , The 16th International Meeting on Lithium Batteries, Korea, **2012**
3. **Hsin-Yi Wang**, Fu-Ming Wang, Lyu-Ye Yang "*Differential pulse formation of solid electrolyte interface (SEI) for enhancing performance on Li-ion battery at high temperature operation*" , The 16th International Meeting on Lithium Batteries, Korea, **2012**
4. **Hsin-Yi Wang**, Fu-Ming Wang, Bing-Joe Hwang "*Multistage constant current for fast-charging Li-ion battery with enhanced long cycle life*" , 62nd Annual Meeting of the International Society of Electrochemistry in Niigata, Japan, **2011**